Placental Insufficiency in the Rhesus Macaque

By

Logan T. Keding

A dissertation submitted in partial fulfillment of
the requirements for the degree of

Doctor of Philosophy
(Endocrinology and Reproductive Physiology)

at the
UNIVERSITY OF WISCONSIN-MADISON
2025

Date of final oral examination: 15 August 2025

The dissertation is approved by the following members of the Final Oral Committee:
Aleksandar K. Stanic, Associate Professor, Obstetrics and Gynecology
Oliver Wieben, Professor, Medical Physics and Radiology
Jenny Gumperz, Professor, Medical Microbiology and Immunology
Sathish Kumar, Professor, Comparative Biosciences

To Sarah, Aldo,
and I guess Rey.

ACKNOWLEDGEMENTS

Many individuals have provided me crucial guidance and support *en route* to the completion of this dissertation and degree. Countless who have helped along the way do not receive mention here in interest of brevity. I thank you all from the bottom of my heart for your contributions to my life and education.

First, I want to thank my parents, Kelly and Kurt Keding, for gifting me with unconditional and unwavering support that has provided the foundation of my whole academic journey. The practical and philosophical lessons they have passed down to me have undoubtedly contributed to the success of work outlined here. Specifically, I would like to thank my mother for her studious nature and open-mindedness, and my father for his work ethic and charismatic nature – to the extent that I have been able to implement these qualities in my own life, I have become a better man and scientist.

I would next like to thank the rest of my immediate and extended family. My grandmother Rita, for her incredible mental fortitude and benevolent nature, and my grandfather Jerry, for his resolute ethics, love of nature, and resourcefulness. My extended family, Kaylin, Reegan, Jenna, Ali, Jack, Kerri, and Kim for their love and support, which has remained a constant throughout my entire life. And last, my sister and brother, Grady and Taylor. Thank you, Grady, for emanating positivity and assurance throughout my life and academic journey. And thank you Taylor, for enthusiastically accepting your role as my mentor and friend since the beginning.

I would like to thank all the academic mentors that have helped me along this journey. Kerrie Hoar, for igniting my love for human anatomy and guiding me early on in my career. Barrett Klein, who taught me that there is room to creativity, artistry, and eccentricity in academia, and that it is crucial we make space for it. Ted Golos, for doing the dirty work of molding my scientific understanding and approach, while allowing me the freedom to pursue novel experimental approaches. Jenna Schmidt, for her effective hands-on mentorship and the myriad of opportunities she has given me throughout the years – all the while conducting herself with stoicism and grace. Jessica Vazquez, for her perfect pairing of personable and professional in the scientific realm – your love of science and passion helps illuminate all those who work with you. And finally, my PhD mentor Aleks Stanic, thank you for your relentless optimism, positive energy, and innovative approaches to science. I'm confident your endless well of scientific knowledge and energy will never run dry.

Last, I would like to thank my wife, Sarah. I would not have made it through this journey without her love and support. Her endless curiosity, incredible work ethic, and *joie de vivre* have made the last four years of this work not only possible, but enjoyable. I could not have dreamed of having a better partner to build a home, family, and career with. Thank you so much for everything, I love you.

In addition, I would like to acknowledge all the individuals that contributed directly to the experiments outlined in this dissertation.

The work outlined in Chapter 2 was conceptualized by Dr. Jenna Schmidt. The eight-day differentiation experiments were completed in collaboration with Avery Heselton. The processing of samples for RNA expression was completed in collaboration with Emily Ren, Avery Heselton, and Dr. Jenna Schmidt. The processing and analysis of samples by flow cytometry was completed by Dr. Michelle Koenig. Immunohistochemical staining of macaque placental samples was completed by Sarah Shaw. All authors helped in the process of reviewing and editing the final manuscript.

The work outlined in Chapters 3 and 4 was conceptualized by Logan Keding. Both Dr. Heather Simmons and Dr. Crystal Bockoven were consulted periodically throughout development of placental pathological feature analysis outlined in Chapter 3, providing crucial feedback concerning pathological feature and sub-tissue categorization. Primary placental cotyledon tissues and ferumoxytol-contrast MRI data in three of the seven animals used in Chapter 4 were collected by Dr. Sydney Nguyen and Dr. Daniel Seiter. Data from the remaining four animals were collected in collaboration with Dr. Jessica Vazquez, Dr. Ruiming Chen, and Ruo-Yu Liu. Processing of dynamic contrast enhanced MRI data was accomplished through the work of Ruo-Yu Liu.

The work outlined in Chapter 5 was conceptualized by Dr. Thaddeus Golos, Dr. Oliver Wieben, and Dr. Dinesh Shah. Placental injections were performed by Dr. Kathleen Antony and Dr. Jenna Racine. Placental cotyledon staining and digitization was performed in collaboration with Emily Bove and Jessica Dorobek. Whole placental histopathological analysis was completed by Dr. Heather Simmons. Processing of dynamic contrast enhanced MRI data was accomplished through the work of Ruo-Yu Liu. Placental dissection, flow cytometry, and cytokine analyses were completed in collaboration with Dr. Jessica Vazquez. All authors helped in the process of reviewing and editing the final manuscript.

The work outlined in Chapter 6 was conceptualized by Logan Keding. Experimental planning, preparation, and analysis was accomplished with the help of Dr. Taylor Keding, Dr. Aleksandar Stanic and Dr. Jessica Vazquez.

I would like to sincerely thank all the co-authors and collaborators that have made this work possible. In addition, I would like to thank those at the Wisconsin National Primate Research Center, particularly those in the SPI group, the Animal Care Staff, Pathology Services, and Assay Services. I am eternally grateful for the effort you have all made to make this collective work possible.

TABLE OF CONTENTS

ABSTRACT

Adverse pregnancy outcomes (APOs) occur in 1 in 5 births and are broadly attributed to placental insufficiency, a condition where a fetus *in utero* receives insufficient oxygen and/or nutrients to sustain healthy development. Although limited *in vivo* techniques are available, placental insufficiency is most often observed clinically by placental pathology *ex vivo*. Furthermore, although much has been done to categorize these pathologies, little is known regarding the mechanism(s) by which placental insufficiency occurs. The rhesus macaque pregnancy model closely resembles the anatomy, physiology, and duration of human pregnancy. We leveraged both *in vitro* and *in vivo* techniques to model placental function and insufficiency in the primate, using the rhesus macaque.

There is evidence that extravillous trophoblast (EVT) differentiation occurs in relative hypoxia *in vivo*. We cultured macaque EVTs in a low oxygen environment *in vitro*, to see if this would reduce morphological heterogeneity. Low oxygen resulted in immature extravillous trophoblast (EVT) populations (potentially modeling less invasive EVTs observed in APOs). Additionally, we confirmed the identity of *in vitro* EVTs through marker expression and further revealed an EVT-specific macaque surface marker, NCAM1. Together, these data establish macaque EVTs as an *in vitro* model and may present an opportunity for future APO modeling *in vitro*.

Next, we established novel methodology to quantify placental pathological features of the macaque *in vivo*. We leveraged this technique in healthy/normal pregnant macaques to investigate relationships between pathology, pregnancy

biometrics, and maternal blood flow. We found that increased pathology was associated with decreased maternal blood flow at the cotyledon level, that mineralization was associated with both decreased fetal weight and decreased maternal blood flow, and that secondary discs in the macaque demonstrated unique relationships to placental perfusion and pathology, suggesting a compensatory mechanism associated with increased mineralization. Together, these data demonstrate multiple pathology-perfusion relationships at the cotyledon level for the first time, and that quantities of placental pathology considered sub-threshold in humans' effect fetal size in healthy/normal macaque pregnancy.

Our final experiments aimed to model placental insufficiency in the rhesus *in vivo*, as a platform in which to trial human APO therapeutics. We first used an intraplacental injection of MCP-1, intending to induce placental inflammation. What we observed was a decrease in placental mineralization, and healthy/normal maternal blood flow and fetal metrics, suggesting that MCP-1 alone may serve a beneficial role in pregnancy. Additionally, we utilized an ischemia/reperfusion injury (IRI) at the placenta to induce oxidative stress and injury. The preliminary time-series experiment produced strong evidence that a 2-hour ligation results in the placental injury indicative of an acute IRI. Future aims include annotating human placentae to assess pathological features and to determine if a single IRI results in the placental insufficiency and APOs at full term, as is observed in human pregnancy. Together, these *in vitro* and *in vivo* studies have succeeded in bettering our understanding of placental physiology and insufficiency in primate pregnancy.

CHAPTER 1

AN INTRODUCTION TO THE PLACENTA

An estimated 350,000 human births occur each day, worldwide [1]. Integral to each of these pregnancies is the placenta, constituting the primary maternal-fetal interface of gestation. The placenta is a miraculous tissue – a singular lifeline facilitating the transfer of all oxygen, nutrients, and waste between mother and fetus. Unfortunately, the placenta has also been aptly termed "the forgotten organ", as it has long been underappreciated, both culturally and scientifically [1]. A major shift in our conceptualization of how the placenta and *in utero* environment affects human health occurred in the 1980's, with the development of "the fetal origins hypothesis" [2]. Also known as "the Barker hypothesis", this framework details how altered aspects of gestation can lead to diminished fetal health acutely, as well as later in life [2]. Specifically, they proposed that diminished nutrition led to permanent alterations in an individual's physiology and increased their risk of lifelong illness [3]. Since the idea's conception, the significant impact of placental development and function on fetal health has become an axiom in human biology, paving the way for increased investigation of the *in utero* environment and placenta. Unfortunately, a considerable lack in understanding of placental disease still exists, as evidenced by the 1 in 5 births effected by adverse pregnancy outcomes [4]. This dissertation presents studies aimed at bettering our collective understanding of placental disease through placental pathological analysis, as well as *in vitro* and *in vivo* placental modeling in the rhesus macaque monkey.

Macro and micro placental anatomy

The human placenta is an organ of discoid structure, comprised of both maternal and fetal tissue [1] (Figure 1.1A). The disc is formed of 15-20 cotyledons, partially separated by placental septa [5] (Figure 1.1B). These cotyledons represent the functional units of the placenta, partially sharing blood flow across a semi-continuous intervillous space [6,7]. The fetal component of the placenta consists of a chorionic plate and chorionic/placental villi. Villi sprouting from the chorionic plate (stem villi) grow in a tree-like structure, branching into secondary and tertiary villous extensions – ever expanding their surface area for maximal oxygen and nutrient exchange with maternal blood. The most distal region of villous tissue is the placental cell column, which makes direct contact with the decidua basalis, the maternal portion of the placenta. Decidual tissue is formed from maternal endometrium in a process called decidualization [8], and infiltrated by fetal cells in the first trimester to help establish placental blood flow [9]. This decidua/cell column boundary constitutes the maternal/fetal interface of the placenta - facilitating maternal blood flow into the intervillous space and bathing the placental villi with oxygen/nutrient rich blood, sustaining fetal development throughout pregnancy[10].

Trophoblasts are fetal cells outside of the blastocyst (primitive embryo) that give rise to the major functional cell types of the placenta. The progenitor trophoblast cell population of the placenta are the cytotrophoblasts (CTBs) (Figure 1.1C). These CTBs give rise to two major differentiated placental cell types: extravillous trophoblasts (EVTs) and the syncytiotrophoblast (STB). EVTs migrate from the

placental cell columns into the decidua, invading maternal spiral arteries and remodeling vascular architecture (Figure 1.1C). This remodeling allows for low resistance, high capacity maternal blood flow to enter placental intervillous space [9]. The STB forms a continuous outer layer along the exterior of the placental villi and is in direct contact with maternal blood [10] (Figure 1.1C). The STB is primarily responsible for transport of oxygen and nutrients into fetal circulation, in addition to providing a first line of defense against pathogens in the maternal blood [10].

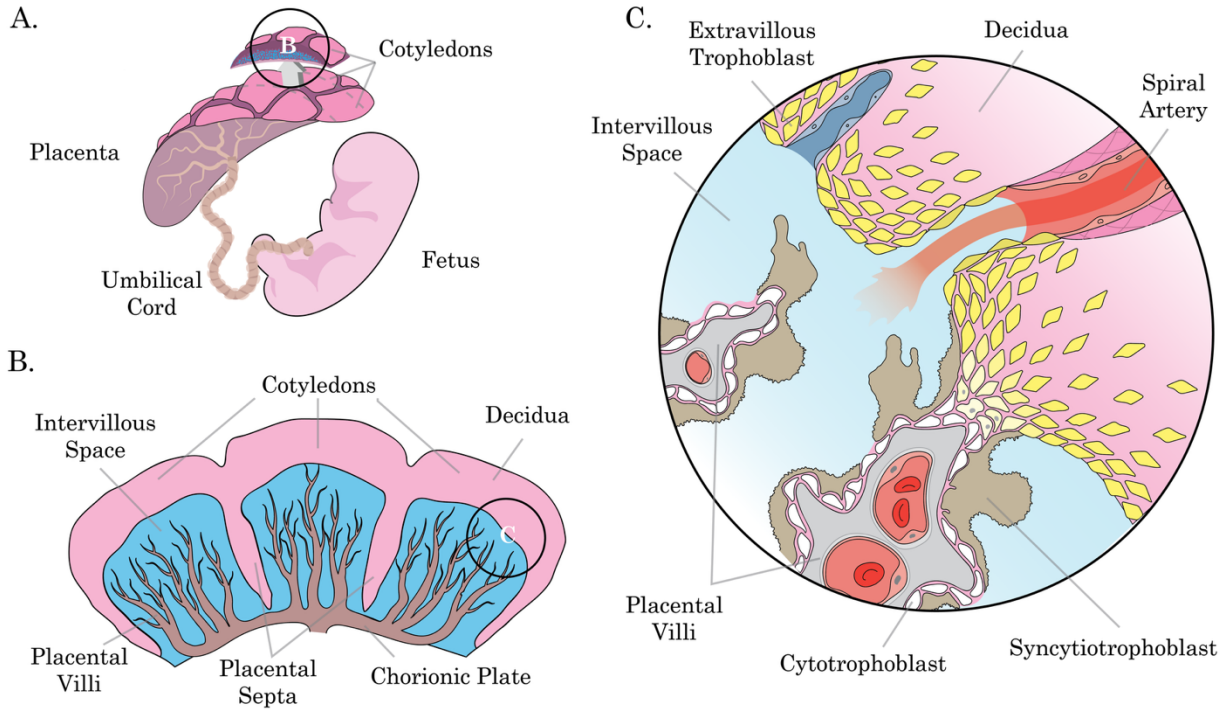

Figure 1.1. A graphical overview of macro and micro placental anatomy. A) A macro view of fetus, umbilical cord, and placenta, with an elevated placental center cut. B) Increased resolution of a placental center cut, displaying three cotyledons separated by placental septa. Each cotyledon contains chorionic plate, placental villi, and decidual tissues C) Micro view of placental anatomy, showing the three major trophoblast populations. Cytotrophoblasts (CTBs) and syncytiotrophoblast (STB) line the placental villi, while extravillous trophoblasts (EVTs) invade decidual tissue, remodeling maternal spiral arteries. The area of CTB transition into invasive EVTs represents the cell column.

Pathological evidence of placental insufficiency

Maternal vasculature remodeling and villous development within the placenta requires a substantial exchange of physiological and immunological cues between mother and fetus to ensure the proper coordination of developmental events. Placental insufficiency occurs when abnormal maternal blood supply to the placenta [11], and/or decreased nutrient/oxygen transport [12,13] results in altered placental exchange, potentially diminishing fetal development. Currently, clinicians rely on ultrasound evaluations of fetal heart rate or umbilical artery Doppler to determine acute changes in blood flow and overall health of the fetus *in vivo* [14]. However, most evidence of placental insufficiency is acquired through detailed pathological analysis of placental lesions following parturition *ex vivo* [15].

Several pathological meta-categories have been developed to encapsulate all possible lesions of the placenta [15]. Pathologies of maternal vascular malperfusion (MVMs) denote injuries that arise because of altered maternal blood circulation at the placenta and are largely confined to the maternal compartment (the decidua and intervillous space). Pathologies confined to the fetal compartment are termed fetal vascular malperfusion (FVM) pathologies and result in altered placental exchange to and from the fetus. Additionally, chronic inflammatory pathologies of the placenta occur across both maternal and fetal compartments, resulting in the collapse of intervillous space, structural damage to the villi, and decreased functional syncytial surface area [16]. Altered villous growth, local ischemia, and damage to villous vasculature associated with all of these conditions hinder the capacity for nutrient

and oxygen transport to the fetus [11,17,18]. Combined, these conditions contribute to placental pathology and are associated with placental insufficiency in pregnancy.

Maternal vascular malperfusion (MVM)

In certain contexts, the MVM designation has completely replaced the term "placental insufficiency", as it encapsulates all lesions associated with pathological maternal blood flow [13], the only route by which oxygen and nutrients are transported to the fetus. MVM pathologies contribute to a diminished perfusable surface area for maternal blood, often resulting in villous ischemic necrosis [17]. Common pathologies of MVM include placental infarction, massive perivillous fibrin deposition, intervillous thrombosis, and retroplacental hematomas [17]. In general, these pathologies occur at the basal plate and constitute a majority of the pathologies observed in the placenta [13,17].

Fetal vascular malperfusion (FVM)

Manifestations of FVM and MVM are inextricably linked within the placental compartment during pregnancy. As a matter of definition, FVM pathologies solely encompass mechanisms of restricted blood flow within the fetal compartment [15]. These can have etiologies based on fetal, umbilical, placental, or uterine origins, and are most often due to some form of obstructed blood flow [17]. Vessel thrombosis, intravillous hemorrhage, delayed villous maturation, avascular/sclerotic villi, and villous stromal mineralization are all common pathologies of FVM, and are further associated with poor fetal outcomes when designated as high-grade [17,19].

Chronic inflammation pathologies

Placental inflammation that is known to contribute to insufficiency predominantly involves chronic inflammatory pathologies affecting the villous region - including chronic villitis, chronic histiocytic intervillositis (CHIV), and villitis of unknown etiology (VUE) [17]. In chronic villitis and VUE, CD3+ and CD8+ maternal T cell and CD68+ macrophage infiltration is observed within villi, as well as architectural breakdown, necrosis, and mineralization [17,20]. Additionally, there are inflammatory lesions that specifically affect the chorionic plate (chronic chorioamnionitis) and decidua (chronic deciduitis) [17]. Many of these pathologies demonstrate a high degree of co-expression, even across placental sub-tissues, suggesting a common etiology [17]. Although placental inflammation can be traced to infection in a minority of cases, a growing body of evidence suggests that the maternal immune system is demonstrating an adverse reaction to fetal tissue (allograft rejection) in a majority of cases [21].

Placental insufficiency and adverse pregnancy outcomes

A majority of adverse pregnancy outcomes (APOs) are associated with placental pathologies of insufficiency [11,22], while factors such as chromosomal [23] and genetic [24] abnormalities seem to contribute to a minority of cases [23]. Major APOs include fetal growth restriction, preeclampsia, and preterm birth [25], affecting approximately 1 in 5 births in the United States [4]. These conditions are associated with lifelong impacts for the offspring and potentially the mother, by increasing the risk of cardiovascular disease, type 2 diabetes, and stroke [4,26]. Additionally, these

APOs often demonstrate symptom manifestation late in gestation [27,28], allowing for potential early therapeutic or clinical intervention to help improve pregnancy outcomes.

Modeling placental function and insufficiency *in vitro* and *in vivo*

The high incidence of APOs currently observed worldwide [4] in combination with ever-declining fertility rates [29] underscores the need for better mechanistic understanding of placental physiology to promote pregnancy success. A myriad of placental/pregnancy models are currently available for researchers to gain insight into mechanisms of placental function and insufficiency - each presenting unique functional, financial, and ethical considerations. *In vitro* techniques primarily consist of using placental explants, placental primary cells, or placental stem cells (in 2D or 3D culture) to observe, model, and manipulate placental physiology. These models allow for increased control of exposure conditions [30], real-time analysis [31], and experimental manipulation [32] that *in vivo* models largely lack [33]. However, *in vitro* modeling is hindered by the uncertainty of biological translatability, as cells and tissues may function and respond differently *ex vivo* than they otherwise would *in vivo*. For this reason, *in vivo* models of pregnancy show translational utility, as they offer a more complete reproduction of physiological dynamics, and therefore, increased clinical relevance. Within the various non-human animal models available for *in vivo* study, there are varying degrees to which the model captures placental likeness to humans. Major factors include the animal's genetic relatedness to humans, length of pregnancy, placental macro and micro anatomy, and how the

maternal blood interacts with the fetal tissue at the placenta for oxygen and nutrient exchange. Of the mainstream models currently in use, the non-human primate represents the most biologically akin model of human pregnancy available.

The rhesus macaque as a model of primate pregnancy

The macaque shares close phylogenetic proximity and placental similarity to humans [10,34]. Importantly, the macaque placenta shares a hemochorial (maternal blood in direct contact with placental villi) and villous branching structure with human placentae [10]. This, in addition to a similarly-long gestational period [35] makes the macaque an ideal model of human pregnancy [36,37]. Importantly, macaque models of pregnancy uniquely enable *in vitro* and *in vivo* study crossover throughout each stage of gestation, from conception to delivery. This enables leveraging the best aspects of both model systems in-tandem, resulting in more biologically valid and generalizable results and greater promise of clinical translation. Although there is limited evidence that rhesus macaques develop APOs naturally [38], they naturally express the same pathologies of placental insufficiency as the human [39,40] and have demonstrated APOs manifestation through induced placental insufficiency [41]. As the study of human pregnancy *in vivo* and *in vitro* is justifiably limited [42], these qualities make the macaque is an invaluable tool for modeling of placental insufficiency and APOs. Considering this, all placental investigation described in this dissertation utilized the rhesus macaque pregnancy model.

Dissertation overview

This dissertation is a distillation of four years of study, centered around bettering our collective understanding of placental anatomy, physiology, and pathology. My central aim was to produce functional models of APO and placental insufficiency using the rhesus macaque. A primate model of placental insufficiency would allow for greater insight into how altered maternal blood flow affects placental pathology manifestation, as well as provide an *in vivo* platform to test and evaluate therapeutics improve human pregnancy outcomes. In addition, developing a robust *in vitro* model of macaque trophoblasts alongside an *in vivo* APO model would allow for experimental crossover, and assessment of APO therapeutics effects on trophoblasts with increased resolution, prior to their study *in vivo*. With this in mind, we began our studies by focusing on our *in vitro* techniques to model trophoblasts of the macaque placenta.

In vitro extravillous trophoblast differentiation in low oxygen

In our previous *in vitro* macaque trophoblast cell culture work, we observed morphological heterogeneity in our macaque extravillous trophoblasts (EVTs) [43]. Work by others suggests that EVTs *in vivo* differentiate in relative hypoxia [44], and that EVT differentiation *in vitro* improves when accomplished with low oxygen incubation [45]. Accordingly, we investigated whether macaque EVT differentiation in low oxygen would improve EVT categorization by decreased morphological heterogeneity and increased classically defined EVT marker expression. We found that in both ambient and low oxygen incubation, our macaque EVTs express similar

genes to humans EVTs at crucial points in the differentiation process. Furthermore, we found that NCAM1 serves as a macaque EVT-specific surface marker, for better identification of EVTs in future *in vitro* and *in vivo* study. Last, we observed that differentiating EVTs in low oxygen resulted in a less mature cell type of diminished proliferative capacity. This population may be representative of the less invasive endovascular EVTs observed in placental insufficiency APOs such as preeclampsia [11,46,47], however more categorization work will need to be done to better assess this possibility. Importantly, this *in vitro* macaque EVT model can serve as a platform by which to investigate questions of EVT-induced placental insufficiency in the primate – as well as serve as a preliminary tool to study the effects of therapeutics prior to *in vivo* experimentation.

Investigating placental pathology, perfusion, and biometrics in healthy macaques

Next, we turned to *in vivo* investigations of rhesus macaque pregnancy. As placental insufficiency is primarily determined through pathological analysis *ex vivo* [18], we first developed a novel form of placental pathology analysis to aid in our investigation of these pathologies of placental insufficiency. To this end, we classified common histopathological features through digital annotation – with the goal of making a more quantitative, objective, and transparent form of placental analysis. Using digital annotation and pixel quantification, we were able to report precise areas of pathology, as opposed to classically utilized estimation methods [15]. Further, it is our position that this is a more objective form of analysis – as no assumptions are made about the origins of the histopathological features of which we quantify. And

finally, we suggest this analysis increases investigative transparency – as all quantification is a matter of record – stored in electronic files for review and potential revision.

We utilized this methodology, alongside dynamic contrast-enhanced magnetic resonance imaging (MRI) methods previously developed by our group [39,48]; to investigate relationships between placental pathology and fetal/maternal/placental biometrics, as well as maternal blood perfusion, at the cotyledon level. We performed these analyses on tissues from healthy/normal macaque pregnancies, to establish an idea of what baseline relationships exist between these variables in primate pregnancy. Through this effort, we demonstrated that increased pathology resulted in decreased maternal blood flow at the cotyledon. We also found that stromal mineralization (a historically overlooked pathology [19]) demonstrated significant relationships to maternal blood flow and fetal weight – a correlation only demonstrated in severe cases when assessing human pregnancy [19]. Additionally, we provide evidence for a common etiology behind underlying pathological lesions of villous intervillous fibrin deposition and agglutination, such as placental infarction and chronic villitis. Finally, we highlight the compensatory potential of the secondary disc in healthy pregnancy and propose a distinct compensatory-driven etiology for placental mineralization. Put together, this work helps to classify baseline pathologies present in healthy/normal macaque placentae, as well as tease apart relationships between placental pathologies, maternal blood perfusion, and fetal outcome at the cotyledon level.

Modeling placental insufficiency in the macaque *in vivo*

For the final aim, we sought to model placental insufficiency in the rhesus macaque *in vivo*. We set out to demonstrate placental insufficiency through 1) inflammation, by intraplacental injection of the chemokine MCP-1, and through 2) oxidative stress, utilizing a transient cervical ligation of major uterine arteries to induce an ischemia/reperfusion injury at the placenta. While attempting to model inflammatory placental insufficiency, we found that an intraplacental injection of MCP-1 decreased pathological mineralization in the stroma of placental villi and resulted in healthy/normal maternal blood perfusion and fetal biometrics. These findings challenge historical conceptualizations of the role of potent chemokines in inflammatory disease and demonstrate that additional stimuli must be present for placental inflammatory injury to occur. When utilizing a transient cervical ligation to induce an IRI, we found that a 2 hr ligation followed by reperfusion resulted in significant increases in the proposed pathology and immunohistochemical staining we hypothesized would occur with such an injury. Although these results are preliminary, it appears that an IRI at the placenta is not only possible but may result in many of the pathologies often associated with placental insufficiency and APO, making it an exciting prospect for future studies of full-term pregnancy.

It is well established that placental development and function has a significant impact on human health [1,3]. Placental insufficiency pathology has been historically strongly associated with both altered maternal blood perfusion [17] and APOs [12]. However, little work has been done to directly elucidate their connection. Here, we

connect these ideas quantitatively, using placental pathology annotation and MRI-derived maternal blood monitoring. In addition, we have made great progress towards modeling macaque the placental insufficiency *in vivo*, as well as strengthening our ability for *in vitro* crossover during macaque pregnancy investigation. Taken together, this dissertation deepens our understanding of placental physiology and insufficiency in the primate placenta, as well as contributes to better modeling platforms of these conditions, thus contributing towards the goal of better understanding placental/pregnancy disease.

CHAPTER 2

AN IN VITRO MODEL OF EXTRAVILLOUS TROPHOBLASTS

Pregnant macaques, like humans, have a villous, hemochorial placenta in which trophoblasts invade and remodel maternal spiral arteries [36,49]. Further, macaque placentae possess all trophoblast cell subtypes [10] and express placenta-specific nonclassical MHC class I molecules Mamu-AG and Mamu-E (human homologs to HLA-G and HLA-E, respectively), and primate-specific chromosome miRNAs [50–53]. With the emergence of media formulations to support in vitro culture of trophoblast stem cells (TSCs) and organoids [54–56], our group successfully derived rhesus macaque TSCs that are capable of directed differentiation to either syncytiotrophoblasts (STBs) or extravillous trophoblasts (EVTs) [43]. These cell resources now enable the ability to evaluate an experimental condition in vitro prior to, or in parallel with, in vivo macaque pregnancy study.

Characterizing macaque EVTs in vitro

The characterization of *in vitro* differentiated macaque EVTs, however, has proven challenging given the lack of a known EVT-specific marker. In humans, surface HLA-G expression can identify EVTs [57], whereas in the macaque, Mamu-AG is expressed in both EVTs and STBs [51]. Additionally, macaque EVTs differentiated in vitro display morphological heterogeneity across cell lines [43]. Recent single-cell RNA sequencing and spatial transcriptomic studies of human [58–61] and macaque [62] placental tissues have refined knowledge of genes expressed by EVTs in early primate pregnancy. The in vivo expression profiles and consensus

markers of EVT sub-populations identified through these sequencing studies can now serve as a reference for improved characterization of the macaque in vitro trophoblast cells.

A low oxygen environment to improve macaque EVT categorization

In vivo differentiation of trophoblasts in early pregnancy occurs within a low oxygen environment [44], yet in vitro trophoblast cell cultures are typically maintained in standard atmospheric oxygen (20% O_2). A low oxygen environment can support in vitro modeling of early gestation [63], and in addition, may promote trophoblast lineage propagation and EVT differentiation in vitro [64–68]. The objectives of this study were to evaluate the impact of oxygen condition on macaque EVT differentiation in vitro and to improve the characterization of macaque TSC-differentiated EVTs. Macaque TSCs were differentiated to EVTs in either 20% or 5% O_2 followed by evaluation of gene and protein expression profiles. An experimental condition of 5% O_2 was selected for this study as it reflects an intermediate level between the 2-10% O_2 tension reported in early gestation human placenta [69,70] and is lower than the standard 20% O_2 typically used for TSC culture. There are no reports of intervillous oxygen tension in the macaque placenta, although ~1.5-2% intrauterine oxygen tension has been reported in nonpregnant females [71]. The 5% O_2 level may be higher than physiological levels in vivo, however, this level has supported early macaque embryo outgrowth development in vitro [72]. Overall, the results of this study validate the differentiation of macaque TSCs to EVTs, highlight

potential molecular differences between human and macaque EVTs, and suggest that differentiation in 20% O_2 supports in vitro differentiation of macaque EVTs.

METHODS

Ethical use, care, and breeding of macaques

All experimental procedures and tissue collections outlined here were performed in accordance with the NIH Guide for the Care and Use of Laboratory Animals and under the approval of the University of Wisconsin College of Letters and Sciences and Vice Chancellor Office for Research and Graduate Education Institutional Animal Care and Use Committee. Wisconsin National Primate Research Center (WNPRC) macaques were housed with compatible mates and monitored for breeding and menstruation. Date of conception was estimated based on initiation of the menstrual cycle, observation of copulation with presence of ejaculate, and ultrasound measurements of fetus and gestational sac.

TSC culture and differentiation to EVTs

Six TSC lines (n=3 of each XX and XY, Supplemental Figure 1A) were derived and cultured as previously described by Schmidt et al. [43]. In brief, TSCs were seeded to T75 flasks coated with 25 µg collagen-IV and cultured in TSC medium until they reached ~90% confluency. After three days of culture, TSCs from each cell line were collected for subsequent analyses and lifted to initiate the differentiation to EVTs. TSCs collected for RNA isolation were resuspended in 1 mL of TRIzol reagent (Invitrogen, cat no: 15596018) and frozen at -80°C until RNA extraction, and for the quantification of cellular protein, TSCs were placed into RIPA buffer (Thermo

Scientific, cat no: 89900) with HALT protease and phosphatase inhibitor cocktail (Thermo Scientific, cat no: 78440).

EVTs were differentiated in 37°C and 5% CO_2 and in either atmospheric (20% O_2) or low oxygen (5% O_2) conditions. The 5% O_2 condition was achieved by oxygen displacement with nitrogen gas and the percentage of O_2 was confirmed by gas analyzer (Bacharach Fyrite O_2 Analyzer) at the onset of experiments. EVT differentiation was initiated by seeding TSCs at a density of $1x10^5$ cells per well of a 6-well plate coated with 5 µg collagen-IV. Matrigel (Corning, cat no: 354234) was added at a concentration of 2% to the cell suspension immediately after plating. Media were formulated as previously described and exchanged on days 3 and 6 of culture with Matrigel supplemented at a final concentration of 0.5% [43,54]. Cell cultures were briefly exposed to atmospheric oxygen during imaging and at the time of media exchange on days 3 and 6 (≤ 10 minutes) of differentiation, as well as at imaging and collection on day 8 (≤ 20 minutes). After 8 days of culture, a portion of EVTs were resuspended in 1 mL of TRIzol reagent (Invitrogen, cat no: 15596018) and frozen at -80°C for later RNA extraction, a second portion was placed into RIPA buffer (Thermo Scientific, cat no: 89900) with HALT protease and phosphatase inhibitor cocktail (Thermo Scientific, cat no: 78440) for subsequent quantification of cellular protein, and a third portion was resuspended in Cellbanker 1 (Amsbio, cat no: 11910) to cryopreserve cells for flow cytometric analysis.

Cell conditioned media were collected from TSCs and EVTs prior to collection of cells. Media were collected on day 3 of TSC culture and day 8 of EVT differentiation and spun at 500 x g for 5 min to remove dead cells and debris, before storing at -80°C.

RNA extraction, cDNA synthesis and qRT-PCR

Cellular RNA was extracted from each individual cell line using a TRIzol-chloroform extraction protocol as previously described [43]. RNA was extracted from 1) TSCs and subsequent EVTs differentiated in standard oxygen (n=6 cell lines, RNA was pooled from 2-4 passages (TSCs) or differentiations (EVTs) for each cell line), 2) EVTs differentiated in 20% and 5% O_2 (n=6 cell lines), and 3) and EVTs (20% O_2) differentiated from the same TSC line (n=6 cell lines, RNA from 2-4 differentiations per cell type was pooled for each cell line). A SuperScript III First-Strand Synthesis kit (Invitrogen, ThermoFisher Scientific, cat no: 18080-051) was used to synthesize cDNA. A total of 1 µg of RNA was combined with kit reagents to perform the reactions according to manufacturer suggestions. cDNA was combined with iQ SYBR green master mix (BioRad, cat no: 1708882), gene-specific primers, and RNase-free water. Reactions were run on a Roche LC 96 instrument in triplicate with no template negative controls. Beta-actin (ACTB) was used as an internal reference for comparison of expression levels. The $2^{-\Delta\Delta Cq}$ method [73] was used to calculate the fold change in expression for each cell line and the mean fold change for all lines was graphed with the standard error of the mean. A paired t-test was applied to the ΔCq values for each gene and compared between cells of each cell line (i.e. EVTs versus TSCs, 20% versus 5% O_2 EVTs).

Flow cytometry

Cell staining and flow cytometry analyses were conducted using previously published methods [43]. Briefly, cryopreserved cells for each cell line (i.e., n=6 individual cell lines in which EVTs were differentiated in 5% and 20% O_2) thawed, washed, and filtered (35 μm) before staining with viability marker Ghost Red 780 (Tonbo Biosciences, cat no: 13-0865). The cells were then stained with surface antigen antibodies against Mamu-AG, Mamu-E, and NCAM1. Cells were then fixed and permeabilized using the Foxp3 transcription factor staining buffer kit (eBioscience, cat no: 00-552-3-00) according to the manufacturer's guidelines, followed by intracellular staining for Ki-67, cytokeratin 7/8, and vimentin. Unstained cells, macaque fibroblast control cell lines, and compensation controls using cell lines or UltraComp eBeads (eBioscience, cat no: 01-2222-42) were prepared in parallel. EVTs differentiated from the same TSC line were analyzed within the same experiment. Two experiments were run in total, one analyzed on a five laser BD LSRII (BD Biosciences) and the other analyzed on a BD FACSAriaII (BD Biosciences). Results were further analyzed using FlowJo v10.8 software (FlowJo LLC). Cells were gated to eliminate doublets, dead cells, and cellular debris. The proportion of positively stained cells and the median fluorescence intensity (MFI) were calculated for live, single cells in each channel. A paired T-test was performed to measure the effect of 5% vs. 20% O_2 on marker expression within the individual cell lines.

Immunohistochemistry

Paraffin-embedded rhesus macaque placenta tissues collected on gestational days (GDs) 19, 21, 24, 25, 36, 37, 55 and 58 were obtained from Dr. Golos' laboratory. To validate the mCG antibody, archived human term placental tissue specimens (n=2) with representative syncytiotrophoblast were also evaluated. The tissues were fixed in 4% paraformaldehyde, dehydrated in ethanol, and embedded in paraffin. Immunohistochemistry was performed on 5 μm thick paraffin sections as previously described [74]. Tissue sections were incubated with primary antibodies against NCAM1, Ki-67, mCG or KRT7/8. Simultaneously, serial sections were incubated with appropriate negative control mouse IgGs (IgG1 or mouse IgG2a) at the same concentration as the respective primary antibody. The slides were then incubated with a goat anti-mouse polymer-horseradish peroxidase secondary antibody, MACH 2 (Biocare Medical, Concord, CA, USA. Staining was developed for 45-120 s with Betazoid Diaminobenzidine (DAB) chromogen (Biocare Medical, Concord, CA, USA). Brightfield photomicrographs were taken using a Nikon Eclipse Ti2 microscope (Nikon Instruments Inc., Melville, NY, USA) with NIS-Elements AR software version 5.02.006 (Nikon Instruments Inc., Melville, NY, USA). Scale bars were added using NIS-Elements AR.

Bioassays to detect hormones and secreted analytes

Blood samples were drawn from seven non-pregnant and six pregnant rhesus macaques initially at GD 17-23 and then subsequently again at GD 36-38 to assess mCG in maternal circulation. Gestational day was estimated based on gestational

sac and crown rump length measurements obtained through ultrasound examination [75]. A 3 ml blood sample was collected into a clot activator tube and serum was isolated by centrifugation for 15 min at 1,400 x g. mCG concentrations in maternal serum and cell conditioned media were analyzed using a radioimmunoassay method as previously described [43,76].

Progesterone (P4) levels secreted by EVTs were measured via LC-MS/MS by the WNPRC Assay Services Unit using methods previously described [77]. In brief, culture media samples underwent extraction and were then analyzed on a QTRAP 5500 quadruple linear ion trap mass spectrometer (AB Sciex) equipped with an atmospheric pressure chemical ionization source. The lower limit of quantification was 7.0 pg/ml. EVT conditioned media was analyzed for secreted levels of matrix metallopeptidase 2 (MMP2) using a Monkey MMP2 ELISA Kit (Abcam, cat no: ab269561), as previously described [43] and run in accordance with assay protocol, in duplicate, at 1:100 and 1:300 dilutions. Data in assay range were averaged for a final concentration. Cellular secretions (i.e., mCG, P4, and MMP2) were normalized to total cellular protein using a Micro BCA Protein Assay Kit (ThermoFisher Scientific, cat no: 23235) as previously described [43].

Statistical analyses

Statistical analyses were performed using GraphPad Prism software. Paired t-tests were used to assess the difference between cells from the same line (i.e., TSCs vs EVTs; EVTs 20% vs 5% O_2; EVTs vs STs). All data are graphed as the mean and the standard error of the mean for each parameter and individual data points for each

cell line analyzed are also plotted. A Kruskal-Wallis tests with Dunn's multiple comparisons test was performed to compare cell secretion levels.

RESULTS

EVTs display similar morphologies regardless of oxygen condition

Six TSC lines were propagated in 20% O_2 prior to undergoing an 8-day EVT differentiation protocol with culture in either 20% or 5% O_2 (Figure 2.1A). Cell morphology was evaluated on days 3, 6, and 8 of differentiation at the time media was exchanged (Figure 2.1B). Macaque TSC-differentiated EVT morphology differed from that of human TSC-differentiated EVTs (less sprawling with fewer spindly projections) [54,78] and varied across cell lines, showing greater consistency within an individual line, regardless of oxygen condition.

Differentiation of EVTs in 5% O_2 induces *HIF1A* expression

The effect of oxygen on EVT differentiation is thought to be largely governed by HIF expression [79]. The hypoxia inducible factor (HIF) complex is a heterodimer comprised of an alpha (i.e., either HIF1A or HIF2A) and beta (i.e., HIF1B, also known as ARNT) subunit and functions as a crucial upstream mediator of a cell's response to decreased oxygen [80,81]. Expression of oxygen sensitive genes *HIF1A* and *HIF2A* (also known as *EPAS1*) were compared between TSCs and EVTs (20% O_2) and between EVTs differentiated in 20% versus 5% O_2 by qRT-PCR. Increased expression of *HIF1A* was observed in TSCs, whereas *HIF2A* was increased in EVTs differentiated in 20% O_2 (Figure 2.2A). Additionally, HIF complexes promote *KDM3A* expression, a histone demethylase that helps regulate trophoblast invasion [82,83].

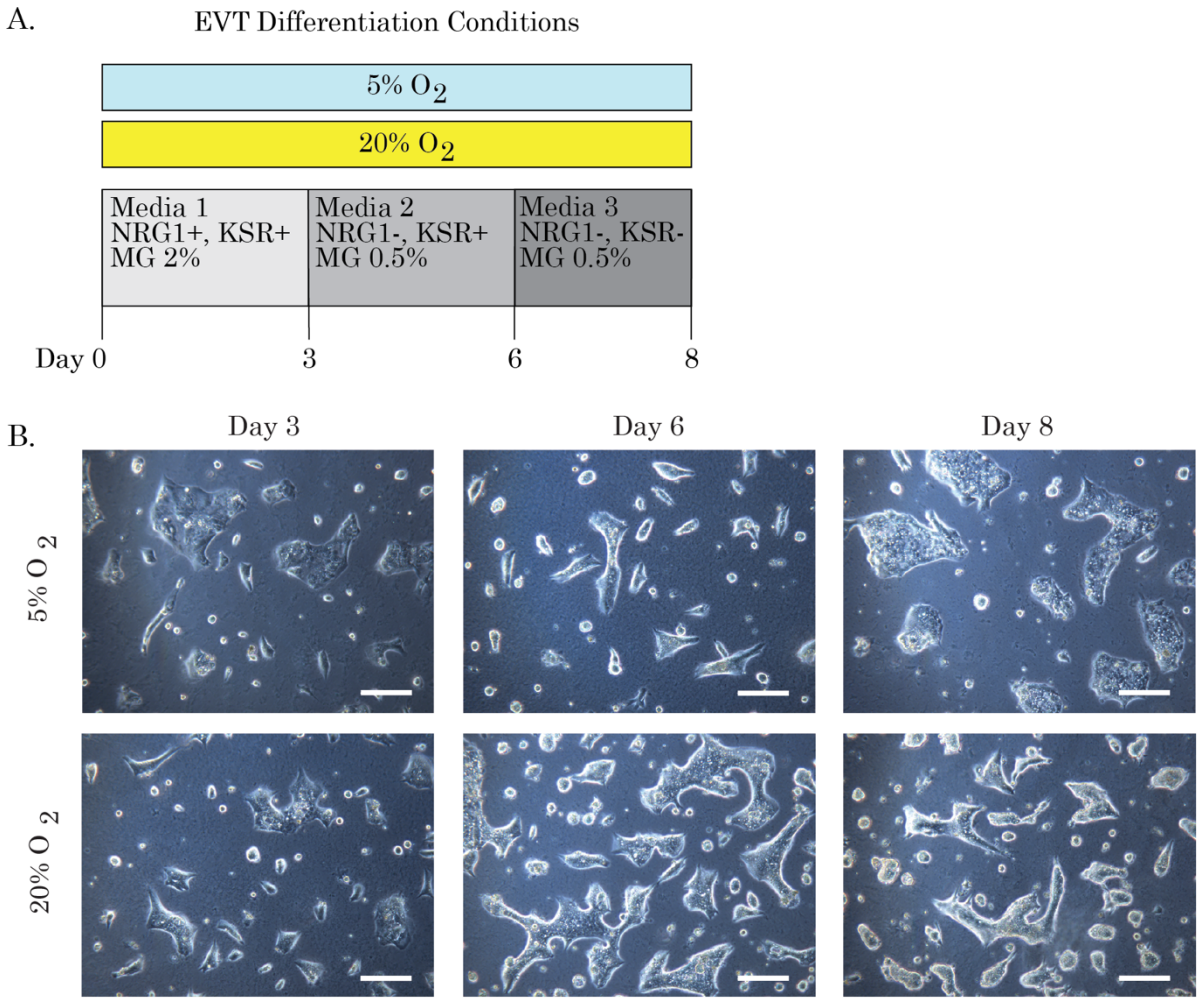

Figure 2.1. Overview of EVT differentiation from TSCs. A) Timeline and conditions for EVT differentiation. TSCs were cultured in either 20% or 5% O2 beginning on day 0 in EVT Medium 1 containing neuregulin 1 (NRG1) and knockout serum replacement (KSR) with matrigel (MG) added at 2% by volume. On day 3, EVT media was exchanged for Medium 2 lacking NRG1, and MG was added at 0.5% by volume. On day 6, EVT media was exchanged for Medium 3 lacking NRG1 and KSR, with MG added at 0.5% volume. B) Representative images of EVTs derived from rh121118 TSCs that were differentiated in either 20% or 5% O2. Scale bar represents 200 µm.

KDM3A was significantly upregulated in EVTs differentiated in 20% O_2 compared to TSCs. When evaluating EVT expression of oxygen sensitive genes, *HIF1A* expression was significantly increased in 5% O_2 EVTs (Figure 2.2A). *HIF1A*, *HIF2A*, or hypoxia directly, stimulates *PAI1* (also known as *SERPINE1*) expression [84,85], a gene associated with decreased invasion of EVTs [86]. The expression of *PAI1* was

comparable between TSCs and EVTs, and similarly unchanged upon differentiation in 5% O_2. Furthermore, there were no significant differences in *HIF2A* or *KDM3A* expression between EVTs differentiated in either oxygen condition (Figure 2.2A).

TSC-differentiated EVTs activate expression of EMT-inducing genes

Villous cytotrophoblasts (vCTBs) undergo an epithelial to mesenchymal transition (EMT) as they differentiate into EVTs [87]. This consists of phenotypic and physiological changes, as cells transition from a polar, adherent epithelial cell to a more migratory, invasive mesenchymal one [88]. Several well-defined transcriptional regulators contribute to EMT induction [87,88]. The expression of EMT inducers was compared between EVTs differentiated in 20% O_2 and TSCs by qRT-PCR (Figure 2.2B). The expression of EMT-inducing genes *SNAI1*, *TCF4*, *TGFB1*, and *WNT5A* increased as expected with TSC differentiation to EVTs. The differentiation of EVTs in 20% versus 5% O_2 did not significantly impact the expression of *SNAI1*, *TCF4*, *TGFB1*, *TWIST1*, or *WNT5A* (Figure 2.2B).

TSC-derived EVTs upregulate genes commonly associated with EVTs

Human EVTs are characterized by increased expression of HLA-G [57,89], expression of EVT-promoting transcription factors [90], evidence of an EMT (through cadherin [87] and integrin switching [91]), and changes in NOTCH signaling [92]. Macaques lack interstitial EVTs [93], hence the macaque intra-placental EVT subpopulations include EVTs within the cell column (cell column trophoblasts [CCTs]), trophoblastic shell, and endovasculature (eEVTs). To improve the molecular

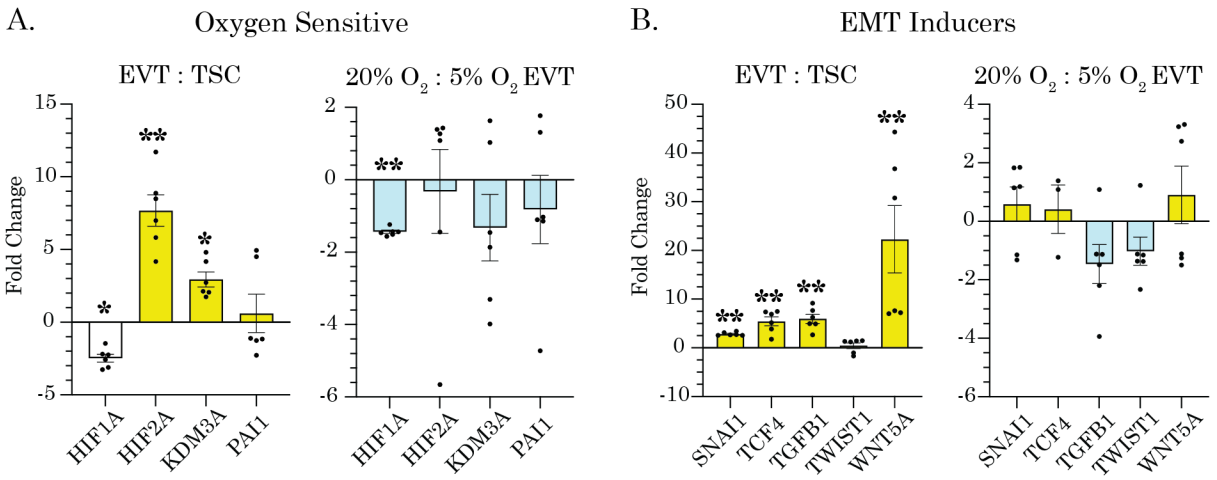

Figure 2.2. Gene expression profiling of TSC-differentiated EVTs by qRT-PCR. The mean fold change in expression between EVTs differentiated in 20% O2 and TSCs, and EVTs differentiated in 20% versus 5% O2 for genes that are oxygen sensitive (A), induce an EMT (B). Positive fold changes indicate higher expression in EVTs differentiated in 20% O2 (yellow) compared to TSCs or 5% O2. Negative fold changes indicate higher expression in TSCs (white), 5% O2 EVTs (blue), or ST (green) compared to 20% O2 EVTs. The mean fold change in expression and the standard error of the mean are graphed for each gene and individual data points for each cell line are also plotted. Three to six cell lines were compared for each marker. The asterisks denote the following significance levels: *p<0.05, **p<0.001, ***p<0.0001.

characterization of macaque TSC-differentiated EVTs, the expression of known human markers of CCTs and EVTs was assessed by qRT-PCR. Gene expression was first compared between TSCs and EVTs differentiated in 20% O_2, as this is the standard differentiation condition previously demonstrated in human and macaque TSCs [43,54]. Several known human EVT-associated markers were significantly upregulated upon differentiation from TSCs, including *ITGA1*, *ITGA5*, *CDH5* and *ASCL2* (Figure 2.3A). In addition, macaque-specific *MAMU-AG* was significantly higher in EVTs compared to TSCs (Figure 2.3A). *ITGA2*, a CCT marker [94], was significantly increased in TSCs compared to EVTs in 20% O_2. *CDH1* is a adhesion molecule, shown to decrease in expression in an EMT, as well as in distal EVT

populations [87]. Interestingly, a small, yet significant increase in *CDH1* was observed in EVTs compared to TSCs (Figure 2.3A).

EVTs differentiated in 20% O_2 more highly express *NOTCH2*

In human first trimester placenta tissue, *NOTCH1* is highly expressed in immature EVTs of the proximal cell column [95], while *NOTCH2* expression increases in mature EVTs of the distal cell column and endovasculature [96]. When comparing between differentiation in standard oxygen versus low oxygen, the EVTs differentiated in 20% O_2 had significantly elevated expression of *NOTCH2*, whereas those differentiated in 5% O_2 had significantly higher expression of *NOTCH1* (Figure 2.3B). EVTs differentiated in 5% O_2 retained higher expression of *CDH1* and showed

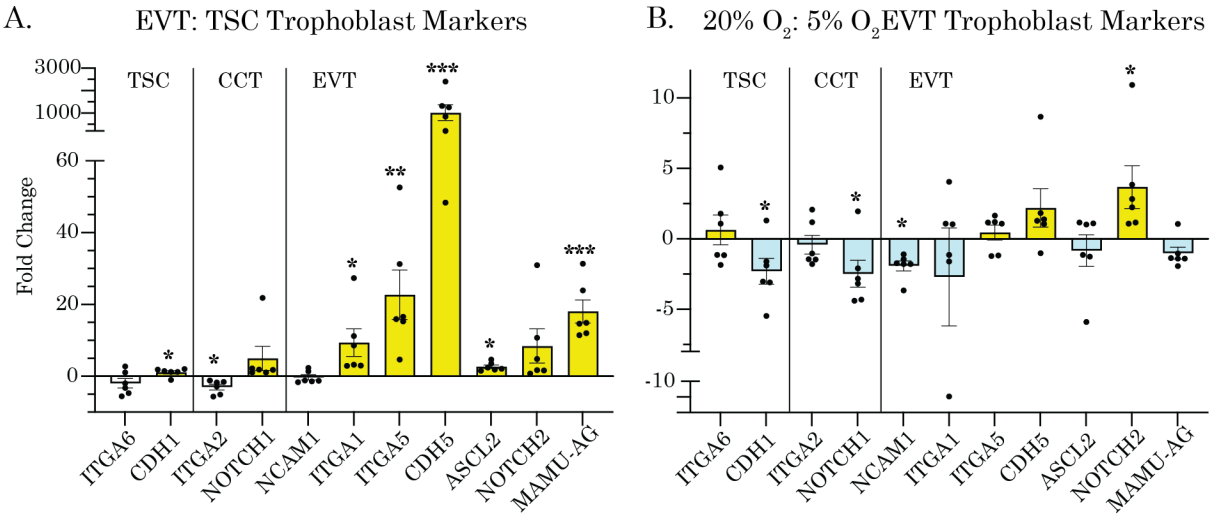

Figure 2.3. The mean fold change in expression between A) EVTs differentiated in 20% O2 and TSCs, and B) EVTs differentiated in 20% versus 5% O2 for genes that are established TSC, cell column trophoblast (CCT), and EVT markers. Positive fold changes indicate higher expression in EVTs differentiated in 20% O2 (yellow) compared to TSCs or 5% O2. Negative fold changes indicate higher expression in TSCs (white), 5% O2 EVTs (blue), or ST (green) compared to 20% O2 EVTs. The mean fold change in expression and the standard error of the mean are graphed for each gene and individual data points for each cell line are also plotted. Three to six cell lines were compared for each marker. The asterisks denote the following significance levels: *p<0.05, **p<0.001, ***p<0.0001.

increased *NCAM1* expression compared to EVTs differentiated in 20% O_2. The expression of *ITGA6*, *ITGA2*, *ITGA1*, *ITGA5*, *CDH5*, *ASCL2* and *MAMU-AG* were not significantly different between the two EVTs oxygen conditions (Figure 2.3B).

EVTs highly express Mamu-AG regardless of oxygen condition

The expression of intracellular and surface membrane proteins was investigated by flow cytometry. The proteins analyzed included: cytokeratin 7/8 (KRT 7/8, epithelial trophoblast marker [97]), vimentin (a mesenchymal marker [98]), Ki-67 (a cell proliferation marker [99]), Mamu-AG, Mamu-E, and NCAM1 (a cell adhesion protein expressed by EVTs [100,101]) (Figure 2.4). Regardless of oxygen condition, approximately 98% of the EVTs expressed KRT 7/8 (Figure 2.4A), while less than 1% of EVTs expressed vimentin (not included in Figure 2.4 given the low proportion of positive cells). Human EVTs express the non-classical MHC cell surface glycoprotein HLA-G [57,89], whereas macaques express the homolog Mamu-AG in both STs and EVTs [102]. Mamu-AG and NCAM1 were uniformly (>95%) expressed in EVTs differentiated in 20% or 5% O_2 (Figure 2.4A). Ki-67 expression was comparable between oxygen conditions and consistent between cell lines, with positive expression in 24-50% of 5% O_2 EVTs and 27-44% of 20% O_2 EVTs. The median fluorescence intensities for the proteins evaluated were similar between EVTs, except for Mamu-E, which was more highly expressed by EVTs differentiated in 5% O_2 (Figure 2.4B).

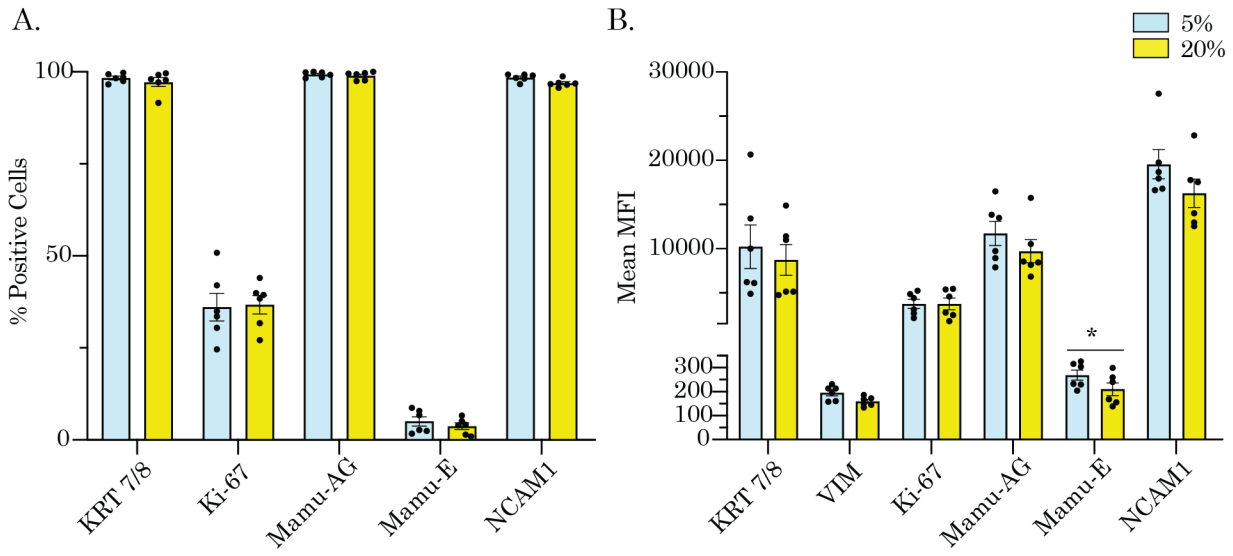

Figure 2.4. Flow cytometric analysis of TSC-differentiated EVTs. A) Percent of the total cells that positively stained for each protein. B) Median fluorescence intensity (MFI) of each protein. The mean and the standard error of the mean for each parameter and individual data points representing each cell line analyzed are also plotted (n=6 cell lines). The asterisk denotes $p<0.05$.

Ki-67 and NCAM1 IHC expression in early gestation macaque placenta

To interpret the in vitro protein expression profiles of Ki-67 and NCAM1 in TSC-differentiated EVTs, in vivo expression of these markers was evaluated in early gestation rhesus macaque placentae by immunohistochemistry. Ki-67 staining was observed in vCTBs as well as trophoblasts in the proximal regions of the cell columns, however, fewer cell column trophoblasts expressed Ki-67 in the GD 55 and 58 placental tissues. eEVTs did not express Ki-67 at the early gestational days evaluated, as expected (Figure 2.5).

In humans, expression of NCAM1 is notably observed in eEVTs [58,100,103] and to a lesser extent in the trophoblastic shell [100]. Here, macaque placental tissue sections were evaluated for comparison (Figure 2.6). In the macaque early gestation placenta, NCAM1 was highly expressed in trophoblasts of the cell columns and

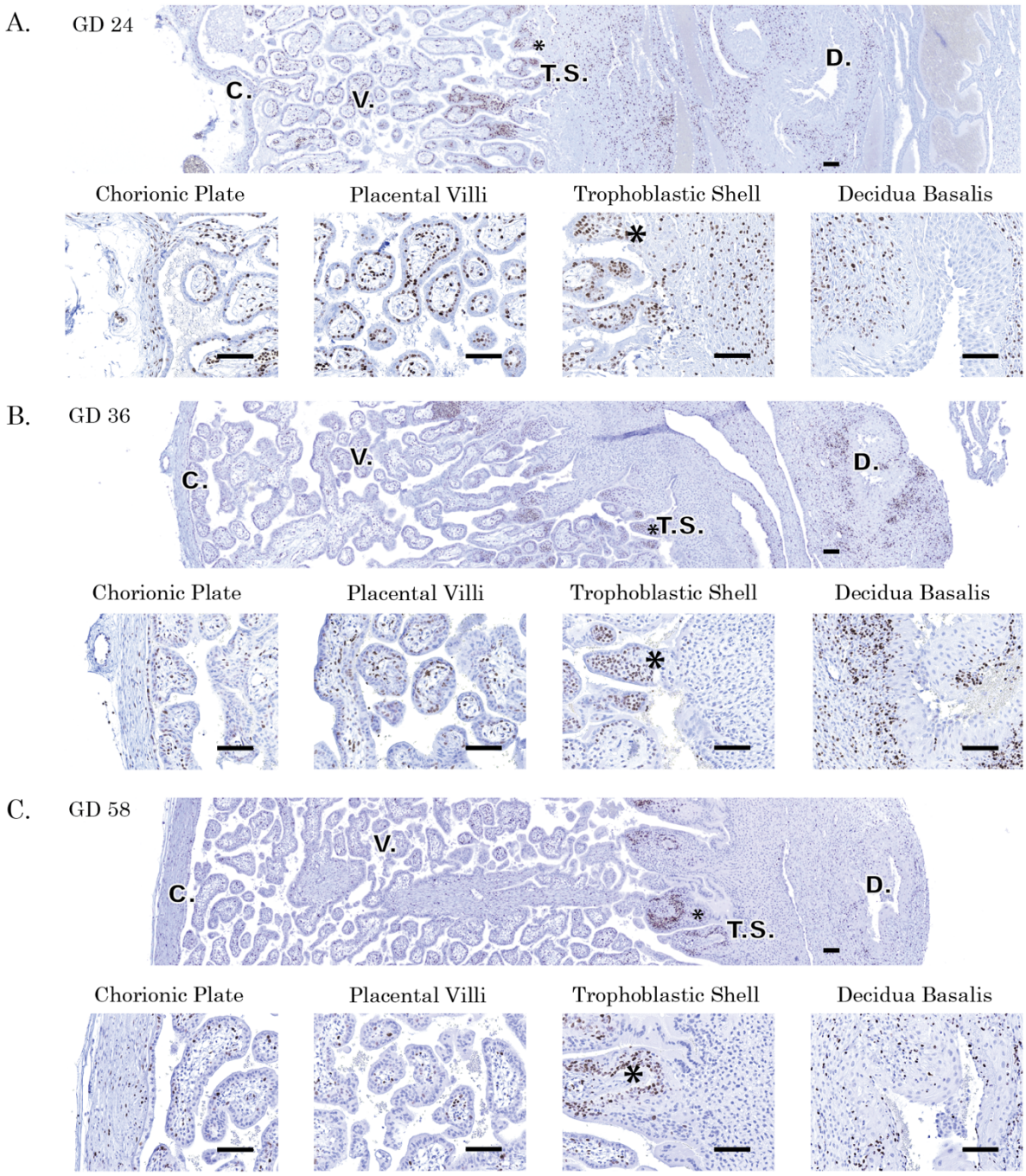

Figure 2.5. Immunohistochemical analysis of Ki-67 expression in macaque trophoblasts. Representative images of Ki-67 immunostaining in rhesus macaque placentas at gestational day (GD) A) 24, B) 36, and C) 58. The 4x magnification scans (top) depict the full thickness placental architecture of each sample. Sub-tissue abbreviations indicate the location of 20x insets (bottom), representative of the chorion (C), villi (V), trophoblastic shell (TS), and decidua (D). An asterisk denotes a representative cell column. The scale bars represent 100 µm.

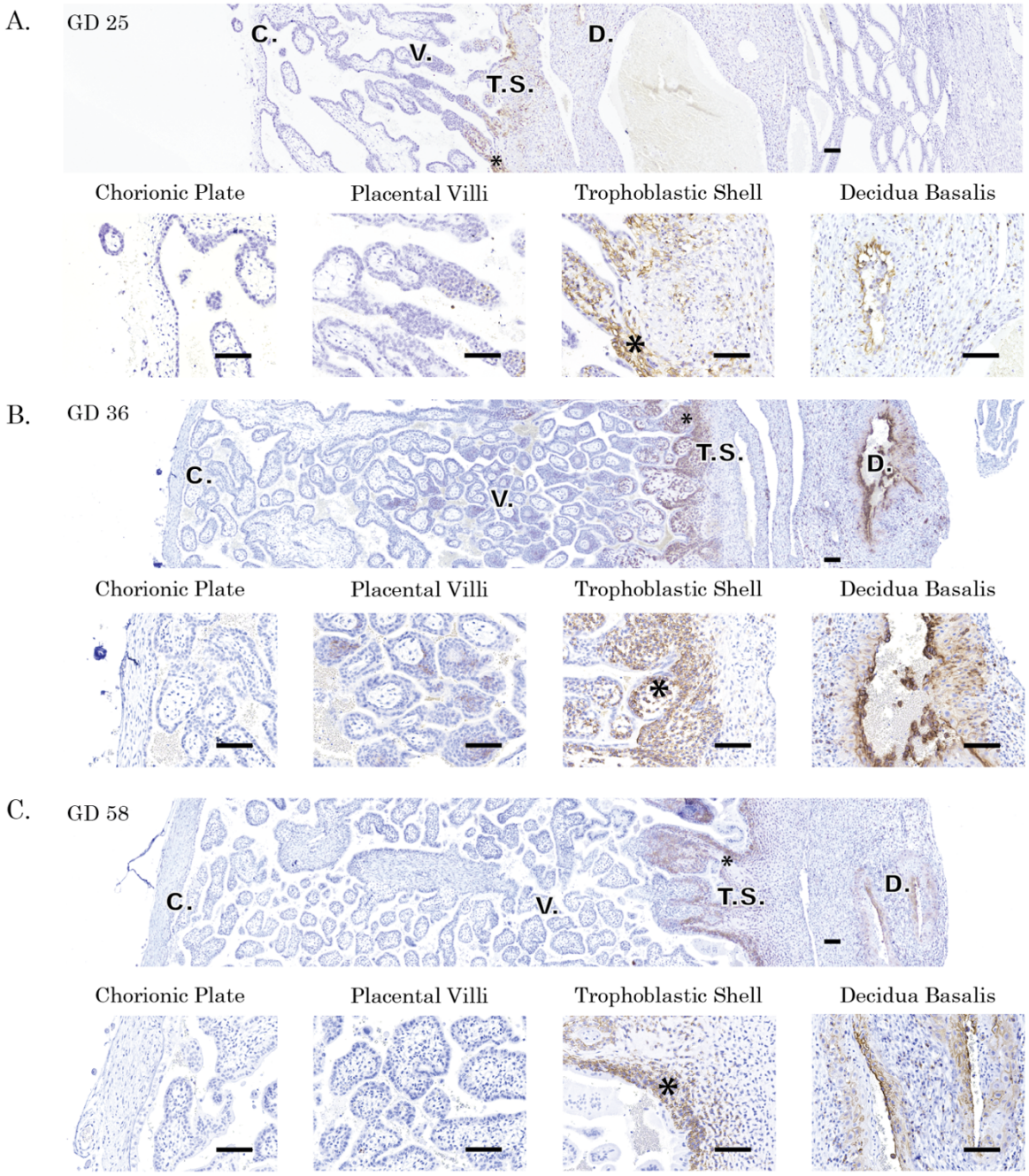

Figure 2.6. Immunohistochemical analysis of NCAM1 expression in macaque trophoblasts. Representative images of NCAM1 immunostaining in rhesus macaque placentas at gestational day (GD) A) 25, B) 36, and C) 58. The 4x magnification scans (top) depict the full thickness placental architecture of each sample. Sub-tissue abbreviations indicate the location of 20x insets (bottom), representative of the chorion (C), villi (V), trophoblastic shell (TS), and decidua (D). The asterisk denotes a representative cell column. The scale bars represent 100 µm.

trophoblastic shell as well as by eEVTs, with no expression of NCAM1 in trophoblasts in the chorionic plate or villi.

EVTs secrete pregnancy-associated mCG, P4, and MMP2

Macaque TSC-differentiated EVTs secrete pregnancy-associated hormones, mCG and P4, as well MMP2, a collagenase that breaks down maternal extracellular matrix allowing for cellular invasion [43]. The expression of CGA and CGB (reflecting CG alpha and beta subunits, respectively) was significantly elevated in EVTs differentiated in 20% O_2 compared to TSCs as well as in EVTs differentiated in 20% compared to 5% O_2 (Figure 2.7A). The secreted levels of P4 and MMP2 into culture media varied but were comparable between TSCs and EVTs. The secretion of mCG into culture media was significantly higher in 20% O_2 EVTs compared to TSCs (Figure 2.7B).

The detection of rhesus macaque mCG in maternal circulation has previously been shown to be restricted to early gestation [104], thus in our initial report the expression of mCG by TSC-differentiated ST and EVT suggested that these cells were reflective of an early gestational age [43]. To assess the in vivo expression profile of mCG in macaque EVTs, first, the window for mCG detection in maternal circulation was profiled (Figure 2.7C). mCG was present in circulation at GD 17 and then was completely undetectable at GDs 36-38 (Figure 2.7C). In addition, immunohistochemical analysis was performed on early gestation macaque placental tissues, using the same mCG antibody as used for detection in maternal circulation and was confirmed to stain ST of human term placenta. Analysis of macaque

placental tissues revealed mCG staining in endovascular EVTs at GD 19 (Figure 2.7D) as well as in the cells of the anchoring columns, trophoblastic shell and ST, as expected at GDs 21 and 24 (Figure 2.7E).

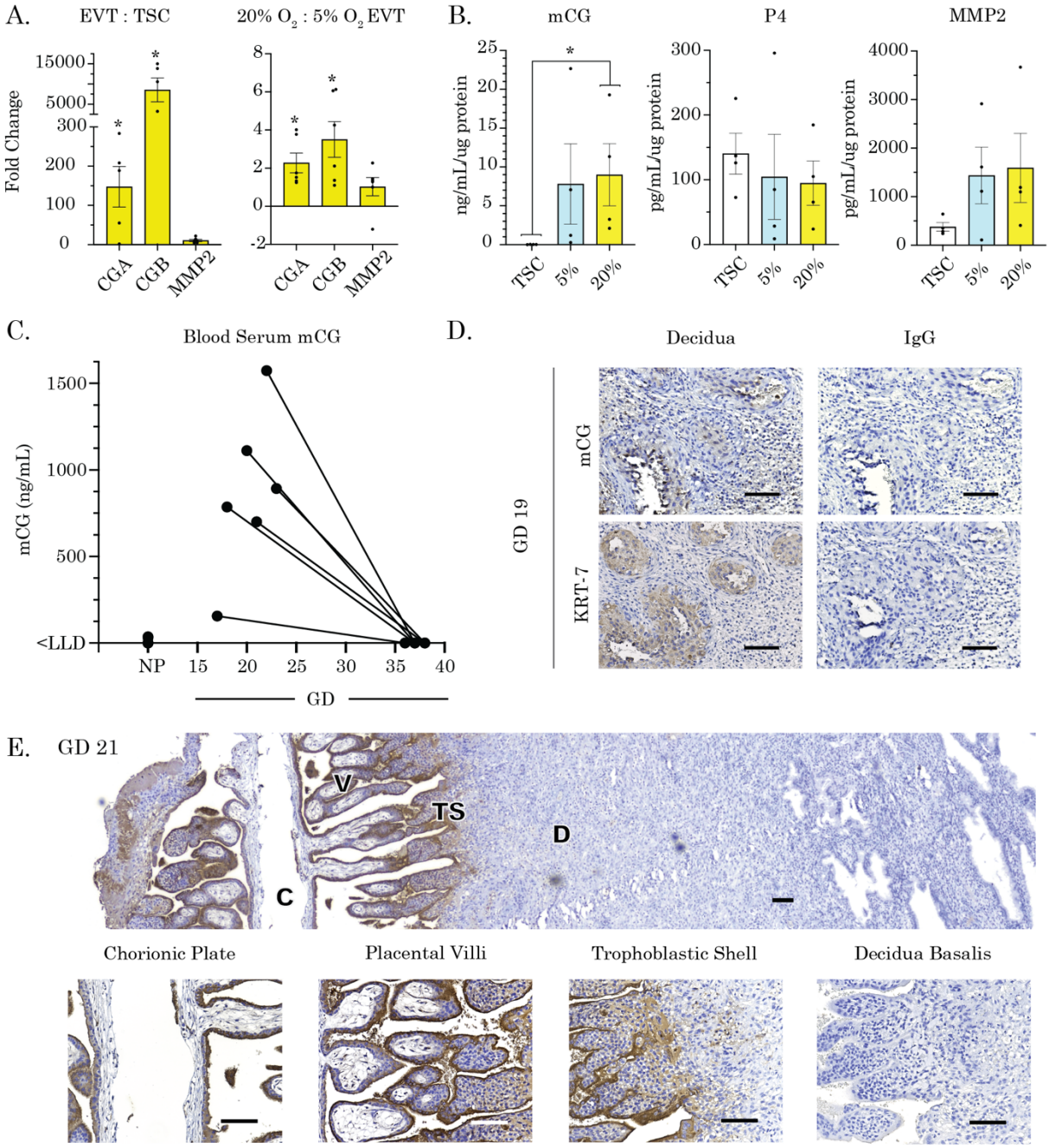

Figure 2.7. Expression and secretion of pregnancy hormones and MMP2 by EVTs. A) The mean fold change in expression of CGA, CGB and MMP2 between EVTs differentiated in standard 20% O2 and TSCs and the mean fold change in expression between EVTs differentiated in 20% versus 5% O2. Positive fold changes indicate higher expression in EVTs differentiated in 20% O2 (yellow) compared to TSCs or 5% O2 (n=6 cells lines). B) Cellular secretion of mCG, progesterone (P4) and MMP2 into cell culture media normalized by total cellular protein (n=4 cells lines). C) Blood serum levels of mCG in early macaque pregnancy. D, E) Immunohistochemical analysis of mCG in macaque placental tissues. Representative images of the chorion (C), villi (V), trophoblastic shell (TS), and decidua (D). For A and B, the data is presented as the mean and standard error of the mean for each parameter and in addition, individual data points are plotted for each cell line. An asterisk denotes a significance level of $p<0.05$. GD: gestational day.

DISCUSSION

The present study's objectives were to enhance our *in vitro* macaque placental modeling system. Specifically, we sought to characterize the morphological, gene, and protein profiles of macaque TSC-differentiated EVTs, and to assess whether low oxygen better supports EVT differentiation in vitro. Differentiation in 5% O_2 did not abrogate the morphological differences observed across macaque EVTs. EVTs differentiated in lower oxygen had elevated *HIF1A* expression and retained expression profiles more similar to TSCs or CCTs, whereas EVTs differentiated in standard oxygen more highly expressed *NOTCH2*, a gene expressed by human eEVTs [96]. Altogether, the differentiation of macaque TSCs to EVTs in standard 20% O_2 led to the upregulation of EMT-inducing genes and genes highly expressed by human EVTs *in vivo*. These data further support the identity of macaque TSC-differentiated EVTs despite the observed morphological heterogeneity.

Differential *HIF1A* and *HIF2A* expression in low oxygen EVTs

In vitro culture of human vCTBs in hypoxic conditions has promoted EVT differentiation with similar [45], or increased [64,105] HLA-G expression when compared to an atmospheric oxygen condition. Oxygen-sensitive HIFs activate genes that induce an EMT-like process, including transcription factors that are highly expressed by EVTs [78]. For example, both *HIF1A* and *HIF2A* expression trigger increased *SNAI1* [78,106], an EMT inducer, that subsequently represses *CDH1* [27] resulting in increased *ITGA5* expression [107] – an integrin highly expressed in cell column EVTs [91]. Here, macaque TSCs and 5% O_2 EVTs had elevated levels of

HIF1A, whereas *HIF2A* was more highly expressed in 20% O_2 EVTs. We believe this points to increased relative maturity in our 20% O_2 EVTs, as supported by previous studies demonstrating increased *HIF1A* expression in EVT progenitors [108] with a shift to increased *HIF2A* expression in TSC-differentiated EVTs [78]. A limitation of this study is that HIF expression was not evaluated at the protein level, and additionally, some oxygen sensitive genes (i.e., *ASCL2*, *KDM3A*, and *PAI1*) showed variable expression levels between EVTs differentiated in 5% versus 20% O_2.

NOTCH expression and EVT maturity

Macaque EVT differentiation in low oxygen resulted in increased *HIF1A* expression, and in agreement with previous human in vitro studies, promoted the differentiation of a cell population that expressed markers consistent with progenitor or immature EVTs within the cell column [45,68,79]. *NOTCH1* has been observed to increase with hypoxia [95] and was highly expressed in human trophoblasts primed for EVT lineage in vivo and in vitro [58]. In contrast, *NOTCH2* expression has shown to be increased in eEVTs [58,92,96] and associated with trophoblast invasion [109] and diminished proliferation [58,95,110]. Macaque EVTs differentiated in 20% O_2 had elevated *NOTCH2* expression, whereas those differentiated in 5% O_2 showed increased *NOTCH1*, suggesting a more mature EVT subpopulation with higher oxygen. It is plausible that upon differentiation there is heterogeneity in the subtypes of EVTs produced and/or that there is variance in the differentiation capacity across individual lines. Although expression of EVT genes varied across cells lines, there was less variance in the expression of the selected protein markers evaluated.

MHC, Ki-67, and mCG expression in low oxygen

The evaluation of single cell protein expression, paired with immunohistochemical staining of early placental tissues, was used to further interpret expression profiles of *in vitro* TSC-differentiated EVTs. TSC-differentiated EVTs presented near uniform Mamu-AG expression by flow cytometry, a MHC class I marker expressed by both ST and EVTs in macaques [51,102,111]. Ki-67 expression was evaluated to characterize the proportion of proliferating cells within *in vivo* EVT populations and in our TSC-differentiated EVTs. CCTs and trophoblastic shell trophoblasts *in vivo* display some cellular proliferation, whereas eEVTs do not. The *in vitro* TSC-differentiated EVTs retained a proportion of Ki-67 positively stained cells regardless of oxygen condition or cell line; this EVT subpopulation could be reflective of the Ki-67 expressing cells observed within the trophoblastic shell of the in vivo macaque placenta. Elevated intensity of Mamu-E expression in 5% O_2 may indicate EVT immaturity, as previous staining *in vivo* demonstrated high expression by vCTBs and only moderate expression by mature EVTs [52].

Increased EVT maturity in 20% O_2 is further evidenced by elevated mCG expression and secretion in 20% O_2 EVTs, as increased mCG in macaque pregnancy [104,112,113] coincides with the onset of eEVT invasion *in vivo* [93]. mCG staining was observed in macaque cell columns and eEVTs; a finding in agreement with the pattern of CG staining observed in human placental tissues at 8-12 weeks of gestation [114] and evidence of CGB8 expression in 8-week human EVTs [115]. The term human placenta tissues used to validate the mCG antibody in the present study

lacked representative populations of anchoring cell columns, interstitial EVTs and eEVTs, hindering the ability to evaluate mCG expression in these trophoblast populations.

NCAM1 as an EVT-specific surface marker in the rhesus macaque

This study revealed potential differences in EVT marker expression between macaques and humans. Macaque EVT invasion is shallow compared to humans, with the lack of interstitial trophoblast and giant cell populations [36]. *In vivo* human placental expression of NCAM1 has shown to be largely restricted to eEVTs [58,100], with staining of the trophoblastic shell limited to regions adjacent to spiral arteries [100]. This is markedly different from the NCAM1 staining we observed along the entirety of the trophoblastic shell, as well as within the spiral arteries of the macaque placenta; a staining pattern in agreement with previous macaque findings [101]. The substantial shell of trophoblasts lining the decidua in macaques [36] seem to reflect a diminished degree of EVT invasion, and further, may be indicative of molecular differences observed in relation to human trophoblasts. NCAM1 was uniformly expressed by TSC-differentiated EVTs regardless of oxygen condition. Hence, the TSC-differentiated EVTs may be reflective of the EVTs within the trophoblastic shell, a region comprised of dense cell layers that are non-motile and less invasive.

Macaque EVT differentiation validation

The EVT differentiation protocol in standard oxygen as described by Okae et al. for human TSCs [54] can subsequently be used to differentiate macaque TSCs to EVTs. A notable difference between the Okae et al. [54] protocol and our protocol is

the lack of passage of the cells on day 6 of differentiation, which could explain the dissimilarity in observed morphology between human and macaque TSC-differentiated EVTs. Here, we show further validation of EVT identity across multiple TSC lines originally derived from placentas of various gestation days and of both XX and XY representation. The expression of EMT-inducing genes, *WNT5A*, *TGFB1*, and *TCF4* was elevated in EVTs compared to TSCs. Increased expression of macaque-specific *MAMU-AG* as well as human EVT markers *CDH5*, *ITGA1*, *ITGA5*, and *ASCL2* provides further evidence that macaque TSCs undergo EVT differentiation. The observations of the present study are largely consistent with our previous study, with a couple exceptions. *TCF4* was previously shown to be decreased in EVTs in our previous study [43], however, the primers amplified the gene *TCF4* rather than *TCF7L2* (alias *TCF4* and the gene amplified in the present study), the relevant gene involved in EVT differentiation. The level of progesterone secreted by EVTs was also relatively lower in the present study and may be attributable to the difference in the method used for analysis.

Study limitations

The present study design warrants highlighting limitations with respect to the low oxygen culture condition. When imaging, feeding, and collecting cells, a hypoxic chamber was not utilized – this resulted in exposing 5% O_2 EVTs to atmospheric conditions for short periods (< 10 minutes) on days 3, 6, and 8 of differentiation. Additionally, we did not pre-condition TSCs that were subsequently differentiated into EVTs at 5% O_2. These factors, while uniformly applied to all cell lines evaluated,

may have pre-conditioned the cells or altered the growth/expression trajectory of EVTs.

Conclusions

In conclusion, the results of this study confirm the identity of macaque TSC-differentiated EVTs, highlight the ability of macaque TSCs to undergo an EMT-like process during EVT differentiation, and identify key differences emerging between human and macaque trophoblasts. Further, the differentiation in atmospheric oxygen, as is standard for most cell cultures, supported the differentiation of a more mature population of EVTs, while immature EVT populations arose when differentiation was performed in low oxygen. The differentiation process likely results in heterogeneity, as evident by variation in gene expression profiles that may be reflective of different EVT subpopulations and maturity. Additionally, it is possible that the immature EVT populations derived here may be representative of eEVTs populations found in cases of placental insufficiency [47] – categorized by their shallow invasion and incomplete remodeling of spiral arteries [11]. However, as there is current uncertainty regarding the role of NOTCH signaling in APO eEVTs [46,47], additional single cell gene and protein expression analyses are needed to better define APO eEVTs *in vivo*, as well as EVT heterogeneity upon *in vitro* differentiation of TSCs.

The use of human and macaque single-cell RNA-seq and spatial transcriptomic datasets and *in vivo* placental tissue specimens will be invaluable for informing marker selection and validating expression in the in vivo context. The ability to

observe, model, and manipulate pregnancy in non-human primate studies, both *in vitro* and *in vivo*, is a feature unavailable in human research and warrants comprehensive study of macaque trophoblast subpopulations. Overall, this work contributes to our understanding of macaque EVT expression profiles to improve the future interpretation of macaque studies and translation to human pregnancy.

Publication:

L.T. Keding, A.R. Heselton, E. Ren, S.A. Shaw, M.R. Koenig, T.G. Golos, J.K. Schmidt, In vitro differentiation of macaque extravillous trophoblasts in a low oxygen environment, Placenta 163 (2025) 16–28. https://doi.org/10.1016/j.placenta.2025.02.014.

CHAPTER 3

A NOVEL METHOD OF MACAQUE PLACENTAL PATHOLOGY ANALYSIS

Placental insufficiency pathologies associated with adverse pregnancy outcomes (APOs) are currently best defined through the maternal vascular malperfusion (MVM), fetal vascular malperfusion (FVM), and chronic inflammation pathological meta-categories outlined in the 2016 Amsterdam Consensus [15]. This consensus statement was established by a team of placental pathologists across the globe, providing standardized practices, terms, and thresholds to utilize while analyzing a placenta histologically. The guidelines first call for visual assessment of the placenta, to determine the of samples collected for microscopic examination dissection [15]. These samples are then assessed for MVM, FVM, and inflammatory pathologies, mainly categorized through visual estimations of histological lesion parenchymal coverage and severity by microscopy.

A limitation to current analysis techniques is that some placental pathologies cannot be appreciated by the naked eye, biasing placental sampling towards the inclusion of large, easily identifiable lesions. Additionally, as pathological diagnoses are made by visual estimates, inter- and intra-observer discrepancies are common when assessing placental pathology in cases of APO [116,117]. As nearly all placental pathologies are composed of a common set of pathological features [16,17,118], we propose that quantitative annotation of these well-established pathological features may be a beneficial method of assessing placental pathology in a research setting – especially when comparing placental pathology to all other forms of strictly

quantitative biological data prevalent in placental research. The authors of the Amsterdam consensus allude to this point - noting that better quantification of intravillous fibrin deposition would aid in elucidating its specific ties with vascular malperfusion [15].

This chapter outlines the novel methodology our group has developed with respect to placental pathology feature quantification and analysis. It is our position that moving towards a strictly quantitative assessment of histological slides is a prudent next step forward in placental pathology research. Our aim was to categorize and annotate common pathological features that would be easily identifiable by hematoxylin and eosin (H&E) stain, at 4x magnification. This magnification was chosen for its functionality and resolution. Less magnification (2x) results in images of which pathologies are hard to discern, whereas increased magnification (10x-40x) results in image sizes currently too large for efficient storage, sharing, and analysis. By design, we avoided annotating along classically defined placental pathological conditions guidelines, as they often contain overlapping morphological characteristics, such as coagulated blood, fibrin deposition, architectural breakdown of villi, leukocytic infiltrate, and mineralization [15,16,119]. In this way, sought to be as objective as possible - reducing the complexity of pixel annotations and limiting qualitative interpretation of pathologies being analyzed – moving towards a more quantitative, unbiased form of placental analysis.

MACAQUE PLACENTAL PATHOLOGICAL FEATURE ANALYSIS

All cotyledon sub-tissue and pathological feature annotation categories were conceptualized and developed by Logan T. Keding, with the help of veterinary pathologist Dr. Heather A. Simmons and board-certified placental pathologist Dr. Crystal Bockoven. Final cotyledon sub-tissue, intervillous space, and pathological feature annotation validation was accomplished through Dr. Bockoven's assessment of 10 randomly selected cotyledon images.

Placental cotyledon annotation methodology

Placental analysis was performed at the level of the cotyledon – as this is the smallest functional unit of blood exchange at the placenta. H&E-stained cotyledon center cut whole slide image (WSI) files were randomized using numeric identifiers – resulting in the annotator being blind to treatment, animal, or disc of which the cotyledon was derived. WSI files were annotated in GIMP (GNU Image Manipulation Program version 2.10.38), utilizing discrete layers for each sub-tissue or feature annotation. The pixel selection process was expedited through utilization of *Free Select*, *Select by Color*, and *Fuzzy Select* tools. Once annotations were finalized, the *Histogram* data tool was then used to quantity the number of pixels in each layer. Additional data collection involved quantifying pathological pixels isolated by individual sub-tissues. Of note, the Antialiasing tool option was deselected throughout all annotation processes. Antialiasing is a raster-based tool that alters the opacity of object borders, blending pixels with their surroundings. By deselecting

this feature, we ensured clean boundaries and non-overlapping annotations, allowing all annotations to be performed and reported to single-pixel resolution.

Cotyledon sub-tissue annotations

Individual sub-tissue layers that comprise the cotyledon were first annotated – the chorionic plate (CHR), placental villi (VIL), trophoblastic shell (TBS), and decidua basalis (DBS) regions (Figure 3.1A-C). All blood pixels along the periphery of the cotyledon were excluded from analysis (Figure 3.1A-B), as their origin was likely an artifact from the dissection process. Additionally, pixels constituting large areas of pooled blood within intact vascular channels were excluded from analysis.

DBS pixels were evidenced by location, change in cellular structure, frequency of nuclei, and increased hematoxylin staining compared to the TBS (Figure 3.1C). Due to the constant thinning of DBS tissue throughout gestation and incomplete removal at dissection, this sub-tissue was often sparse and, in some cases, completely missing from late gestation cotyledons. Blood pooled between DBS and TBS sub-tissue that met inclusion criteria were included in DBS pixels.

The TBS region (known as the cell column in humans) was lighter in hue, usually more eosinophilic, and contained sparse hematoxylin-stained nuclei (Figure 3.1C). Anchoring villous tissue continuous with the TBS were included in TBS area (no tissue breaks or staining color change). Where TBS and CHR sub-tissues met, distinctions were made by tissue structure and staining. Rarely, TBS-CHR distinctions were not evident. In these cases, the two sub-tissues were split at the

approximate half-way point between the most easily identifiable areas of CHR and TBS sub-tissues.

VIL pixels were evidenced by their location, sandwiched between TBS and CHR sub-tissues, along with their unique structure and staining (Figure 3.1C). The final sub-tissue category, CHR, was evidenced by location. Structure and staining from VIL sub-tissue (Figure 3.1C). Agglutinated villi continuous with CHR sub-tissue were included in CHR pixels. Large, continuous stem villi emerging from the CHR were separated from CHR pixels along the natural contour of the plate and included in VIL sub-tissue pixels. Together, these DBS, TBS, VIL, and CHR pixels constituted the total cotyledon area (COT).

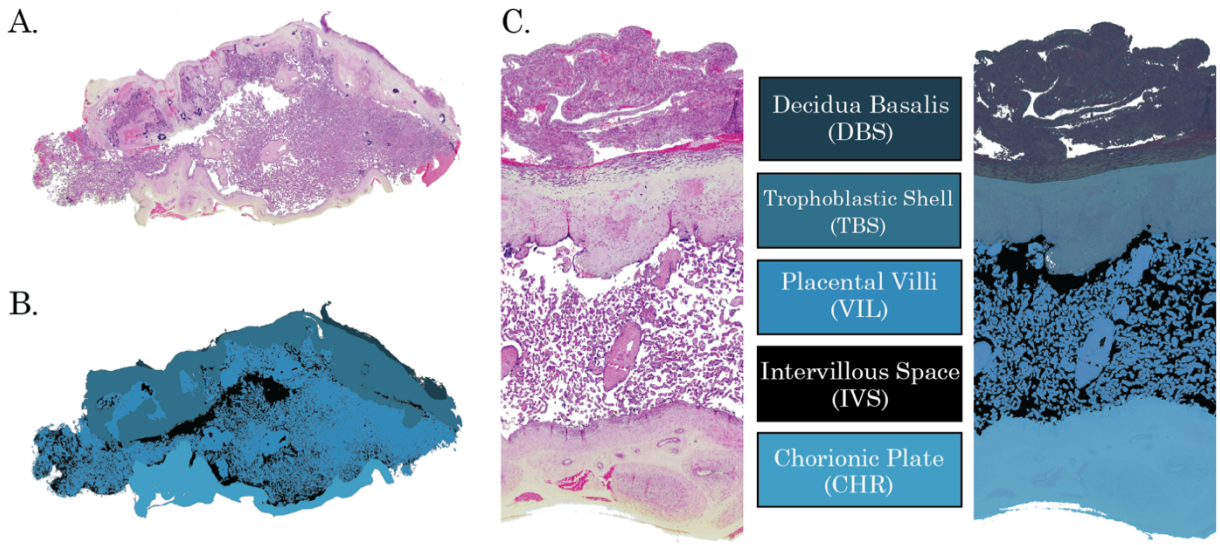

Figure 3.1. Representative cotyledon sub-tissue annotations. A) An H&E 4x magnification WSI of a placental cotyledon. B) Sub-tissue and intervillous space (IVS) annotations of the cotyledon above, with all peripheral red blood cells removed. C) An enlarged cotyledon section, highlighting decidua basalis (DBS), trophoblastic shell (TBS), placental villi (VIL), and chorionic plate (CHR) sub-tissue layers and the intervillous space (IVS).

In addition to COT pixels, the intervillous space (IVS) was also defined, separate from COT and sub-tissues. This included all negative space within the VIL

region and non-peripheral pooled blood pixels within the IVS (Figure 3.1). All COT sub-tissue and IVS annotations were non-overlapping, constituting discrete total pixel areas within digitized WSIs.

Pathological feature annotations

Next, pathological feature annotations were determined within the COT (DBS, TBS, VIL, and CHR) and IVS pixels (Figure 3.2A-C). As was the case with COT and IVS annotations, all pathological feature annotations were non-overlapping, to single pixel resolution. The sole pathological feature of the IVS was intervillous blood pooling (IVB) (Figure 3.2C). The remaining pathologies were found within COT pixels, and consisted of tissue hematoma (HEM), fibrin deposition (FBD), villous agglutination (AGL), inflammatory villous agglutination (INF), and stromal mineralization (MIN) (Figure 3.2C). All pathologies were deemed of sufficient size for annotation when ≥ ~2,000 px for feasibility. To capture total cotyledon pathology, these discrete COT pathological features were also combined for an additional pathological feature category: total pathological pixels (PTH). By design, these PTH pixels overlapped with all other COT pathological feature pixels.

Intervillous blood pooling (IVB)

Intervillous blood pooling (IVB) can take the form of several different types of classically defined pathology, depending on the time, location, and origin of the coagulation [17]. Generally termed intervillous thrombi, pathological blood pooling that is central/basal (near the trophoblastic shell) is typically deemed more

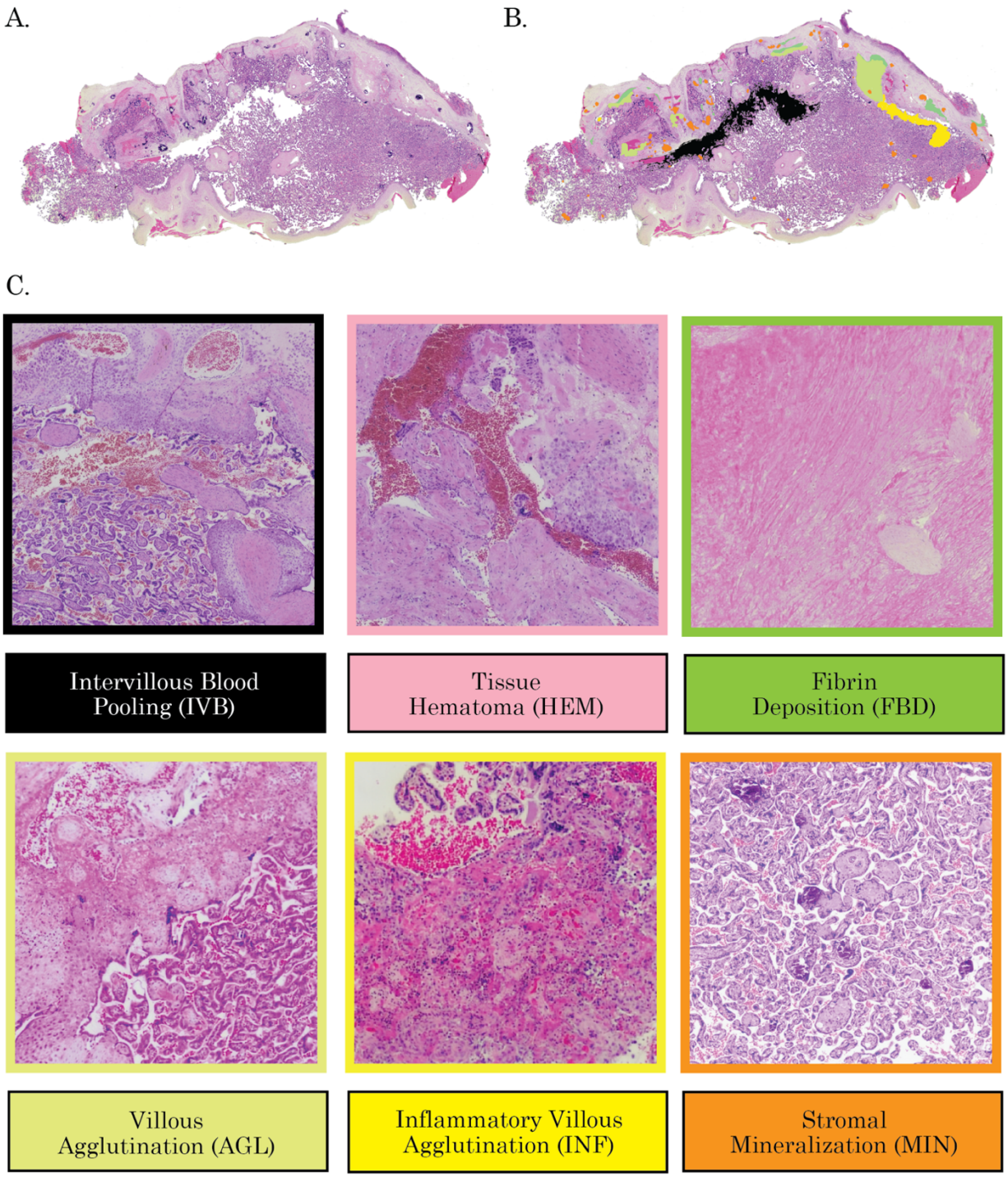

Figure 3.2. Representative cotyledon pathological feature annotations. A) An H&E 4x magnification WSI of a placental cotyledon. B) Color-coded pathological feature annotations overlaid. C) An enlarged representations intervillous blood pooling (IVB), tissue hematoma (HEM), fibrin deposition (FBD), villous agglutination (AGL), inflammatory villous agglutination (INF), and stromal mineralization (MIN).

pathological than blood pooling that occurs at the chorionic plate (subchorionic hematoma) [17]. This is largely based on the conceptual understanding that turbulent blood flowing from spiral arteries enters the IVS collides with the chorionic plate, leading to the villous displacement or reduced villous growth there [7]. With this understanding, we only included significant gaps/blood pooling of IVS pixels located along the TBS and/or centrally located within the VIL regions towards intervillous blood pooling (IVB) pixels (Figure 3.3). IVB encapsulated all blood in varying degrees of structure and coagulation, while excluding fibrin deposition.

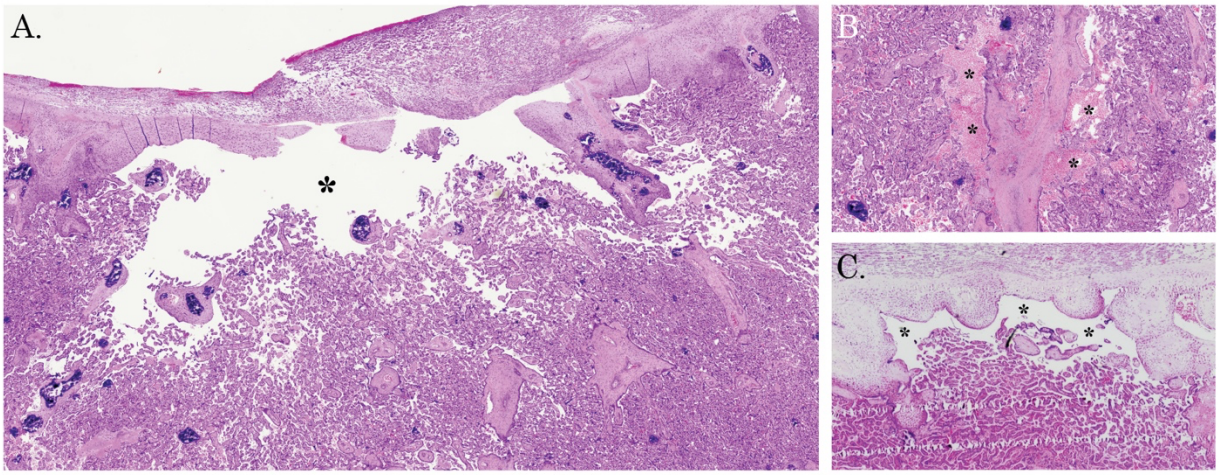

Figure 3.3. Representative images of cotyledon intervillous blood pooling. A) A large gap in the intervillous space along the trophoblastic shell, indicative of pathological blood pooling. B) Two areas of blood pooling in the central parenchyma, alongside a stem villus. C) A smaller gap in the intervillous space, along the trophoblastic shell. Asterisks "*" represent pathological areas of interest. All images taken at 4x magnification.

Tissue hematoma (HEM)

Pooled blood pixels within CHR, TBS, or DBS tissues, not confined to intact vessels were given the categorical descriptor of tissue hematoma (HEM) (Figure 3.4). This feature presented as pooled blood, of varying degrees of structure and hyalinization. All significant blood pooling within intact vessels of COT or IVS regions

was excluded from analysis. Additionally, some coagulated blood displayed varying degrees of fibrin formation – in these cases effort was made to distinguish annotations between non-fibrous blood pooling and fibrin deposition (Figure 3.4A). The "Lines of Zahn" pathology being one such case, associated with thrombi formed in faster blood flow [120] (Figure 3.4B). When coagulation complexity made distinction not feasible, areas estimated to be over 50% non-fibrous blood pooling were included in HEM pixels (Figure 3.4B). Areas below 50% non-fibrous blood pooling were excluded from HEM pixels.

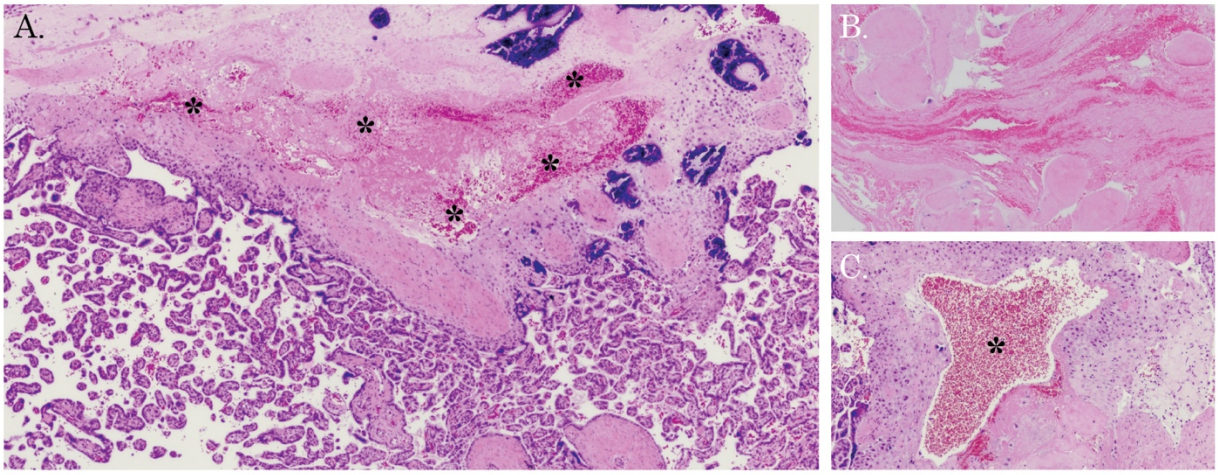

Figure 3.4. Representative images of cotyledon tissue hematoma (HEM). A) A partially coagulated area of pathological blood pooling within the trophoblastic shell alongside mineralization. B) Lines of Zahn pathology, diffusely intertwined fibrin deposition and structured blood. C) A mostly diffuse area of pathological blood within the chorionic plate. Asterisks "*" represent pathological areas of interest. All images taken at 4x magnification.

Fibrin deposition (FBD)

Placental fibrin deposition (FBD) has been shown to largely consist of fibrin, fibrinogen, and fibronectin [121]. Also termed fibrin, fibrinoid, or fibrinoid deposition, it is one of the most common and easily identifiable histological features of the placenta, presenting as amorphous, often anuclear, eosinophilic material (Figure 3.5).

Its appearance may vary widely, presenting as hyaline in nature, laminar, fibrous, reticular or any combination of each. Furthermore, this pathology can manifest in a spectral manner, ranging from a diffuse (Figure 3.5B), patchy appearance to complete parenchymal coverage (Figure 3.5A). A myriad of partially over-lapping pathological designations have been developed to better categorize fibrin deposition depending on the percent parenchymal coverage, villous agglutination or displacement, and location of blood proteins [17]. Fibrin within the villous region, for example, can be termed intra-, inter-, or perivillous – depending on its location with respect to villi [12]. Further, placental fibrin can be categorized as either fibrin-type, or matrix type, depending on whether it came from blood or cellular injury [12]. Additionally, large and homogenous fibrin deposits along the chorion (Langhans' fibrinoid) or trophoblastic shell (Nitabuch's fibrinoid) are considered normal features of a healthy placenta [12].

For the pathological feature of fibrin deposition (FBD) we included all eosinophilic material, either a nucleated (fibrin-type) or sparsely nucleated (matrix-type) (Figure 3.5). Additionally, FBD may have included some semi-coagulated blood, when constituting less than 50% of total area and thoroughly dispersed within FBD pixels (Figure 3.5C). Partially nucleated and/or anuclear homogenous fibrin that spanned the entire chorionic plate (Langhans' fibrinoid) or trophoblastic shell (Nitabuch's fibrinoid) was excluded from FBD categorization [12].

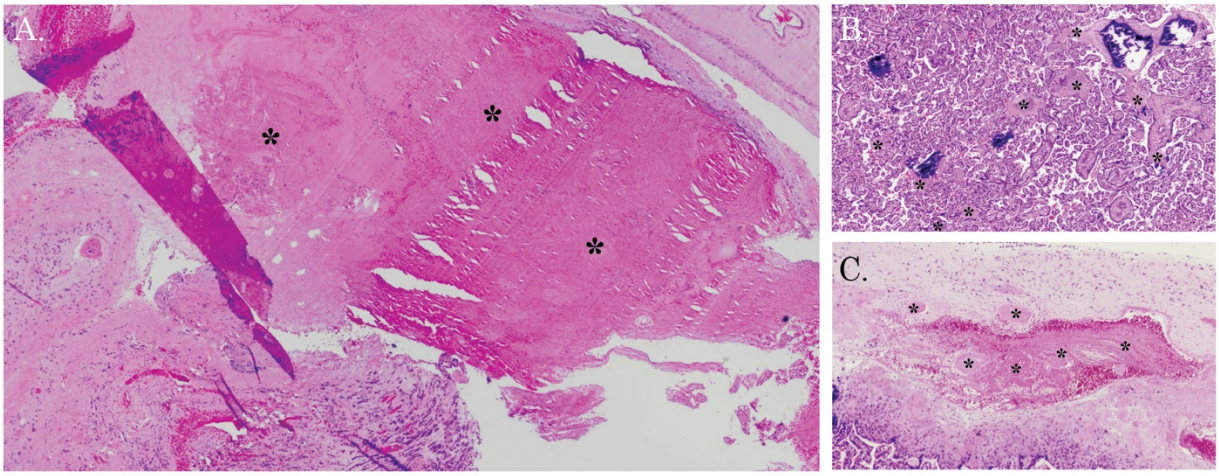

Figure 3.5. Representative images of fibrin deposition (FBD). A) A large area of most homogenous fibrin deposition along a placental septum. Gaps within FBD are an artifact of the tissue sectioning process. B) Diffuse, less eosinophilic FBD throughout the villous region. C) A pocket of partially coagulated blood within the trophoblastic shell, with FBD islands. Asterisks "*" represent pathological areas of interest. All images taken at 4x magnification.

Villous agglutination (AGL)

Within the placental parenchyma, all levels of villous branching may be subject to some level of agglutination. In a historical placental pathology context, agglutination refers to the clustering/crowding of villi – common in cases of accelerated villous maturation (AVM) or villitis of unknown etiology (VUE) [16]. Here, we defined architectural damage of the villi, with syncytial breakdown and inter/perivillous fibrin deposition as villous agglutination (AGL) (Figure 3.6). Perivillous fibrin deposition, massive perivillous fibrin deposition, and villous infarction are all overlapping, closely related pathological categories that have been associated with pathological outcomes for the fetus [17], that share the pathological attributes of villous agglutination as defined here. We created the AGL categorization as an attempt to neutrally describe this type of pathological presentation in tissue without speculation of the pathological origin inherent in other common categories.

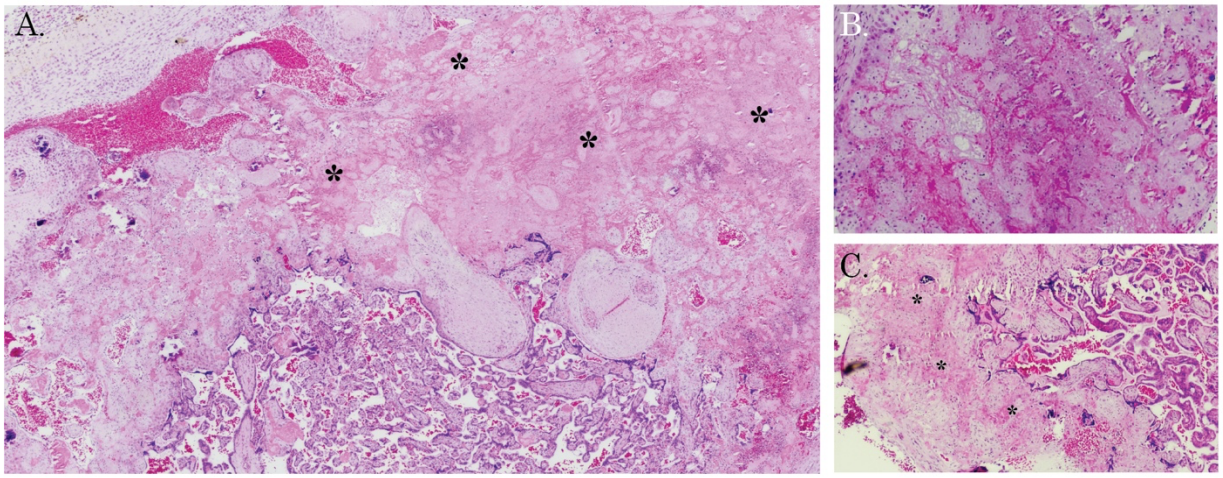

Figure 3.6. Representative images of villous agglutination (AGL). A) AGL along the trophoblastic shell, with small areas of heavy leukocytic infiltrate throughout. B) AGL found within the central parenchyma. C) AGL along the chorionic plate. Asterisks "*" represent pathological areas of interest. All images taken at 4x magnification.

Inflammatory villous agglutination (INF)

Chronic inflammatory placental lesions include chronic histiocytic intervillositis (CHIV), chronic villitis, and villitis of unknown etiology (VUE)[17]. Despite their discrete classifications, all conditions contain overlapping features of immune cell infiltration and villous destruction [17]. Furthermore, these lesions often manifest in tandem – supporting an argument for shared pathological origins of the lesions [118]. We established the category of inflammatory villous agglutination (INF), defined by a loss of villous structure, intervillous fibrin deposition, and heavy leukocyte infiltrate (Figure 3.7). This was established to encapsulate the villous damage and decreased syncytial surface area indicative of placental insufficiency, with the added element of an overt increase immune cell infiltrate. As a conservative measure, all cases of low or moderate leukocyte infiltrate were excluded, due to the potential inclusion of hematoxylin-stained nuclei at 4x magnification.

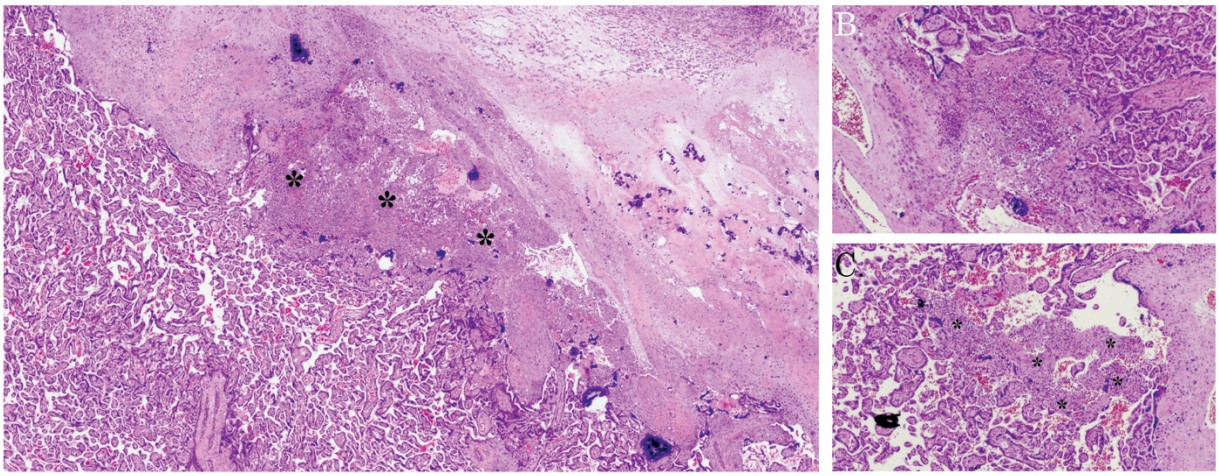

Figure 3.7. Representative images of inflammatory villous agglutination (INF). A) INF along the trophoblastic shell, with small areas of heavy leukocytic infiltrate throughout. B) INF found within the central parenchyma. C) INF along the chorionic plate. Asterisks "*" represent pathological areas of interest. All images taken at 4x magnification.

Stromal mineralization (MIN)

Placental mineralization is a histological feature most commonly associated with placental age [122]. Although this lesion has been found to present secondarily after an initial injury [19], it has not been historically deemed diagnostically or prognostically significant [19,123]. However, excessive focal mineralization in the placenta has been associated with fetal abnormalities, aneuploidies, disease, and demise [123]. Mineralization of the villous stroma seems to originate from fibrotic or necrotic tissue, indicating prolonged injury within these regions [19]. It has been hypothesized that stromal mineralization results from continued transport of minerals across the syncytia in the absence of fetal circulation and subsequent uptake [124]. Notably, a recent histological analysis of 1698 placentas associated segmented villous stromal mineralization with sclerotic/hypovascular chorionic villi, suggesting

this mineralization lesion as an independent pathological feature of vascular malperfusion within the fetal compartment [19].

Stromal mineralization (MIN) was identified by its location, often semi-circular appearance, and hematoxylin-rich staining (Figure 3.8). Mineralization was included only when found within the stroma of tissue, mostly likely the remnants of a vascular channel. Different manifestations of placental mineralization, such as syncytial knotting throughout villous regions and along the chorion or maternal floor [17], were excluded. This was due to their limited evidence of pathological effects on maternal and fetal outcomes, likelihood of false positives with H&E analysis [125], and poor feasibility of annotating this feature across all cotyledons.

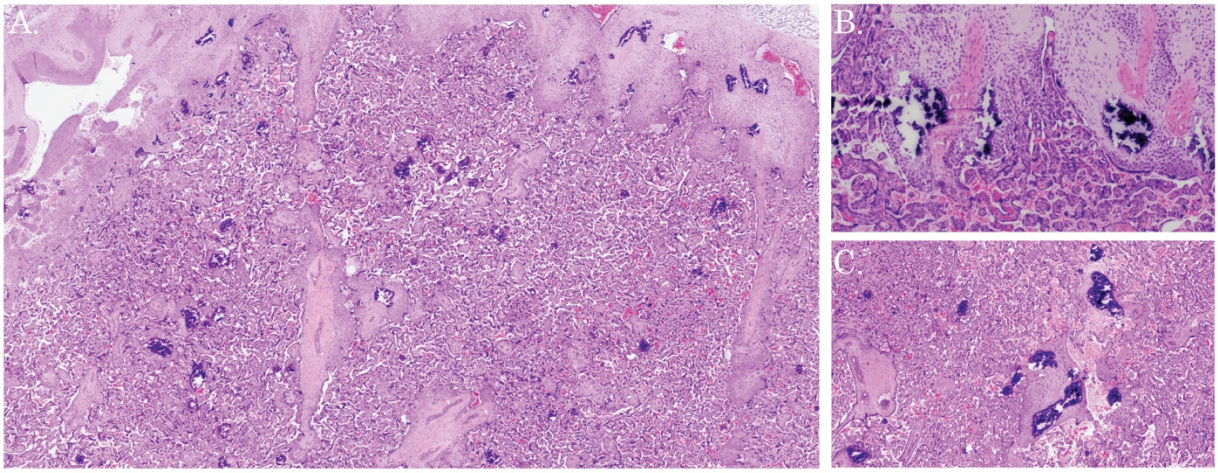

Figure 3.8. Representative images of stromal mineralization (MIN). A) MIN across the villous region and trophoblastic shell. B) MIN within the stroma of anchoring villi. C) MIN within stem and floating villi. All images taken at 4x magnification.

Quantification of placental pathological features

Currently, understanding of placental injury in the relies on the interpretation of descriptive pathological reports or a semi-quantitative scale-grading, all based upon visual estimations of lesion severity and coverage microscopically. The strength

of this new strictly quantitative methodology is the ability to determine exact quantity and location of pathological features (Figure 3.8), statistically analyze these features against other forms of quantitative biological data, and the removal of more qualitative aspects of historical placental pathological assessment. It is our position that pathological feature quantification may represent the big next step forward in placental pathology – working to shed the more qualitative and intuition-based aspects of placental pathology reporting.

Studies comparing WSI pathological analysis to traditional glass-slide analysis has found digital techniques to be non-inferior to classical microscopy [126]. The use of more objective and complete histological analyses have historically been hindered by cost and technological limitations [127]. However, with ever-increasing accessibility to low-cost/high-performance computing, the barriers to a thorough placental analysis have never been lower. Through quantification of pathological features, we may work towards decreasing intra/inter-observer bias while also generating more easily interpretable data for placental/pregnancy research.

As was accomplished with the Amsterdam Consensus nearly ten years ago [15], we envision that collaborative efforts would greatly strengthen the possible scope and accuracy of placental pathological feature annotation. As these pathological annotations are digitized, they are available for review, critique, and importantly, revision. It is our position that quantification of these pathological features will help to make placental pathology data more accessible to researchers for analysis, uncovering relationships within reproductive research previously unappreciated.

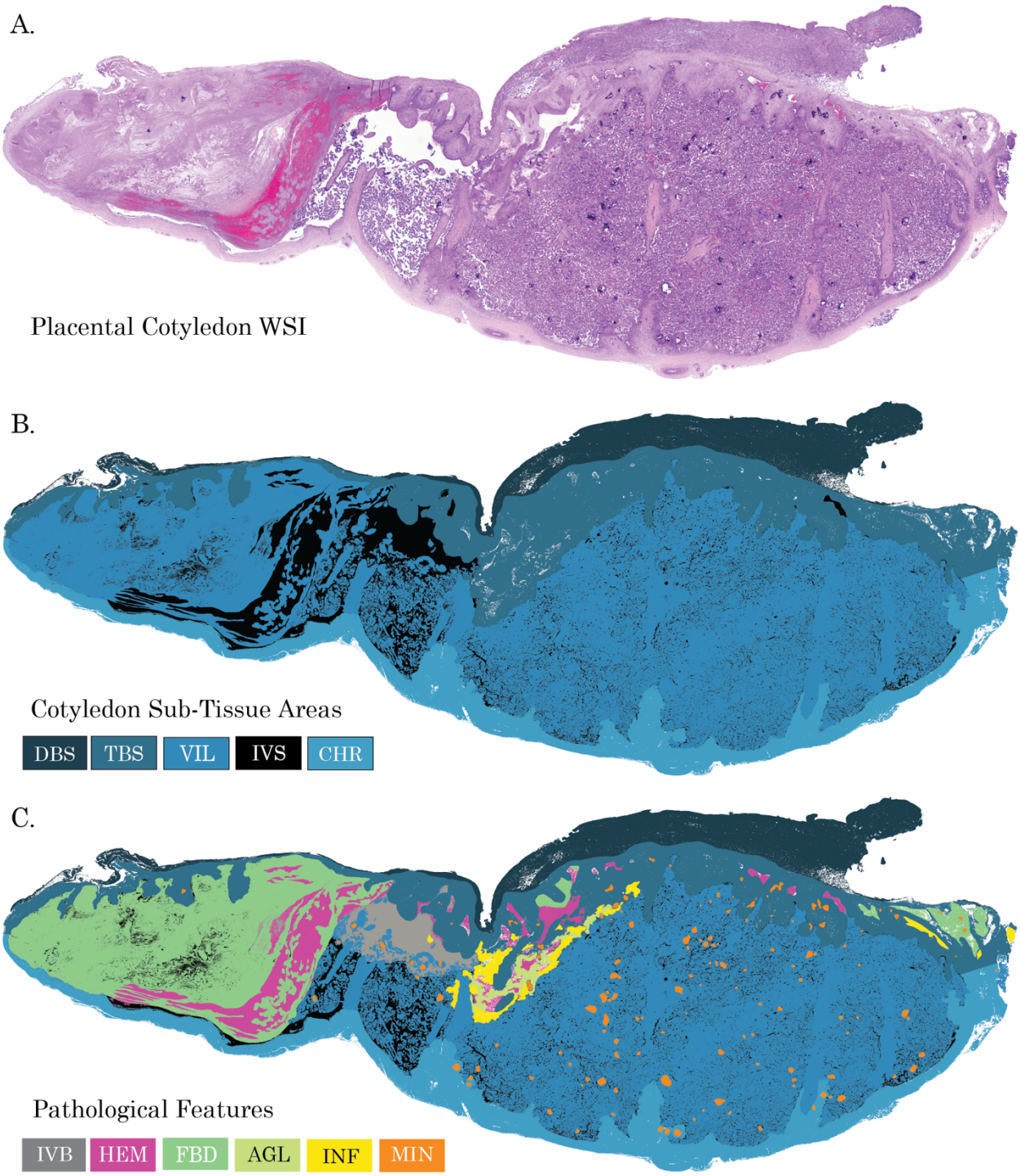

Figure 3.8. Representative images of stages of complete placental annotation. A) Whole slide image (WSI) of an H&E-stained placental cotyledon scanned at 4x magnification. B) Chorionic plate (CHR), placental villi (VIL), trophoblastic shell (TBS), decidua basalis (DBS), and intervillous space (IVS) sub-tissue areas annotated. C) Intervillous blood pooling (IVB), tissue hematoma (HEM), fibrin deposition (FBD), villous agglutination (AGL), inflammatory villous agglutination (INF) and stromal mineralization (MIN) pathological features annotated above sub-tissues.

CHAPTER 4

HEALTHY MACAQUE COTYLEDON PATHOLOGY AND PERFUSION

A majority adverse pregnancy outcomes (APOs) are attributed to pathologies of placental insufficiency, as evidenced by placental pathological analysis *ex vivo* [11]. A significant impediment to our collective understanding of placental insufficiency and its pathogeneses, however, is our failure to define what types of injury and quantities occur at the placenta in healthy pregnancy [17]. Chronic inflammatory pathologies, fetal vascular malperfusion [FVM] pathologies, and maternal vascular malperfusion [MVM] pathologies [15,16] all contribute to placental insufficiency [11], and are often found in varying degrees within healthy/normal placentae [122,128]. This is not surprising, as placental establishment, growth, and decay occurs much faster than in other tissues, resulting in nearly all placentae showing some degree of pathology at term [128]. To make matters more complicated, APOs can occur when the placenta exhibits no pathological lesions at all, when assessed by traditional analysis techniques [127]. Furthermore, despite the strong associations proposed connecting placental insufficiency pathologies with altered placental blood perfusion [17], little work has been done to directly connect *in vivo* maternal blood flow with placental pathology *ex vivo* [39].

Quantification of maternal blood perfusion at the placenta

In recent years, our group has developed robust methodology to quantify the maternal contribution to placental blood perfusion, using dynamic contrast enhanced (DCE) magnetic resonance imaging (MRI) [39,129,130]. These maternal blood

quantification methods, paired with placental assessment using established pathological analysis guidelines [15], has resulted in our group describing pathology and perfusion relationships at level of the whole placenta [39], however, these relationships largely broke down at the cotyledon-level of analysis [39]. Considering this, we aimed to expand our previous work on rhesus macaque placentae analysis at the cotyledon-level by exploring the relationships between fetoplacental biometrics and maternal blood perfusion in relation to placental injury. This was accomplished through implementation of our novel pathological feature quantification methodology outlined in chapter three.

Connecting pathology to biometrics and blood perfusion at the cotyledon level

We utilized healthy/normal macaque pregnancies to investigate the strength and direction of biometric-perfusion-pathology data correlations. As this study outlines normative data of primate pregnancy, our investigation was both hypothesis-driven and exploratory – working to enhance our understanding of the relationships fundamental to normal/healthy pregnancy. Due to the great co-expression/overlap observed in these pathological features across the human placental literature [118,119], we hypothesized that pathological feature quantification would reveal significant positive relationships between each of the pathological features in healthy/normal placentae. Additionally, we hypothesized that pathological feature quantification would reveal an inverse relationship between placental pathology vs fetal weight and maternal blood flow at the cotyledon level in healthy/normal pregnancy, previously not recognized at the cotyledon level.

METHODS

Ethical use, care, and breeding of macaques

We utilized the macaque as our pregnancy model, due to its phylogenetic proximity, long gestational period, and placental physiology similarity to humans [10,34]. All experimental procedures and tissue collections were performed in accordance with the NIH Guide for the Care and Use of Laboratory Animals and under the approval of the University of Wisconsin College of Letters and Sciences and Vice Chancellor Office for Research and Graduate Education Institutional Animal Care and Use Committee, protocol G006209. Wisconsin National Primate Research Center (WNPRC) macaques were housed with compatible mates and monitored for breeding and menstruation. Date of conception was estimated based on initiation of the menstrual cycle, observation of copulation with presence of ejaculate, and ultrasound measurements of fetus and gestational sac.

Saline-injected rhesus macaques

The biometrics, placental tissue, and MRI data used here were originally collected from 7 saline-treated pregnant rhesus macaque dams at the Wisconsin National Primate Research Center of prior study [39,130]. Three of the seven animals were injected with 1 mL of sterile saline into the amniotic sac at gestational day (GD) ~55 [39], while the remaining four animals received a 5 mL sterile saline injection to the anterior disc at GD ~100. Both groups received mid-gestation (GD ~95) and late-gestation (GD ~145) MRIs with ferumoxytol contrast agent, to track maternal blood perfusion at the placenta. Although the source animals' tissue and DCE-MRI raw

files of which this data was derived are the same, all data and analyses presented in this work are original, unpublished in any form.

MRI acquisition, processing, and maternal blood metrics

Pregnant rhesus macaques received monitoring by ferumoxytol dynamic contrast enhanced (DCE) MRI to assess changes in maternal blood dynamics at the placenta across gestation. Ferumoxytol, a superparamagnetic iron oxide nanoparticle approved for clinical treatment of anemia, was chosen due to its established safety [129], efficacy [39,131], and inability to cross into fetal tissue. Dams were imaged under anesthesia in right-lateral position on a 3.0-T clinical scanner (GE Healthcare) at GD ~95 and ~145. DCE MRI data was acquired following venous injection of ferumoxytol (Feraheme, 4 mg/kg, diluted 5:1 with saline) with a respiratory-gated, T1-weighted spoiled gradient echo sequence (DISCO, TR = 4.8 msec, TE = 1.8 msec, temporal resolution = 4.5-7.7 s, spatial resolution = 0.86x0.86x1.00 mm3, # of time frames=40). Ferumoxytol, and a subsequent flush with 20 mL of saline, was administered at 0.5 mL/second with a power injector and started simultaneously with the scan. Placental segmentations were conducted semi-automatically with ITK-SNAP [132] based on final-timepoint DCE images. DCE-MRI data were processed using an established workflow [39] to obtain measures of maternal blood volume (VOL), flow (FLO) for each perfusion domain. Fill time (FIL) for each perfusion domain was produced by dividing cotyledon volume (mL) by blood flow (mL/min). Perfusion (PER) metrics were produced by dividing blood flow (mL/min) by cotyledon volume (mL) for each perfusion domain.

Fetal and placental tissue dissection

All pregnant macaques underwent cesarean section to excise placental and fetal tissue at GD ~155, 10-14 days prior to full gestation [133], to avoid potential early labor and loss of tissue. Placental and fetal tissue weight were noted, along with the maximum placental disc diameter. Intact placentae were then photographed, to be used alongside the maximum diameter measurement to determine placental attachment areas via ImageJ (Version 1.54). Placentae were then moved to a BSC for dissection. Six of the seven fetuses had bidiscoid placentae, consisting of primary (D1) and secondary (D2) discs. One PL-I animal (Animal 7) possessed only a primary disc, resulting in a cohort monodiscoid rate of 14%, in agreement with previously described naturally-occurring rates between 5 and 20% [35,122,134]. Placental cotyledons were determined first, through both visual and textural assessment. A second photograph was taken of each placental disc, layered with individual cotyledons annotations for sampling reference. Individual cotyledons were dissected from one another, along the placental septa separating cotyledons (primary disc n =50, secondary disc n=30). Once isolated, a full thickness section from each was obtained, aiming for central mass while avoiding edge/peripheral tissue.

Cotyledon center cuts were fixed in 4% paraformaldehyde, embedded in paraffin wax, and sectioned at 5 μm – as described previously [39]. Sections were then stained with hematoxylin and eosin (H&E), cover-slipped, and scanned for whole slide images (WSIs). WSIs were stitched together at 4x magnification using a Nikon Eclipse Ti2 microscope with NIS-Elements AR software (v 5.02.006, Nikon

Instruments Inc., Melville, NY, USA). This magnification was chosen for its functional feasibility – 4x images allowed sufficient resolution to identify pathologies while keeping WSI file sizes manageable for image sharing, processing, and storage.

Cotyledon matching to perfusion domains

Previous work from our group [39] and others [135] have demonstrated that cotyledons of primate placenta can share a single perfusion domain, supplied by a single, or multiple maternal spiral arteries. For the present study, we took a conservative approach, excluding any perfusion domains that spanned multiple physical cotyledons. In this fashion, we have selected for perfusion domain-cotyledon pairings of which we are confident of the local MRI-derived maternal blood metrics. Additionally, the matching of perfusion domains and physical cotyledons relies heavily on a degree of asymmetry in both MRI scans and physical cotyledon orientation. When a near perfectly circular placenta displays a near symmetric layout of cotyledons, there is little evidence that can definitively prove that virtual perfusion domains and physical cotyledons are matched appropriately (Figure 4.1). These cases were omitted from perfusion domain-cotyledon matched analyses.

Placental annotation data preparation

All placental cotyledons were analyzed using the tissue area annotations (chorionic plate [CHR], placental villi [VIL], trophoblastic shell [TBS], decidua basalis [DBS], and intervillous space [IVS]) and pathological feature annotations (intervillous blood pooling [IVB], tissue hematoma [HEM], fibrin deposition [FBD], villous agglutination [AGL], inflammatory villous agglutination [INF], and stromal

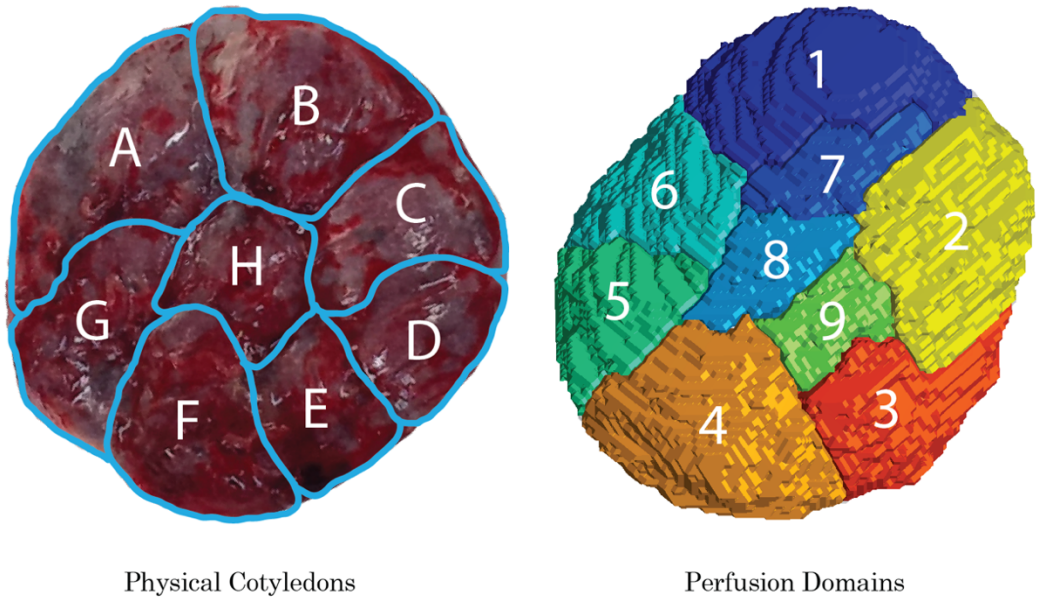

Figure 4.1. Example of omitted cotyledon-perfusion domain data. Left) An image of a placental disc (decidua side up) with cotyledon borders (blue) and labels (A-H). Right) A 2-dimenstional image of a 3-dimensional image file, with perfusion domains labeled 1-9. Both the circularity and uniformity of cotyledon/perfusion domain borders result in uncertain matching.

mineralization [MIN]) outlined in Chapter 3 (Figures 3.1, 3.2, and 3.9). Annotations were reported as a ratio of the area of which they were located in. All sub-tissue areas (DBS, TBS, VIL, and CHR) were reported as a ratio with respect to their specific COT pixels (i.e. CHR pixels/COT pixels). Pathological feature pixels (HEM, FBD, AGL, INF, MIN, and PTH) were handled the same - always reporting the raw pixel count of a placental feature with respect to the tissue or sub-tissue it was located within (i.e. CHR MIN pixels/CHR pixels, COT INF pixels/COT pixels). By analyzing sub-tissue and pathological feature areas as a ratio, we able to more accurately compare pathologies and sub-tissues across varying-sized cotyledons. Additionally, we reported IVS pixels with respect to VIL pixels (i.e. IVS pixels/VIL pixels). In this way, we accounted cases of a large proportional IVS regions contained within small

cotyledons, and vice versa. Like in the cases of COT pathological features, the IVB feature within IVS pixels was reported as a ratio (i.e. IVB pixels/IVS pixels).

Additionally, we omitted all decidua basalis annotation data from the correlation analysis section of our study. Decidual tissue does not grow with the rest of placental tissue throughout gestation. As a result, decidual tissue at term is often quite sparse, with smaller discs containing more decidual tissue for analysis than larger discs. We believe this would have contributed to more pathology being observed as a function of increased analyzable area in smaller placentae, skewing our data and interpretations.

Statistical analyses

All statistical analyses were accomplished in Graphpad Prism (version 10.4.1) at a significance threshold of $\alpha=0.05$. T tests were used to assess differences in animal biometrics and placental maternal blood metrics across saline treatments. COT, IVS, and sub-tissue pixel areas across animals were assessed by either t test or Mann-Whitney U test, depending on the normality of data being analyzed. To assess correlative relationships at animal, disc, cotyledon, and sub-tissue level, we utilized the non-parametric Spearman correlation test. This test was chosen as a conservative approach towards an exploratory dive into novel data. The observed correlations inform us whether these factors demonstrate a monotonic (one-way movement [up or down]) relationship, while allowing for non-normality in our data distribution, as well as zero-inflation – a quality inherent in many of the pathological features investigated.

RESULTS

Saline injection route did not affect biometrics or maternal blood perfusion

Our central aim was to assess biometric-pathology-perfusion relationships in healthy/normal rhesus macaque pregnancy. Accordingly, we first determined whether we could condense the placenta-injected (PL-I) and amnion-injected (AM-I) animal data into a single healthy/normal dataset. To this end, we assessed maternal, placental, and fetal biometrics, as well as maternal blood perfusion at the placenta across PL-I and AM-I groups to determine if injection route/timing had affected any available health metrics. At c-section, veterinarian and pathologist assessment of dam and fetus described healthy/normal findings, with histological analysis further demonstrating no significant lesions across fetal organs of both groups. Visual assessment of placental discs showed good circularity and primary discs displayed central/eccentric cord insertions across all animals. Analysis of fetal, placental, and maternal biometrics demonstrated no significant differences across the two treatment groups (Figure 4.2A). When stratifying biometrics by disc, we also observed no differences in PL-I and AM-I placentae (Figure 4.2B). Furthermore, all individual datapoints were within 2 standard deviations of gestational age-matched weights and disc measurements previously reported in healthy/normal macaques [35].

Next, cotyledon volume, blood flow, blood fill, and blood perfusion metrics were assessed at the placenta during mid- and late-gestation in placenta-injected (PL-I) and amnion-injected (AM-I) animals to determine whether injection route led to significant alterations in these maternal blood metrics (Figure 4.3). As expected,

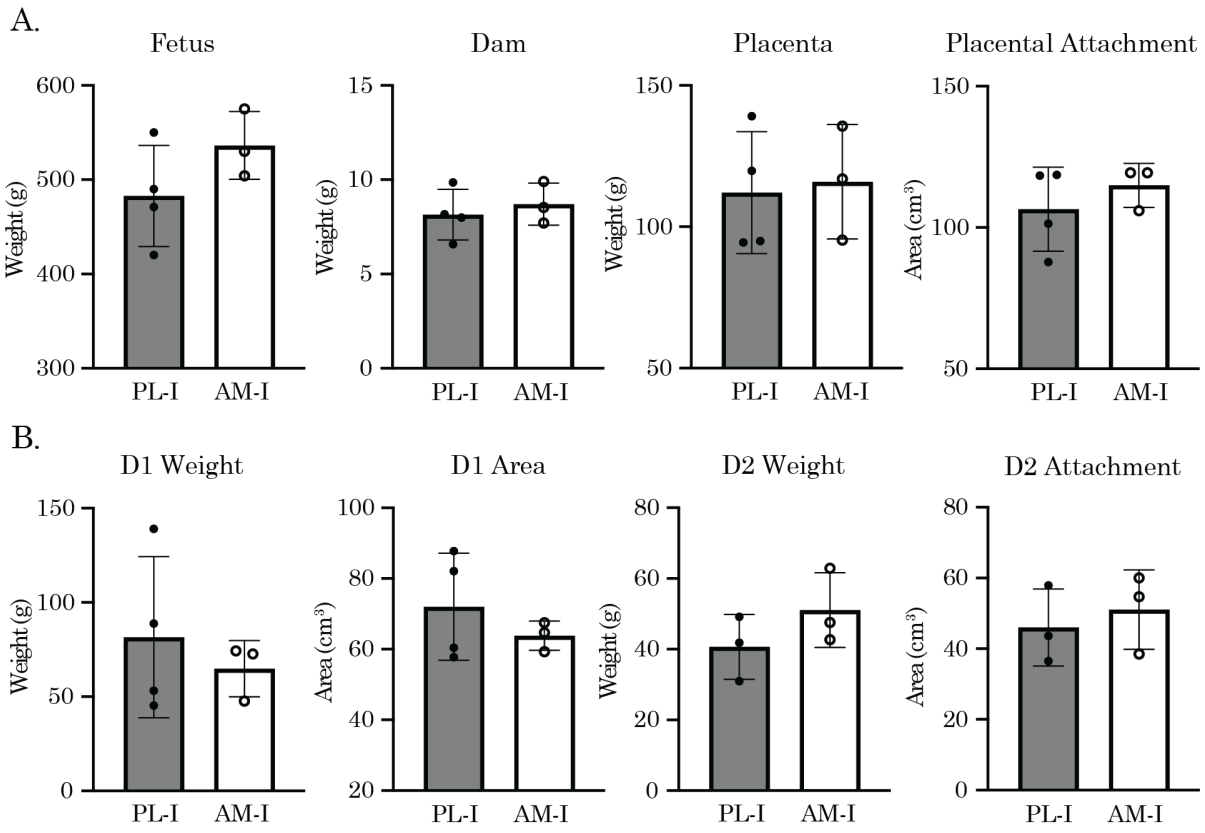

Figure 4.2. Fetal, placental, and maternal biometrics of saline-injected animals. A) Gross weights of the fetus, dam, and placental discs, along with placental disc attachment areas from placenta-injected (PL-I, black) and amnion-injected (AM-I, white) animals. B) Placental biometrics stratified by primary (D1) and secondary (D2) discs. Data points represent individual animal values; bars represent the mean +/- the standard deviation.

cotyledon volume, blood flow, and blood fill-time at the placenta all increased from mid- to late-gestation (Figure 4.3A), showing no difference between treatments when comparing the change in these metrics across gestation. Together, all available evidence suggests no difference between PL-I and AM-I treated pregnancies. When also considering the well-established negligible effect of saline injection on mammalian biology, we deemed it appropriate to consolidate these data into a single group representing healthy/normal rhesus macaque pregnancy.

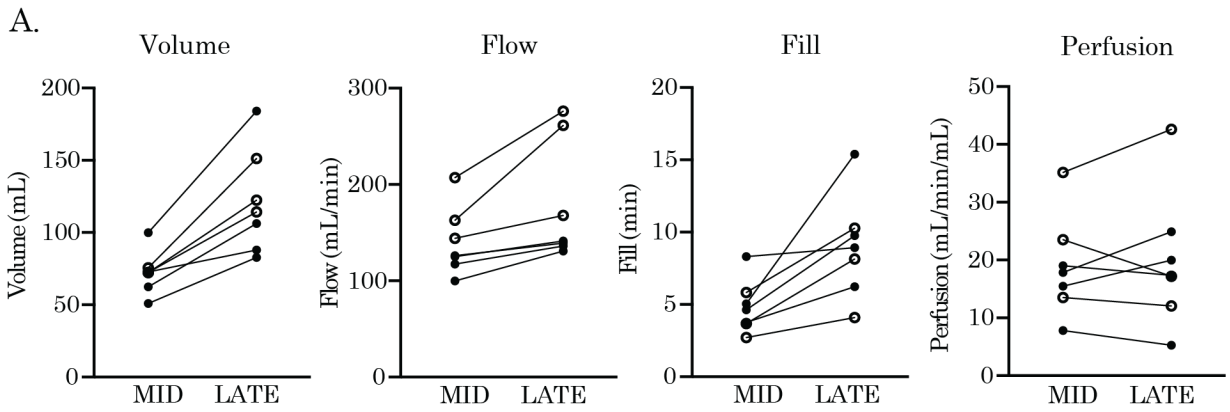

Figure 4.3. Maternal blood metrics at the placenta. A) Maternal blood volume, flow, fill, and perfusion at the placenta in placenta-injected (PL-I, black) and amnion-injected (AM-I, white) animals across late gestation.

Macaques and humans share similar placental sub-tissue and pathological features

To first investigate how macaque and human placentae compare, we began our analysis by categorizing contribution of sub-tissues and IVS to total cotyledon area, and the contribution of individual pathological features to total cotyledon pathology (Supplemental Figure 4.1). Unsuprisingly, the placental villous region (VIL) constituted the greatest proportion of cotyledon pixels, while the decidua basalis (DBS) made up the least (Supplemental Figure 4.1A), as is observed in human placentae [12]. Total cotyledon sub-tissue (COT) pixels by animal revealed that cotyledon sample sizes differed across animals (Supplemental Figure 4.1B), confirming our decision to report all pathological analyses in ratio values instead of pixels. Additionally, analysis of cotyledon sub-tissue and IVS pixel ratios across animals revealed several significant animal-specific differences (Supplemental Figure 4.1B). Significant differences in cotyledon pathological feature manifestation were also observed across animals (Supplemental Figure 4.1D), demonstrating that

pathological lesion variability is observed across healthy/normal placentae in humans [17] and macaques.

Pathological feature data across animals were further organized to illustrate percent contribution of each sub-tissue to individual and combined cotyledon pathology (Supplemental Figure 4.2). Fibrin deposition is implicated in nearly every placental lesion to some degree [16] and can be the result of both blood coagulation and cell death [12], and is therefore likely the single most common feature connecting all placental pathologies. Additionally, diminished blood flow near the basal plate [7] is hypothesized to result in increased fibrin deposition near the trophoblastic shell (Rohr's fibrinoid) [17] as well as a general increase placental pathology there [17,119]. In agreement, fibrin deposition constituted the greatest proportion of pixels across all pathological features, while the TBS sub-tissue (the basal plate) contained the greatest proportion of total pathological pixels (Supplemental 4.2).

Placental pathology is associated with decreased fetal weight in healthy pregnancy

We next focused on relationships between healthy/normal pregnancy metrics, using Spearman correlations to determine the direction, strength, and significance of associations. All biometric, pathology, and perfusion relationships were visualized by heatmap to show the direction and strength of individual correlations, as well as better illustrate general trends within and across categories. We chose this method of extensive analysis and review in order to capture pertinent positive and negative associations, crucial to a wholistic understanding healthy/normal primate pregnancy. We began by investigating maternal, fetal, and placental biometrics vs placental

pathological features (Figure 4.4). Our hypothesis was that increased pathology would be associated with altered placental size, decreased fetal weight, and increased maternal weight.

We observed that the pathological feature intervillous blood pooling (IVB) was associated with decreased placental weight, while mineralization (MIN) was positively associated with placental attachment area across discs at the cotyledon level (Figure 4.4). IVB, is often considered maternal vascular malperfusion pathology [17], and is generally associated with smaller placentae [136]. Increased placental attachment [137,138] and increased placental mineralization [41] have been associated with increased placental compensation in pregnancy. Increased cotyledon mineralization across both discs also demonstrated a negative relationship with fetal weight, while mineralization and multiple other pathologies demonstrated a positive relationship with maternal weight (Figure 4.4). As pathological manifestation and fetal/maternal weight relationships have historically only been reported significant in association with disease states [11,139], these data suggest that significant relationships between pathology and maternal/fetal weight can be observed in healthy/normal pregnancy as well.

IVB, inflammatory villous agglutination (INF), and MIN pathologies demonstrated a negative relationship with primary disc weight (Figure 4.4). Significant relationships within the secondary disc involved villous agglutination and INF demonstrating a negative relationship with secondary disc size, and IVB and MIN demonstrating a positive one (Figure 4.4). Interestingly, increased pathology in

the primary disc was significantly associated with increased secondary disc size (Figure 4.4), suggesting potential compensatory growth in the secondary disc. Further, mineralization (an FVM pathology [19]) and IVB (an MVM pathology [17]) proved to be the only pathologies to demonstrate a negative relationship with fetal weight (Figure 4.4).

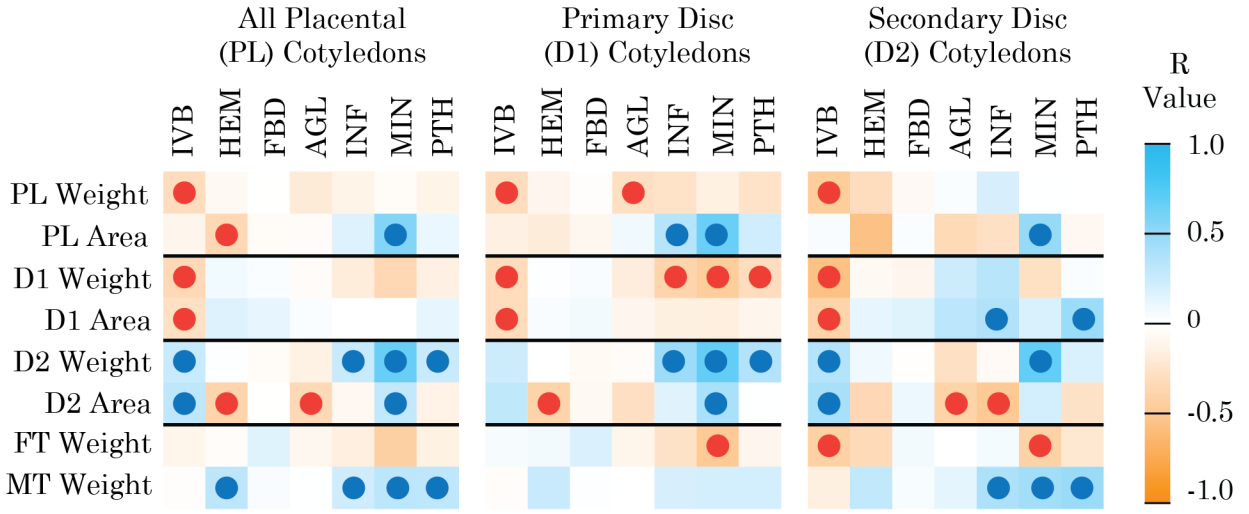

Figure 4.4. A heatmap showing correlations between fetal (FT), placental (PL, D1, D2), and maternal (MT) biometrics vs cotyledon pathological features and combined pathological features (PTH). Box color indicates relationship strength and direction. Blue boxes indicate a positive relationship (r value approaching 1, right). Orange boxes indicate inverse relationship (r values approaching -1, right). Dots within boxes indicate statistically significant relationships (α=0.05).

When next assessed fetal, maternal, and placental biometrics vs maternal blood perfusion metrics (Supplemental Figure 4.3) to determine if pregnancy biometrics were associated with altered maternal blood delivery in healthy/normal pregnancy. Cotyledon volume and blood flow were positively associated with total placental, primary disc, and fetal weights (Supplemental Figure 4.3), well in agreement with previous placental-wide association literature [140]. When further segregated by disc, however, discrepancies between primary and secondary disc were

noted. Primarily, primary discs displayed expected relationships with biometrics, such as increased cotyledon volume, blood flow, and fill time with increasing disc size, and decreased tissue perfusion with increased disc size (Supplemental Figure 4.3). Curiously, the secondary disc cotyledons lacked these common associations between disc biometrics and blood metrics, showing no relationship with secondary disc size and cotyledon volume or blood flow (Supplemental Figure 4.3). These data indicate differences in compensatory growth, potentially in the form of non-branching angiogenesis [141], which would likely result in increased placental weight alongside low cotyledon volume and blood flow.

Biometric-pathology relationships show discrepancies by disc

We next increased investigation resolution of biometric-pathological relationships to the cotyledon sub-tissue level, to determine whether pathological features located in specific areas of the cotyledon demonstrated increased contribution to observed relationships (Figure 4.5). MIN across all sub-tissues was negatively associated with fetal weight, while several pathologies across sub-tissues were positively associated with maternal weight (Figure 4.5). The only chorionic pathology related to total placental size was mineralization, demonstrating a positive association (Figure 4.5). Curiously, primary and secondary discs demonstrated opposite relationships at the chorion, as chorionic pathology was positively associated with primary disc size, and negatively associated with secondary disc size (Figure 4.5). The pathological features most significant in these relationships where tissue hematoma (HEM), fibrin deposition (FBD), and villous agglutination (AGL) – all

pathologies closely associated with blood coagulation. Although increased blood flow is associated with larger placentae and better pregnancy outcomes [140], turbulent blood ejected from spiral arteries colliding with the chorionic plate is hypothesized to induce stress and damage there [7], resulting in a potential increase in chorionic pathology with elevated cotyledon blood flow. The difference between primary and secondary discs observed in the blood flow-disc size relationship supports this interpretation (Supplemental Figure 4.3), as it mirrors the discrepancy at the chorionic plate (Figure 4.5). Curiously, the placental villous region pathological features demonstrated mixed associations, showing generally negative associations with primary disc biometrics, and generally positive associations with secondary disc biometrics (Figure 4.5).

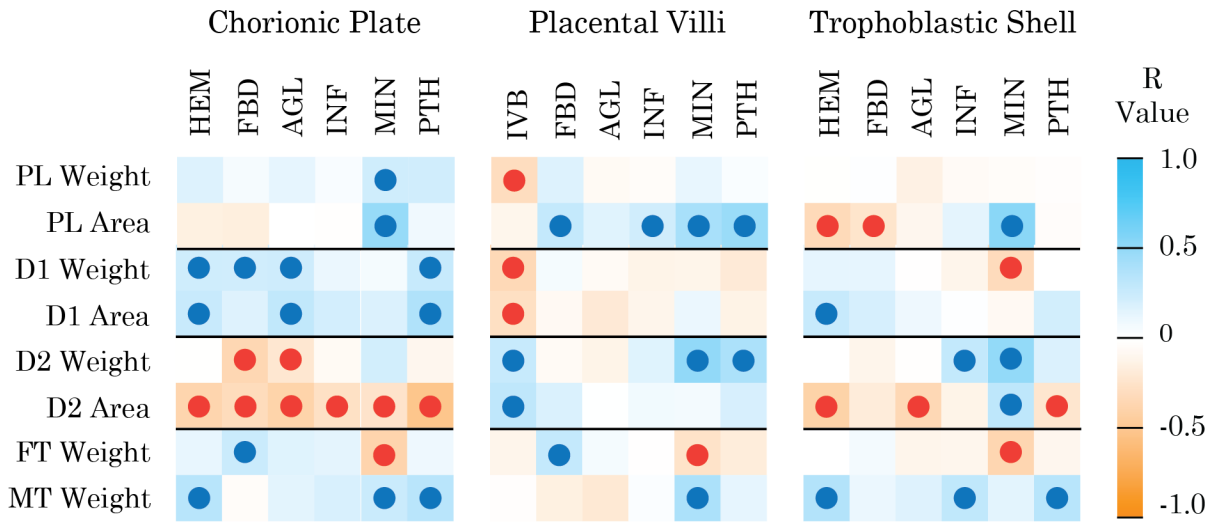

Figure 4.5. A heatmap showing correlations of fetal (FT), placental (PL, D1, D2), and maternal (MT) biometrics vs chorionic plate, placental villi, and trophoblastic shell cotyledon sub-tissue pathological features and total pathology (PTH). Box color indicates relationship strength and direction. Blue boxes indicate a positive relationship (r value approaching 1, right). Orange boxes indicate inverse relationship (r values approaching -1, right). Dots within boxes indicate statistically significant relationships (α=0.05).

Segregation primary and secondary cotyledon sub-tissue data helped to make sense of this lack of significant biometric-pathology relationships observed within the villous region (Figure 4.6). As expected, villous pathology of the primary disc demonstrated negative associations with primary disc placental biometrics and fetal weight (Figure 4.6A), as the villous region represents the interface of nutrient and oxygen exchange for the fetus and is crucial for healthy development [17]. In accordance with observations at the cotyledon level (Figure 4.4), pathology of the villous region in the primary disc as positively correlated with secondary disc biometrics – primary discs with increased villous region pathology were associated with larger secondary discs (Figure 4.6A). This trend was not observed when solely assessing the secondary disc sub-tissues (Figure 4.6B). At the chorionic plate, both primary and secondary disc chorionic pathologies reflected the same trends observed when discs were combined – a positive association between chorionic pathology and primary disc weight and a negative association between chorionic pathology and secondary disc weight (Figure 4.5 and 4.6A and B). Although many individual relationships proved significant, as in the combined sub-tissue analysis (Figure 4.5), limited general trends were noted in trophoblastic shell when segregated by disc (Figure 4.6A and B).

Pathological features demonstrate significant co-expression

High co-expression of distinct pathologies at the placenta is a well-documented phenomena [17,119,142]. However, less is known about the rates of pathology co-expression for lesions determined to be below the clinical threshold of significance.

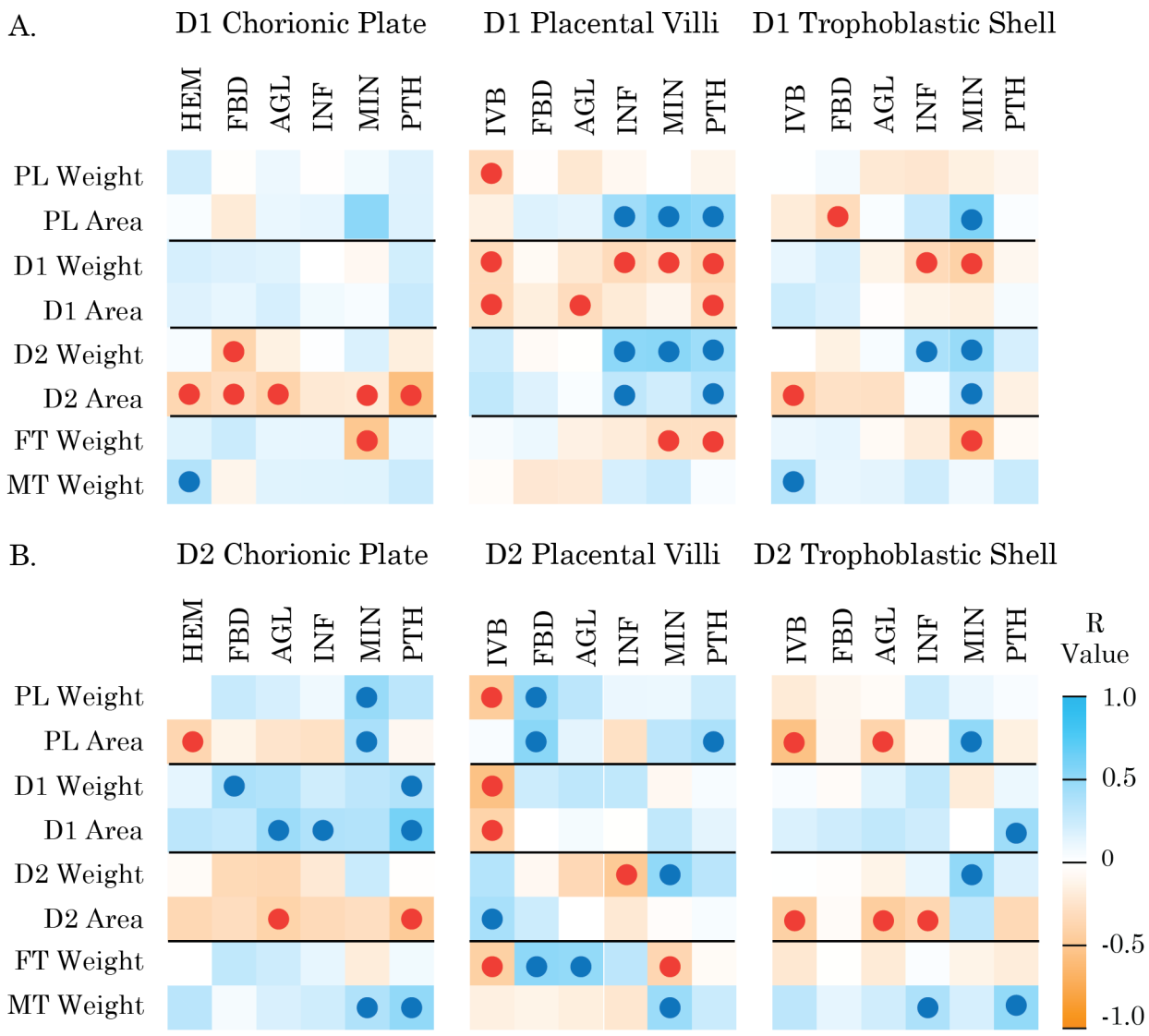

Figure 4.6. Heatmap showing fetal (FT), placental (PL, D1, D2), and maternal (MT) biometrics vs chorionic plate, placental villi, and trophoblastic shell, cotyledon sub-tissue pathology correlations in A) primary disc cotyledons and B) secondary disc cotyledons. Box color indicates relationship strength and direction. Blue boxes indicate a positive relationship (r value approaching 1, right). Orange boxes indicate inverse relationship (r values approaching -1, right). Dots within boxes indicate statistically significant relationships (α=0.05).

With this in mind, we sought to better categorize cotyledon and sub-tissue intra- and inter-pathological relationships in healthy/normal placentae (Figure 4.7). In agreement with current placental pathology understanding, most pathological features shared positive relationships with the manifestation of other pathological

features at cotyledon and sub-tissue levels (Figure 4.7). This observation was also generally observed when separating data by primary and secondary discs (Supplemental Figure 4.4)

Pathological features and the coagulation cascade

Interestingly, all pathological features besides fibrin deposition were significantly associated with their own manifestation across sub-tissues (i.e. chorionic mineralization was associated with mineralization of the trophoblast shell; chorionic inflammation was associated with villous inflammation). Furthermore, fibrin deposition showed fewer significant relationships with other pathological features, with villous fibrin specifically demonstrating significant negative relationships across multiple pathological features and sub-tissues (Figure 4.7). Similarly, intervillous blood pooling and mineralization demonstrated few significant relationships with other pathologies (Figure 4.7). Prior work suggests that IVB, mineralization, and villous fibrin deposition manifestation are positively associated with placental aging [122,143], which would explain their lack of relationship to other pathological features of discrete etiologies. Fibrin deposition showed the most positive relationships with intervillous blood pooling, tissue hematoma, and villous agglutination - especially along the trophoblastic shell (Figure 4.7) – all features of the coagulation cascade in a region of the cotyledon known to have decreased blood flow [7]. All together, these data illustrate the degree of which fibrin deposition is associated with coagulation/placental aging and does not uniformly co-express with other pathological features.

Villous agglutination inflammatory status effects inter-pathological relationships

The pathological features villous agglutination (AGL) and inflammatory villous agglutination (INF) only differ in their severity of leukocytic infiltrate (Chapter 3). As expected [118,119], AGL and INF shared a significant positive relationship cross sub-tissue and the cotyledon levels (Figure 4.7). Curiously, AGL and INF relationships with the remaining pathological features appeared to differ in

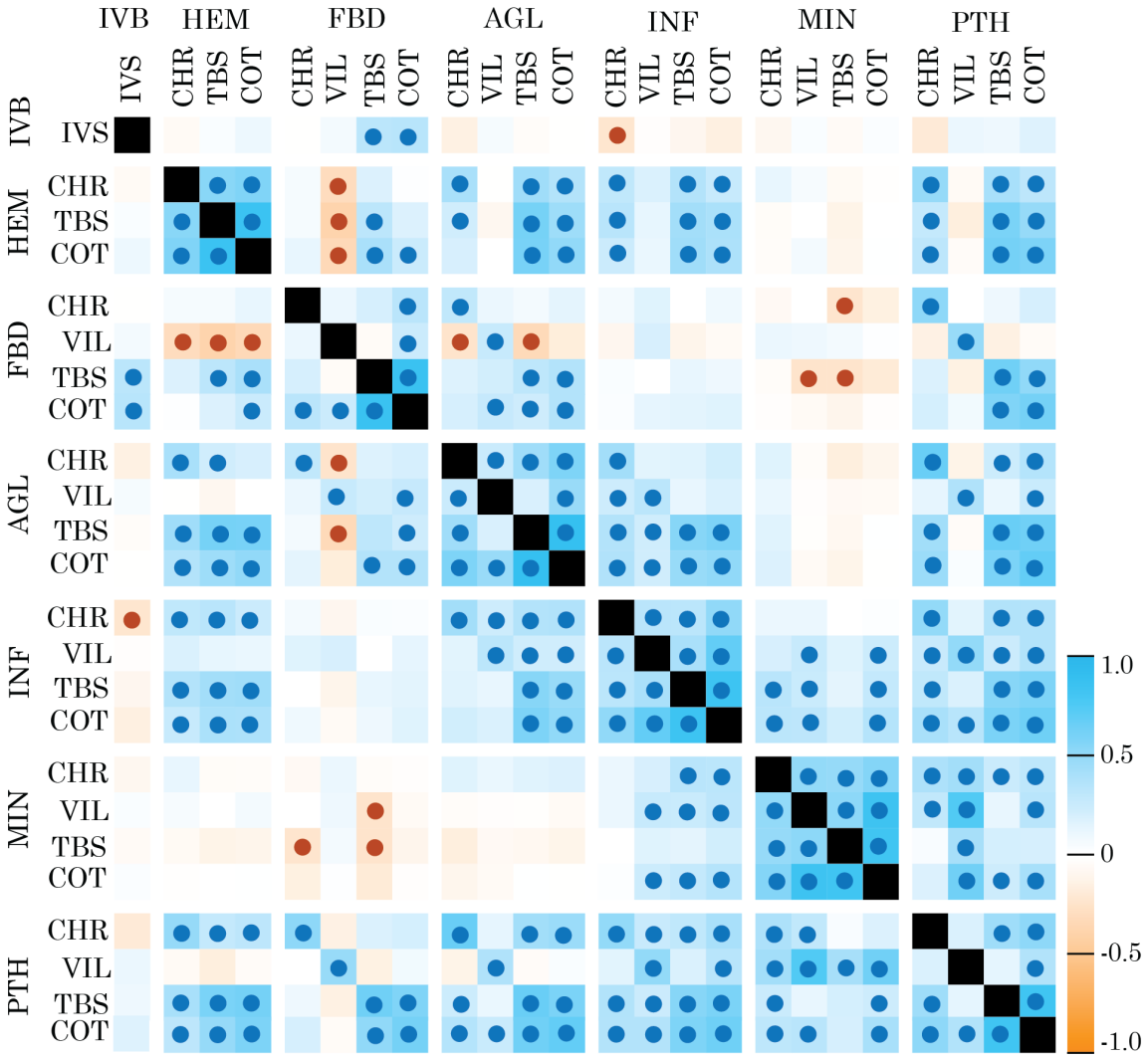

Figure 4.7. A heatmap of showing pathological feature relationships at the cotyledon and sub-tissue level. Box color indicates relationship strength and direction. Blue boxes indicate a positive relationship (r value approaching 1, right). Orange boxes indicate inverse relationship (r values approaching -1, right). Dots within boxes indicate statistically significant relationships (α=0.05).

complementary ways. AGL shared many positive associations with fibrin deposition, while INF and fibrin deposition shared none (Figure 4.7). Similarly, mineralization and inflammation showed a strong, positive relationship across sub-tissues, while AGL and mineralization shared none (Figure 4.7). When separating the data by primary vs secondary disc, we find that the strong co-expression occurring between INF and mineralization pathologies was fully supported by primary disc cotyledons and completely absent in the secondary disc (Supplemental Figure 4.4). Together, these data support a high degree of co-expression between AGL and INF, with distinct disc-specific relationships between INF and mineralization.

Inflammation and mineralization are associated with decreased blood flow

Last, we investigated the relationship between cotyledon and sub-tissue pathological features and maternal blood perfusion (Figure 4.8). Surprisingly, no coagulation cascade-associated pathologies were significantly associated with any maternal blood metrics (Figure 4.8A). However, INF and mineralization pathologies displayed an inverse relationship with blood flow at the cotyledon level, most significantly at the trophoblastic shell (Figure 4.8A). Additionally, when assessing combined pathology, total trophoblastic shell pathology was significantly associated with fill time – cotyledons with more trophoblastic shell pathology filled more slowly (Figure 4.8A). This suggests that increased pathology along the trophoblastic shell commonly observed in pregnancy [17], may be associated with diminished blood flow, manifesting in even normal/healthy pregnancy.

Disc-specific relationships between placental pathology and blood flow

When parsing the data by primary (Figure 4.8B) and secondary (Figure 4.8C) discs, we find disc-specific contributions to observed placental-wide relationships. The relationship observed between INF and mineralization pathologies and cotyledon blood flow were found to be almost completely supported by cotyledons of the primary disc (Figure 4.8B) as secondary cotyledons showed little evidence of this relationship (Figure 4.8C). Furthermore, increased blood flow was associated with increased

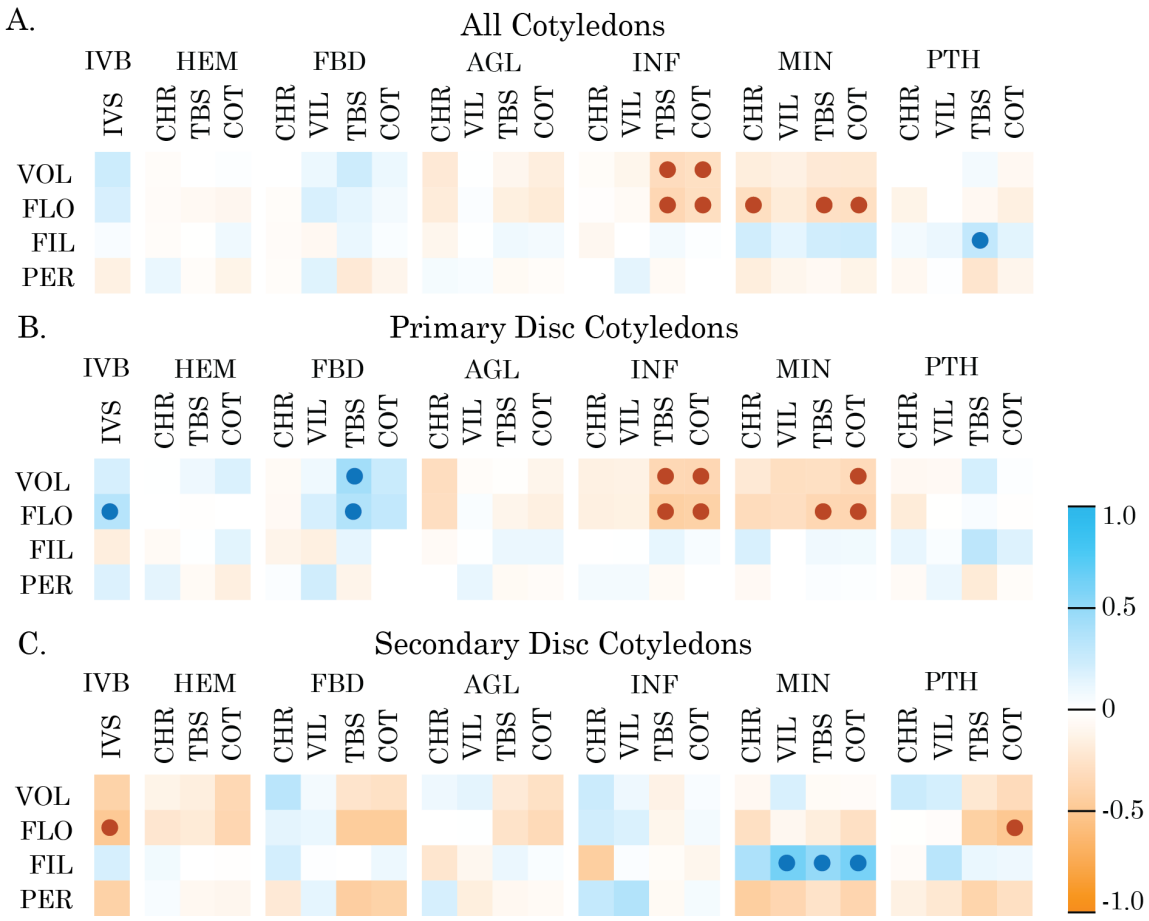

Figure 4.8. Heatmaps showing maternal blood metric and pathology relationships across A) all cotyledons, B) primary disc cotyledons, and C) secondary disc cotyledons. Box color indicates relationship strength and direction. Blue boxes indicate a positive relationship (r value approaching 1, right). Orange boxes indicate inverse relationship (r values approaching -1, right). Dots within boxes indicate statistically significant relationships (α=0.05).

villous blood pooling and fibrin deposition in the trophoblastic shell of primary disc cotyledons, in agreement with previous literature [7,143] (Figure 4.8B). In contrast, the opposite was observed in secondary cotyledons, showing a significant negative relationship between intervillous blood pooling and blood flow, as well as a negative trend connecting trophoblastic shell fibrin deposition and blood flow (Figure 4.8C). Additionally, secondary disc mineralization demonstrated significant positive associations with placental fill time across sub-tissues (Figure 4.8C), whereas little relationship between these metrics were observed in primary cotyledons (Figure 4.8B). These data demonstrate significant pathology-perfusion relationship discrepancies in cotyledons derived from primary vs secondary discs.

DISCUSSION

Relationships between pregnancy biometrics, placental pathology, and maternal blood perfusion remain largely mysterious, both at the cotyledon-level resolution and with respect to the placentae of a healthy pregnancy [17]. This has serious implications on how we interpret placental pathology, as determining severity of injury from baseline healthy/normal condition is fundamental to all pathological analysis. Here, we leveraged our novel quantitative placental pathological feature methodology alongside maternal blood perfusion monitoring by DCE-MRI to explore connections between pregnancy biometrics, placental pathology, and maternal blood delivery to the placenta in healthy/normal macaque pregnancies. We successfully observed many significant pathological correlations at cotyledon level, demonstrating that quantification of pathological features, instead of semi-quantification of

historical pathological categories [39], may be required to tease apart these relationships.

To our knowledge, this type of quantitative approach to connect biometrics, pathology, and perfusion in pregnancy is the first of its kind. Although the biological significance of any given individual finding is open to interpretation and debate; three significant relationships observed here warrant address. The first concerns the relationship between placental mineralization vs maternal blood flow and fetal weight - highlighting the significant effect of stromal mineralization in healthy pregnancy. Next, relationships observed across agglutination pathological features suggest a common etiology, challenging the way these pathological features are mechanistically perceived. And last, we provide evidence for secondary disc compensation in healthy pregnancy, and mineralization manifesting as a direct result – providing several lines of evidence for a novel etiology or placental mineralization, while challenging the idea of macaque primary and secondary discs being physiologically equivalent lobes working as a single unit [35,144].

Mineralization, maternal blood flow, and fetal weight in healthy pregnancy

Stromal mineralization was the most significant factor associated with reduced fetal weight, across chorionic, villous, and trophoblastic shell sub-tissues. The current view of this type of mineralization identifies it as an FVM pathology when sufficiently severe, effecting ~2% of all term placentae studied [19]. Basal plate mineralization (within the anchoring villi of the trophoblastic shell) is reported to occur increasingly throughout gestation [12] and not associated with reduced fetal growth [145,146]. In

contrast with these findings, we observed that stromal mineralization at the trophoblastic shell, as well as in the chorion and villi, demonstrated a strong relationship with reduced fetal weight across cotyledons.

This finding coincides with maternal blood perfusion data, as placentae that had decreased blood flow demonstrated significant increases in stromal mineralization. Cotyledons of diminished flow would have decreased intervillous blood turnover, and by extension decreased oxygen and nutrients available for transfer to fetal circulation. This may well have resulted in increased oxidative stress and damage to fetal vasculature, resulting in the observed increase in stromal mineralization. FVM pathologies of placental origin (as opposed to fetal or umbilical) are thought to occur due to increased resistance [147], endothelial damage [148], or altered vascular tone [149]. Although MVM and FVM pathologies are binned discretely, it is clear their manifestations are linked within the placenta [17]. Accordingly, our evidence suggests a strong relationship between the mineralization FVM pathology manifestation and maternal blood flow in healthy pregnancy. All together, these data suggest that direct quantification of stromal mineralization has revealed a spectral relationship with maternal blood flow and fetal outcome, previously only appreciated at the extremes [12,19,39].

The case for a common origin of pathological features

A coherent physiological cascade can be detailed linking each placental pathological feature annotation to a single inciting injury. For example, an ischemic event within a stem villus could lead to villous oxidative stress, resulting in syncytial

and stromal necrosis in that region [150]. Local tissue breakdown could further result in blood pooling, leading to a coagulation cascade involving potentially both fetal and maternal blood, resulting in varying degrees of fibrin deposition and villous agglutination [17]. The resulting inflammatory cytokines and damage-associated molecular patterns could then lead to fetal and/or maternal leukocytic infiltrate into injured/agglutinated villi, potentially exacerbated by the degree of mixing between fetal/maternal antigens/immunomes [151,152]. In addition, continued transport of minerals to ischemic/damaged vasculature, combined with the continued degradation of necrotic/fibrotic tissue within the stroma would result in stromal mineralization [153]. In cases like this, traditional pathological analysis may be less informative, as interpretation of this injury could vary widely, depending on the chance samples you acquire, and the timing of collection in relation to the injury. Along these lines, our data showed a high degree of co-expression when investigating combined pathological features across discs, cotyledons, and sub-tissues analyzed. Plainly put, as pathology increased in the primary disc of an animal, the secondary disc showed significant increase – as one cotyledon's pathology increased, pathology of all other cotyledons within the disc increased - as pathology increased in the chorion of a cotyledon, the trophoblastic shell of that same cotyledon also showed increased pathology.

As villous agglutination (AGL) and inflammatory villous agglutination (INF) annotations differed only by leukocytic infiltration degree, it is possible that these pathological features share a common origin, and their distinction is simply a matter of temporal or severity differences with respect to initial injury. The strong, positive

relationships found between AGL and INF pathologies at placental, cotyledon, and sub-tissue levels provide evidence for this interpretation. Additionally, both AGL and INF show strong positive relationships with their own manifestation across all sub-tissues, suggesting their inciting injury was not especially localized within the placenta (as chorionic and trophoblastic shell manifestations were positively associated).

A case be further supported that AGL and INF are the result of common injury when investigating how their inter-pathological relationships differed. FBD has been shown to increase within the placental parenchyma throughout gestation as a function of local hemodynamics [7] and increased intervillous blood [143]. In agreement, FBD demonstrated a positive relationship with coagulation-associated pathologies IVB and HEM, supporting the notion that a majority of cotyledon FBD was blood derived (fibrin-type fibrinoid [12]). AGL shared strong positive relationships with FBD at the cotyledon and sub-tissue level, whereas INF and FBD displayed no relationship whatsoever. Additionally, INF was the only pathology at the cotyledon-level to have a significant positive relationship with MIN, whereas AGL displayed no relationship with MIN. AGL's association with varying degrees of blood coagulation support its connection with early processes of placental damage, whereas INF's relationship to MIN suggests an extended duration since the inciting injury [19,154]. AGL and INF's strong relationship of co-expression, strong relationship with total pathology at each level of analysis, and relationships with pathologies of distinct timing, lead us to hypothesize a common etiology for a significant proportion

of AGL and INF lesions in healthy placentae. In agreement, previous analyses of related pathologies to AGL (massive perivillous fibrin deposition) and INF (chronic villitis/villitis of unknown etiology) have demonstrated their high co-expression and heavy overlap of morphological attributes [119].

A novel compensatory mechanism underlying placental mineralization

The final significant finding from our work investigating relationships within the healthy/normal macaque pregnancy was the many discrepancies observed between the primary and secondary discs, indicative of placental compensation. In general, the macaque placenta is considered a representative model of the human placenta [155,156], with primary and secondary discs working as a single functional unit [35]. The bidiscoid placenta occurs in 80-95% of all macaque pregnancies [35,122,134], while humans exhibit a bidiscoid placental rate of ~5% [157]. To our knowledge, no significant differences between primary and secondary discs have been reported in macaques when comparing physiological characteristics [144] and placental blood flow [135]. Additionally, prior study has demonstrated the ability for the primary disc to compensate for the secondary [41]. This is taken to the extreme in monodiscoid pregnancies, which have been shown to be non-inferior to bidiscoid pregnancies in all assessed health metrics [35]. However, the compensatory capacity of the secondary disc with respect to the primary has yet to be investigated.

In 2012 Victoria Roberts and colleagues demonstrated that severing the inter-placental vessels connecting macaque primary and secondary discs resulted in increased mineralization and weight in the compensating disc [41]. We observed this

positive relationship between mineralization and weight in the secondary discs of healthy/normal macaque placentae, while primary discs demonstrated a negative relationship between mineralization and placental weight. Additionally, mineralization in secondary disc cotyledons shared no relationship with any other pathological feature, was associated with significantly increased fill-time of maternal blood and showed evidence of placental compensation through an altered placental weight-maternal blood perfusion relationship. These discrepancies within the secondary disc concerning mineralization, additional pathological features, and maternal blood metrics, suggests a distinct etiology for mineralization when occurring in compensatory vs pathological discs. We hypothesize that these data illustrate some degree of physiological coordination between the two discs, and that the secondary disc acts in a compensatory manner with respect to the primary in healthy macaque pregnancy.

Distinct compensatory and pathological mechanisms resulting in mineralization manifestation would also help to explain why mineralization has historically only been associated with placental aging [19,122], as both hypothesized etiologies would likely result in increasing mineralization across gestation, even in the absence of significant APOs. This may be a macaque-specific quality by nature of a bidiscoid placenta, or this compensatory relationship may exist across cotyledons/perfusion domains of monodiscoid human placentae. Regardless, these data suggest significant placental compensation occurring within healthy/normal

primate pregnancy, and further, suggests that placental mineralization may occur by distinct etiologies, one pathological in nature, and the other compensatory.

What is a "normal" placenta?

Our findings demonstrate significant association between placental pathology manifestation, smaller fetuses, and larger dams - a phenomenon only described at the extremes in human literature [11,139]. This pathology/fetal size relationship was most significantly driven by pathology of the villous region - the interface of nutrient and oxygen exchange for the fetus, and therefore most crucial for healthy development [17]. It is our position that the morphological overlaps found in distinct pathological conditions [17,118,119], alongside the qualitative methods by which placental pathologies have been reported [15,16] have greatly obfuscated the spectral qualities of placental pathogenesis. Previously, our group has drawn semi-quantitative relationships between pathology and perfusion at the level of the placenta [39,48], however, these relationships largely broke down at the level of the cotyledon [39]. Through quantification of pathological features, we demonstrated that pathology was negatively associated with fetal weight at the cotyledon level, and that pathology was negatively associated with maternal blood flow at the cotyledon level. This novel analysis, in combination with parsing of data by disc, has illuminated previously obfuscated relationships connecting biometrics, pathology, and perfusion at the cotyledon-level, improving our understanding of the relationships between pregnancy biometrics, maternal blood metrics, and placental pathology in "normal" primate placentae.

Study Limitations and future directions

The primary limitation of this study was the exclusive use of Spearman correlations to assess biometric, pathological, and perfusion data within and across placental, cotyledon, and sub-tissue levels. We used this technique as a conservative measure of assessing non-normal, zero-inflated data. Assessment of biometrics at the cotyledon and sub-tissue level was necessarily accomplished through repeated values (for example, the same fetal weight value of a single animal was repeatedly used in correlation assessment across placenta, cotyledon, and sub-tissue levels). This likely resulted in inflating the significance of our findings across analyses. With this in mind, we did our best to be conservative in our interpretation with respect to biometrics, and only drew conclusions based on consistent trends observed across analysis throughout the study. A future direction will include customizing an elastic-net regression/lasso regression analysis, specifically designed for exploration complex, large datasets such as this.

Additionally, there are aspects of this pathological feature analysis that will likely be built upon or revised as new methods are conceived. Fibrin deposition, for example, can be derived from clotted blood (fibrin-type fibrinoid) or cellular injury (matrix-type fibrinoid) [12]. As parsing these categories apart usually requires additional staining [12], we made no attempt to distinguish between them. Despite their high co-expression, these two types of fibrin deposition can clearly manifest from discrete injury and likely explains why FBD pathology associations were weaker than

other pathological features, especially with respect to biometric and maternal blood perfusion data.

Conclusions

As current best practices in placental pathological analysis promote collecting relatively few samples and visually-estimating lesion coverage [15], it is no surprise that a large percentage of complicated pregnancies exhibit no overt placental pathology [127]. We utilized the rhesus macaque model to investigate normal/healthy primate pregnancy, allowing increased control and depth of analysis largely unavailable in human pregnancy research. Our work outlines novel quantitative relationships between biometrics, placental pathologies, and maternal blood perfusion metrics, highlighting the significant, continuous nature of these relationships within healthy pregnancy. Importantly, we also uncovered the significant differences inherent in the primary vs secondary disc cotyledons of the macaque placenta – helping to explain why common pathological lesions did not significantly correlate with blood metrics at the cotyledon level in our prior analyses [48]. Together, these findings greatly contribute to the question currently plaguing all placental researchers [17] - understanding what a “normal” placenta really is.

SUPPLEMENTAL INFORMATION

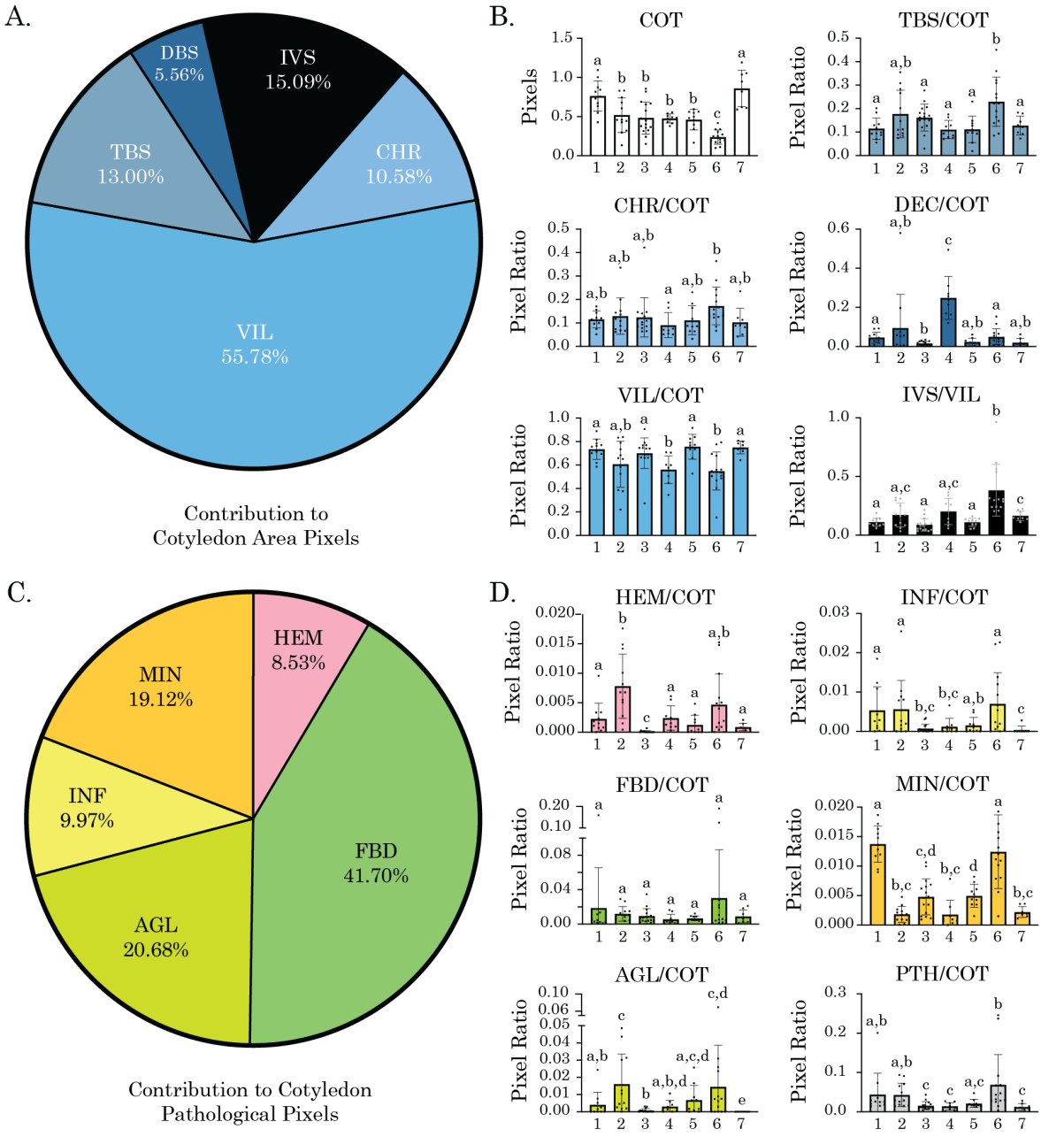

Supplemental Figure 4.1. Cotyledon areas and pathological features summary. A) Graph showing % contribution of sub-tissues (chorionic plate [CHR], placental villi [VIL], trophoblastic shell [TBS], decidua basalis [DBS]) and intervillous space (IVS) to total cotyledon area. B) Total cotyledon pixels, sub-tissue pixel area ratios, and IVS pixel ratios across all animals (1-7). C) Graph showing % contribution of pathologies (tissue hematoma [HEM], fibrin deposition [FBD], villous agglutination [AGL], inflammatory villous agglutination [INF]) and stromal mineralization [MIN]) to total cotyledon pathology. D) Individual and total pathology pixel ratios across cotyledons of all animals (1-7). Data points represent individual cotyledon values; bars represent the mean +/- the standard deviation. Common letters above bars indicate no statistical difference (α=0.05).

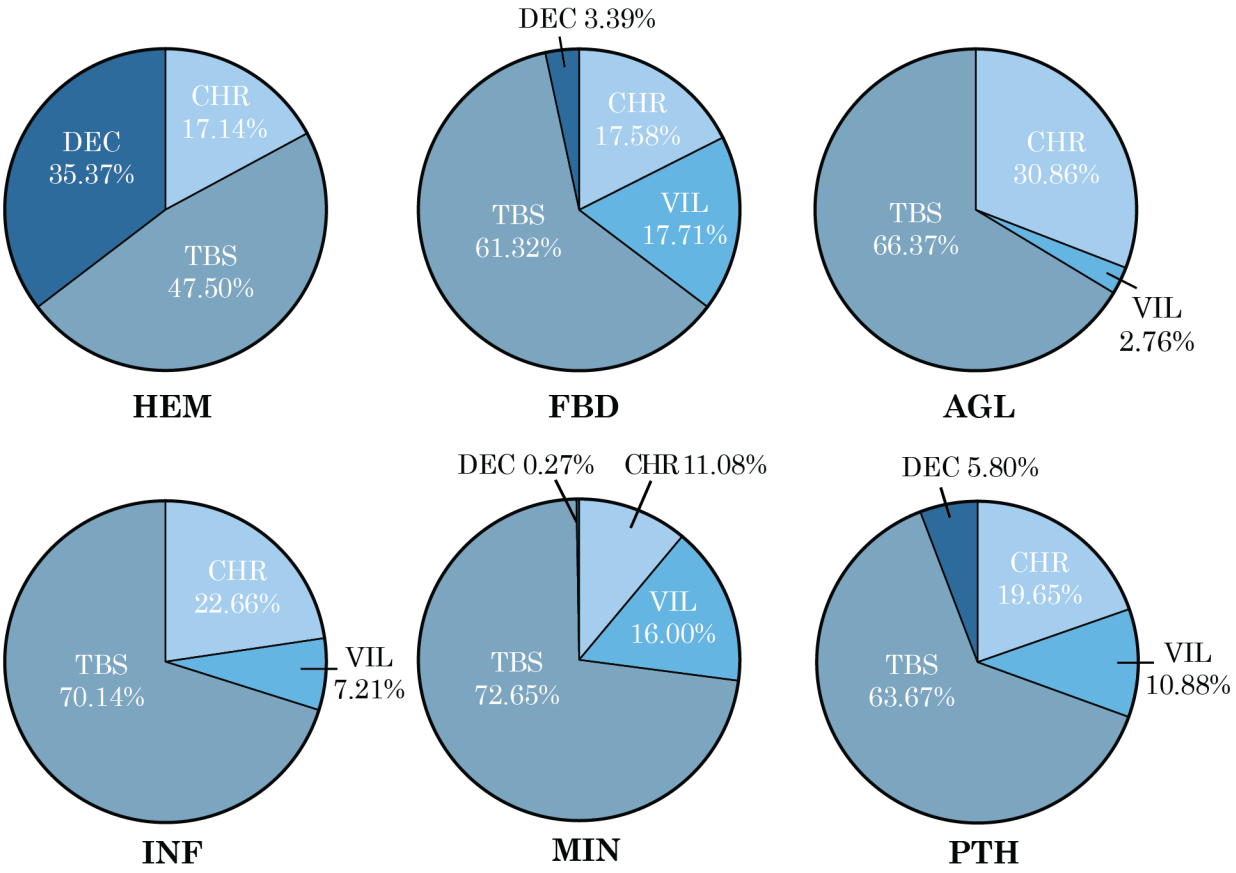

Supplemental Figure 4.2. Pie charts indicating the percent of pixels of individual (tissue hematoma [HEM], fibrin deposition [FBD], villous agglutination [AGL], inflammatory villous agglutination [INF]) and stromal mineralization [MIN]) and combined placental pathologies by cotyledon sub-tissue (chorionic plate [CHR], placental villi [VIL], trophoblastic shell [TBS], decidua basalis [DBS]).

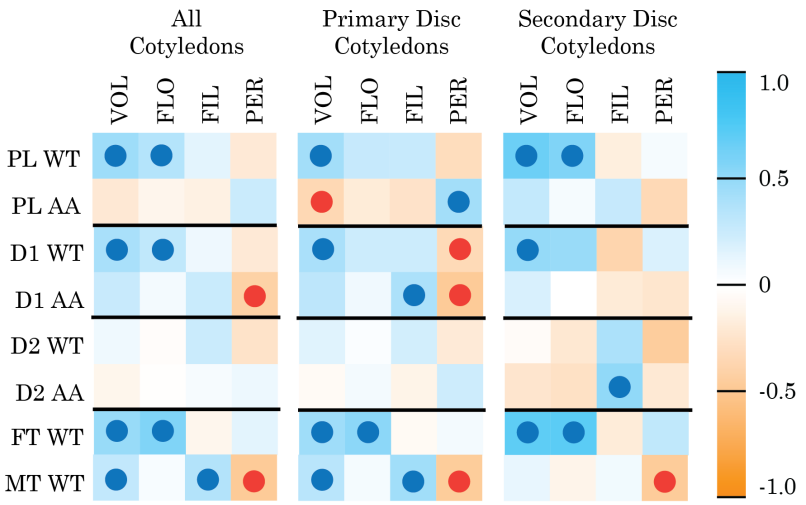

Supplemental Figure 4.3. A heatmap showing cotyledon-level maternal blood perfusion relationships with biometrics. Box color indicates relationship strength and direction. Blue boxes indicate a positive relationship (r value approaching 1, right). Orange boxes indicate inverse relationship (r values approaching -1, right). Dots within boxes indicate statistically significant relationships (α=0.05).

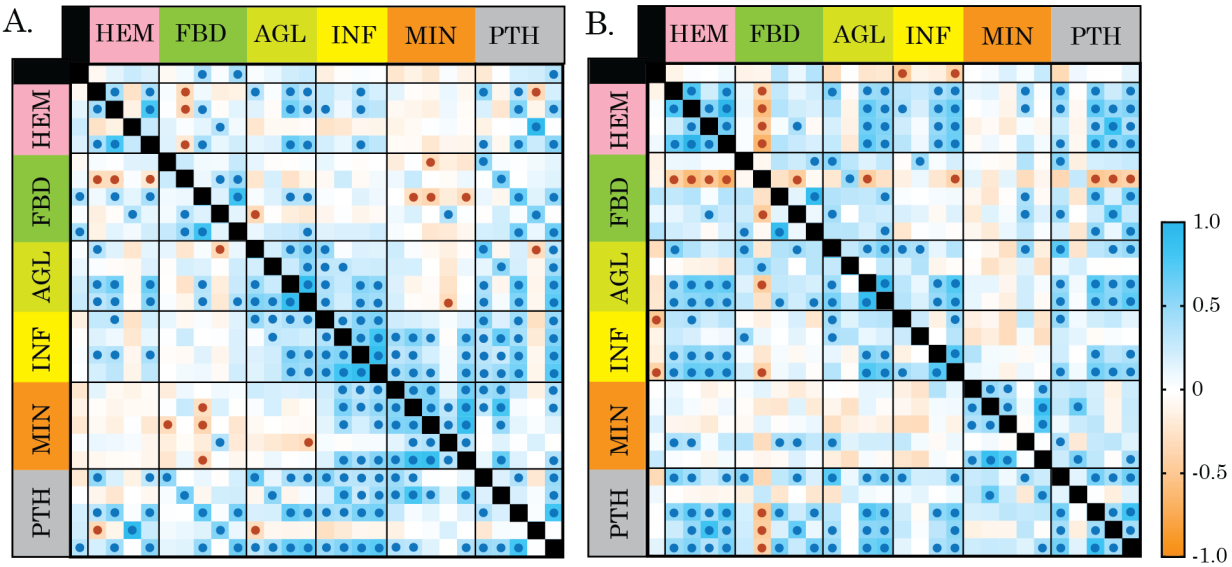

Supplemental Figure 4.4. Sub-tissue-level pathological relationships. Heatmaps of showing pathological feature relationships at the sub-tissue level in A) primary disc and B) secondary disc cotyledons. Individual rows/columns within pathologies mirror Figure 3.14. Box color indicates relationship strength and direction. Blue boxes indicate a positive relationship (r value approaching 1, right). Orange boxes indicate inverse relationship (r values approaching -1, right). Dots within boxes indicate statistically significant relationships (α=0.05).

CHAPTER 5

AN INFLAMMATORY MODEL OF PLACENTAL INSUFFICIENCY

Placental insufficiency is evidenced clinically through detailed pathological analysis of vascular malperfusion and inflammatory lesions [15]. Placental inflammatory lesions can span both fetal and maternal compartments, and have been subdivided into categorizes such as chorioamnionitis, acute or chronic villitis, chronic histiocytic intervillositis (CHIV), and villitis of unknown etiology (VUE), based on the predominant immune cell populations observed and the tissue in which they infiltrate [16,17,158]. Despite their unique diagnostic criteria, many of these lesions contain overlapping features of immune cell infiltration and villous destruction, and have been observed to manifest in tandem [17,118].

Placental stromal mineralization

Inflammatory injury at the placenta can also include vascular obliteration within the villi, leading to secondary degeneration of tissue [16] and tissue mineralization. Placental mineralization is a histological feature most commonly associated with placental age [122]. Although this lesion has been found to present secondarily after an initial injury [19], it has not been historically deemed diagnostically or prognostically significant [19,123]. However, excessive focal mineralization in the placenta has been associated with fetal abnormalities, aneuploidies, disease, and demise [123]. Mineralization of the villous stroma seems to originate from fibrotic or necrotic tissue, indicating prolonged injury within these regions [19]. It has been hypothesized that villous stroma mineralization results from

continued transport of minerals across the syncytia in the absence of fetal circulation and subsequent uptake [124]. Notably, a recent histological analysis of 1698 placentas associated segmented villous mineralization with sclerotic/hypovascular chorionic villi, suggesting this mineralization lesion as an independent pathological feature of vascular malperfusion within the fetal compartment [19].

MCP-1 injection to model placental inflammation

Animal models of placental insufficiency have led to a better understanding of placental malperfusion and chorioamnionitis pathogenesis through experimental techniques such as placental arterial ligation [41] and pathogen challenge [159]. However, our current understanding of sterile inflammatory lesions comes solely from the use of in vitro models [160] and clinical retrospective studies [161], highlighting the need for a reliable in vivo model. To this end, we utilized monocyte chemoattractant protein-1 (MCP-1 or CCL2) to model the villous injury and increased leukocytes observed in placental inflammatory lesions. This chemokine plays a crucial role in monocyte/macrophage migration and infiltration into tissues [162], along with memory T cells [163], dendritic cells [164], and activated NK cells [165]. *In vivo*, monocytes and macrophages are a major source of MCP-1 production [162], resulting in directed migration along the chemokine's concentration gradient [162].

We investigated the effect of a supraphysiological dose of MCP-1 at the MFI during midgestation on placental health, maternal placental blood perfusion into the intervillous space, and fetal outcomes in the macaque. We hypothesized that MCP-1 administration would result in sterile inflammation and placental insufficiency,

evidenced through increased inflammatory injury pathology, recruitment and activation of leukocyte populations at the MFI, decreased maternal blood perfusion to the placenta, and fetal growth restriction. Surprisingly, we observed decreased placental mineralization, a trend towards increased placental blood perfusion, and healthy fetal outcomes following MCP-1 placental injection.

METHODS

Ethical use, care, and breeding of macaques

We utilized the macaque as our pregnancy model, due to its phylogenetic proximity, long gestational period, and placental physiology similarity to humans [10,34]. All experimental procedures and tissue collections were performed in accordance with the NIH Guide for the Care and Use of Laboratory Animals and under the approval of the University of Wisconsin College of Letters and Sciences and Vice Chancellor Office for Research and Graduate Education Institutional Animal Care and Use Committee, protocol G006209. Wisconsin National Primate Research Center (WNPRC) macaques were housed with compatible mates and monitored for breeding and menstruation. Date of conception was estimated based on initiation of the menstrual cycle, observation of copulation with presence of ejaculate, and ultrasound measurements of fetus and gestational sac.

Intraplacental injections

All injection solutions were prepared using sterile tools and aseptic techniques within a biosafety cabinet. MCP-1 solutions were prepared by dissolving 100 μg of MCP-1 (RP1284Y, KingFisher Biotech) in PBS with 0.1% BSA. The MCP-1 solution

was thoroughly mixed, filtered (0.22 μm), and drawn into a 1.0 mL syringe, totaling 100 μg of MCP-1 in 500 μL for placental injection. Saline control solutions were prepared using the same protocol, omitting the addition of MCP-1. To determine the acute effects of MCP-1, two macaques (n=1 saline, n=1 MCP-1) received placental injections, while full-term effects were investigated through placental injection of eight pregnant macaques (n=4 saline, n=4 MCP-1, Figure 1). One macaque dam (Animal 6) was used repeatedly - treated with saline in an initial pregnancy, then MCP-1 in a subsequent pregnancy. All injections were performed by a board-certified obstetrician, between gestational day (GD) 100 and 105, under ultrasound guidance, targeting the trophoblastic shell/decidual interface of the anterior placental disc.

Placental and fetal dissection

Cesarean sections were performed on pregnant macaques at GD 108 for acute study, and GD ~155 for full-term study (10-14 days before full gestation [133], to avoid potential early live births). All placental and fetal tissues were collected, noting relevant weight and length biometrics. Authors were unable to record the organ weights of one fetus of a saline-treated dam, resulting in a fetal organ weight n=3 within saline group. Placental discs were photographed, and placental attachment area was determined through ImageJ (Version 1.54) using diameter measurements taken at dissection. Placental cotyledons were classified through visual and textural tissue assessment. A full-thickness whole-placental section was taken for histological analysis, after which individual cotyledon boundaries were dissected. Full thickness sections were then obtained from each cotyledon for quantitative histological

analysis, along with biopsies for cytokine analysis. Decidua was removed from remaining cotyledon tissue for further processing. Cotyledon sections were processed as previously described [39]. Hematoxylin and eosin (H&E) stained slides were scanned for whole slide imaging (WSI) at 4x magnification and stitched together using a Nikon Eclipse Ti2 microscope with NIS-Elements AR software version 5.02.006 (Nikon Instruments Inc., Melville, NY, USA).

Placental histological analyses

Whole-placenta center cuts were assessed for histopathological lesions via brightfield microscopy on H&E stained tissues by a senior pathologist along the guidelines outlined in the 2016 Amsterdam Consensus [15]. Additionally, center cuts from each individual placental cotyledon were FFPE processed as previously described [30], and subject to the quantitative placental pathological annotation analysis described in Chapter three. For the purposes of this study, only pathology at the cotyledon level was quantified. In addition, a subset of cotyledons were also stained and digitally annotated for CD45+, to assess leukocyte populations and confirm accuracy of inflammatory villous agglutination (INF) annotations. Serial sections stained with a CD45 antibody demonstrating great agreement/overlap with INF annotation (Figure 5.1).

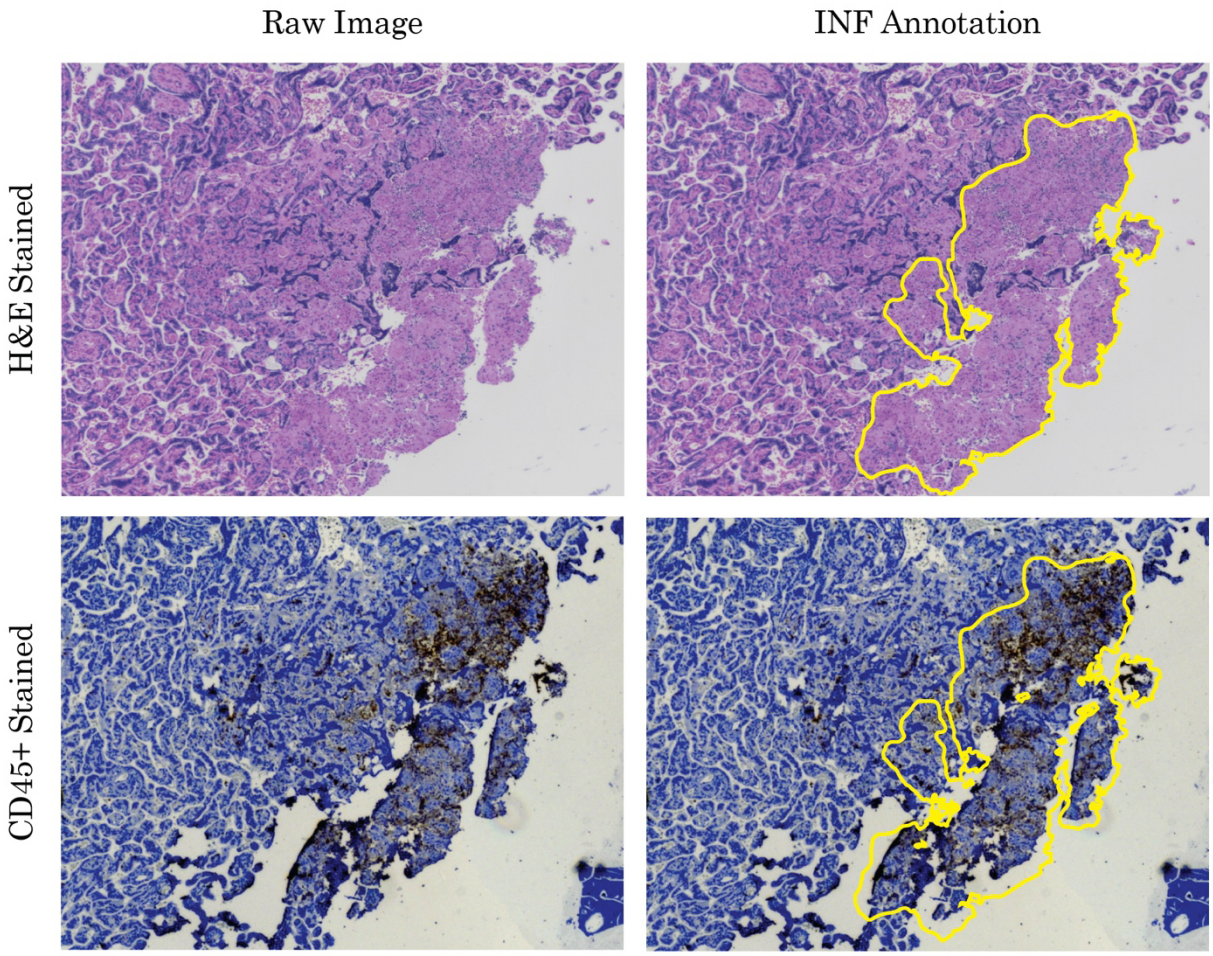

Figure 5.1. Representative images of goo agreement between inflammatory villous agglutination (INF) pathology annotation and leukocytic infiltration as visualized by CD45+ staining.

As was described in Chapter 4, all histological quantification was reported as a ratio, in relation to total cotyledon pixels (i.e. total feature pixels/total cotyledon pixels), to account for discrepancies in cotyledon sample size.

CD45 immunohistochemistry

To capture total leukocyte levels at the cotyledon, digital annotation and quantification was performed on CD45 immunohistochemically stained WSIs. Cotyledon tissues sections were incubated with a primary antibody against CD45 (Abcam, AB40763), alongside a negative control IgG at the same concentration.

Staining was developed for 120 s with Betazoid Diaminobenzidine (DAB) chromogen (Biocare Medical, Concord, CA, USA).

Tissue homogenization

Placental tissue homogenization has been described previously by our group [166]. Briefly, tissue biopsies were placed in a snap cap tube with PBS, 10 µl/mL of Halt Protease and Phosphatase Inhibitor Cocktail 100X (Thermo Scientific, Waltham, MA), and stainless-steel beads. Biopsies were homogenized using a TissueLyser II (Qiagen, Germantown, Maryland) and centrifuged to remove debris. Protein concentration was then quantified using the Micro BCA Protein Assay and read on the SpectraMax Plus 384 Microplate Reader (Molecular Devices).

Placental cytokine analysis

Cytokines were analyzed using the LEGENDplex NHP Inflammation Panel (13-plex, Biolegend, San Diego, CA) multiplex assay. Briefly, tissue homogenates were diluted in PBS to reach a standard protein concentration of 1 mg/mL. All samples were run in duplicate. The assay beads were then fixed with 4% paraformaldehyde (PFA) for five minutes. Samples were analyzed on the Attune NxT Flow Cytometer (ThermoFisher Scientific, Waltham, MA), and the resulting FCS files were analyzed using LEGENDplex Data Analysis Software Suite (Biolegend, San Diego, CA). The mean value of each sample was calculated from duplicate wells. Resulting values were then z-score normalized and visualized using the ComplexHeatmap R package [167].

Mononuclear cell isolation and flow cytometry

Mononuclear cells (MCs) were isolated from the decidua as previously described [168]. Peripheral blood mononuclear cells (PBMCs) were isolated from whole blood before injection and 24 hours after treatment, from the dam's periphery. Isolated MCs were then stained for flow cytometric analysis as previously described [169]. In brief, isolated decidual MCs and PBMCs first labeled with LIVE/DEAD® fixable blue stain (Invitrogen), followed by staining with fluorochrome-conjugated monoclonal antibodies, and diluted in BD Horizon Brilliant™ Stain Buffer. For intracellular targets, MCs were fixed and permeabilized overnight with FoxP3 Transcription Factor Staining Buffer (Invitrogen), followed by sequential incubation with antibodies targeting transcription factors. Samples were acquired using a Cytek Aurora spectral cytometer. Authors were unable to collect decidual samples from one MCP-1 treated dam, resulting in an n=3 for MCP-1 decidual flow cytometry analyses.

Flow cytometry data analysis

FCS files were unmixed using SpectroFlo software with optimized single stain controls, then pre-gated in FlowJo v.10 (FlowJo LLC, Ashland, OR). Major immune populations were then identified to confirm proper unmixing. Dimensionality reduction analysis was performed within the R package Spectre [170] as previously described by our group [166]. Resulting identified clusters were annotated based on expression of lineage defining markers. Cluster abundance across samples was determined within Spectre and visualized using ComplexHeatmap package.

MRI acquisition and processing

Macaques from full-term experiments received monitoring by ferumoxytol dynamic contrast enhanced (DCE) MRI to assess changes in maternal blood perfusion to the placenta across gestation. Dams were imaged under anesthesia in right-lateral position on a 3.0-T clinical scanner (GE Healthcare) around GD 95, 115, and 145 (Figure 5.2). DCE MRI data was acquired utilizing the same techniques and specifications outlined in Chapter 3.

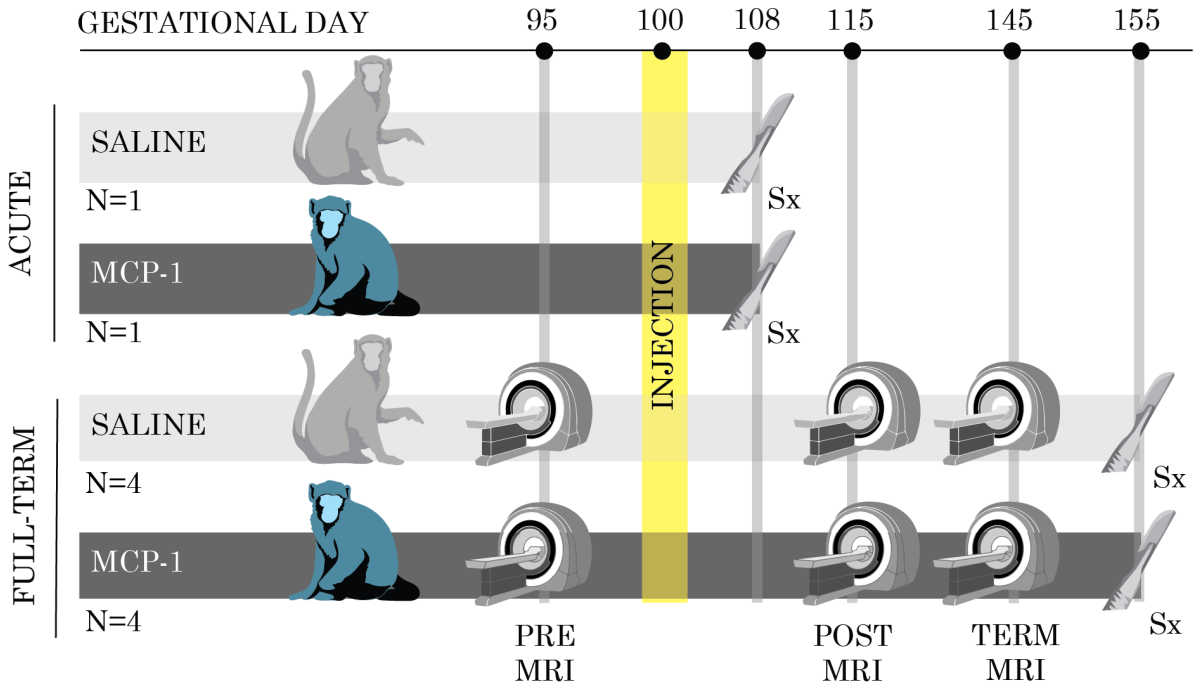

Figure 5.2. MCP-1 injection experimental design. A graphical representation of acute (n=2) and full-term (n=8) groups receiving either MCP-1 or saline injection. Injection, MRI, and C-section surgery (Sx) procedures are shown, with respect to the approximate gestational day they occurred.

Statistical analyses

Changes in acute inflammatory injury, CD45+ staining, and cotyledon villous mineralization were determined by Wilcoxon rank-sum test (α=0.05), while acute

CD45+ villous stroma staining was determined by Fisher's Exact Test (α=0.05). Changes in full-term inflammatory injury, CD45+ staining, and villous stroma mineralization were determined using a mixed linear model with zero inflation (treatment as a fixed factor, dam as a random factor, α=0.05), developed using publicly available R packages (R, version 4.4.2). For flow cytometry analysis, statistical differences in cluster abundance were determined by Mann-Whitney test or 2-way ANOVA when appropriate. MRI placental perfusion metrics (maternal blood flow and placental fill time) and fetal biometrics were analyzed for significance by t test (α=0.05, GraphPad Prism, version 10.4.1).

RESULTS

MCP-1 acutely increased leukocytes and decreased mineralization in the villous stroma

Inflammatory lesions and MVM pathologies are thought to contribute significantly to placental insufficiency, leading to adverse pregnancy outcomes (APOs) for the developing fetus [17,171]. To assess the immediate impact of MCP-1 injection on placental pathology, acute whole-placental center cuts were examined by a senior pathologist for lesions indicative of placental injury and insufficiency. Center cuts showed no significant gross lesions, with only mild, acute inflammation noted in both saline and MCP-1 acute-treated placentae. In agreement with this observation, cotyledon quantitative assessment of all acute samples showed no difference in inflammatory injury or CD45+ staining between MCP-1 and saline groups (Figure

5.3). However, acute MCP-1-treated cotyledons displayed decreased mineralization of villous stroma compared to controls (Figure 5.3).

Given these acute findings, the full-term impact of MCP-1 injection on pathologies of placental insufficiency was assessed. At term, whole-placental center cuts showed coagulative necrosis and multifocal mineralization in both saline and MCP-1 groups. Additionally, two of the four MCP-1–treated placentas had sufficient lesions (coagulative necrosis, infarctions, and retroplacental hemorrhage) to constitute MVM pathology. We next performed cotyledon quantitative assessments on full-term placental cotyledons to compare saline and MCP-1 groups. MVM pathologies in general were not observed at the cotyledon level. Additionally, as was noted acutely, inflammatory injury and total leukocyte populations did not differ between treatments, while a significant decrease in villous stromal mineralization was observed in MCP-1-treated cotyledons when compared to saline (Figure 5.3). This decrease in mineralization at full term with MCP-1 injection was further observed when assessing cotyledons from Animal 6, a dam who first received saline, then MCP-1 treatment in a subsequent pregnancy.

Interestingly, an increase in CD45+ cell clustering within the villous stroma of stem and anchoring villi was noted in roughly half of the acute cotyledons (e.g., Figure 5.4). Binning these cotyledons by treatment revealed that MCP-1 injection revealed a significantly higher incidence of leukocyte clustering in the villous stroma. Furthermore, these same regions of leukocyte clustering were notably devoid of mineralization in cotyledons of MCP1-treated placentae (Figure 5.4). In agreement

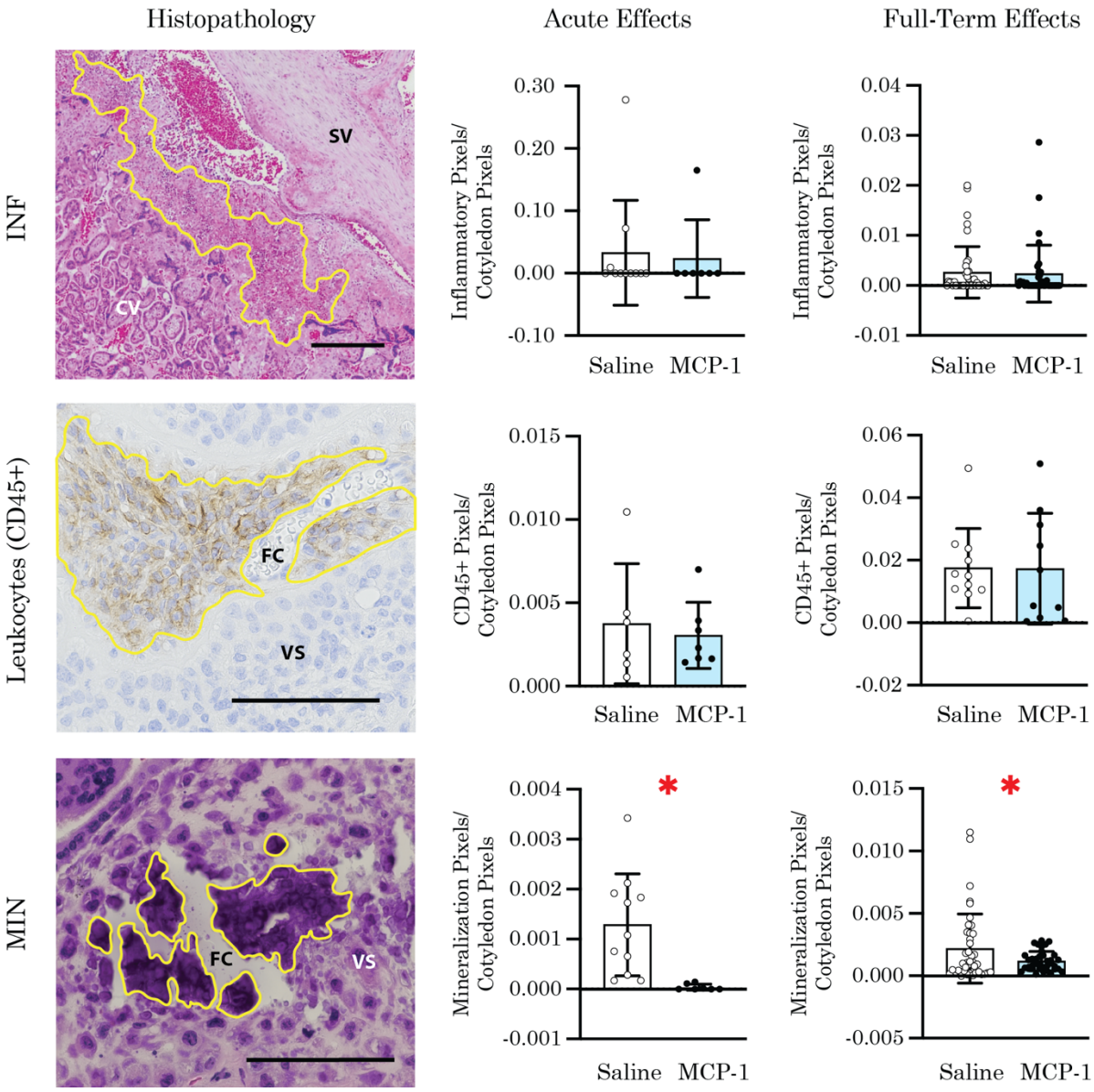

Figure 5.3. MCP-1 injection effects on placental histopathology. Top) A representative image of inflammatory injury (yellow) sandwiched between chorionic villi (CV) and a stem villi (SV) (H&E-stained, 4x magnification, scale bar = 500 µm) alongside graphs depicting the ratio of inflammatory injury pixels/total area pixels for acute and full-term exposure saline (and MCP-1 injected cotyledons. Center) a representative image of villous stroma (VS) CD45+ staining (yellow) around a fetal capillary (FC) (hematoxylin counter-stained, 40x magnification, scale bar = 100 µm) alongside graphs depicting the ratio of CD45+ pixels/total area pixels for all acute cotyledons and random subset of full-term exposure saline (n=11) and MCP-1 (n=10) injected cotyledons. Bottom) a representative image of villous stroma (VS) mineralization (yellow) around an obliterated fetal capillary (FC)(H&E stained, 40x magnification, scale bar = 100 µm) alongside graphs depicting the ratio of villous mineralization pixels/total area pixels for acute and full-term exposure saline and MCP-1 injected cotyledons. All bars represent the mean, all error bars represent +/- standard deviation. An asterisk "*" represents a p value ≤ 0.05.

with acute findings, the villous stroma mineralization was largely confined to the anchoring and stem villi near the maternal floor in full-term cotyledons (Figure 5.4). Histological examination of H&E and CD45+ stained serial-sections strongly suggested their identity as either macrophages or dendritic cells based on cellular morphology and location (Figure 5.3 and 5.4). However, we did not observe leukocyte clustering within the villous stroma at full-term, in contrast to acute outcome tissues (Figure 5.4).

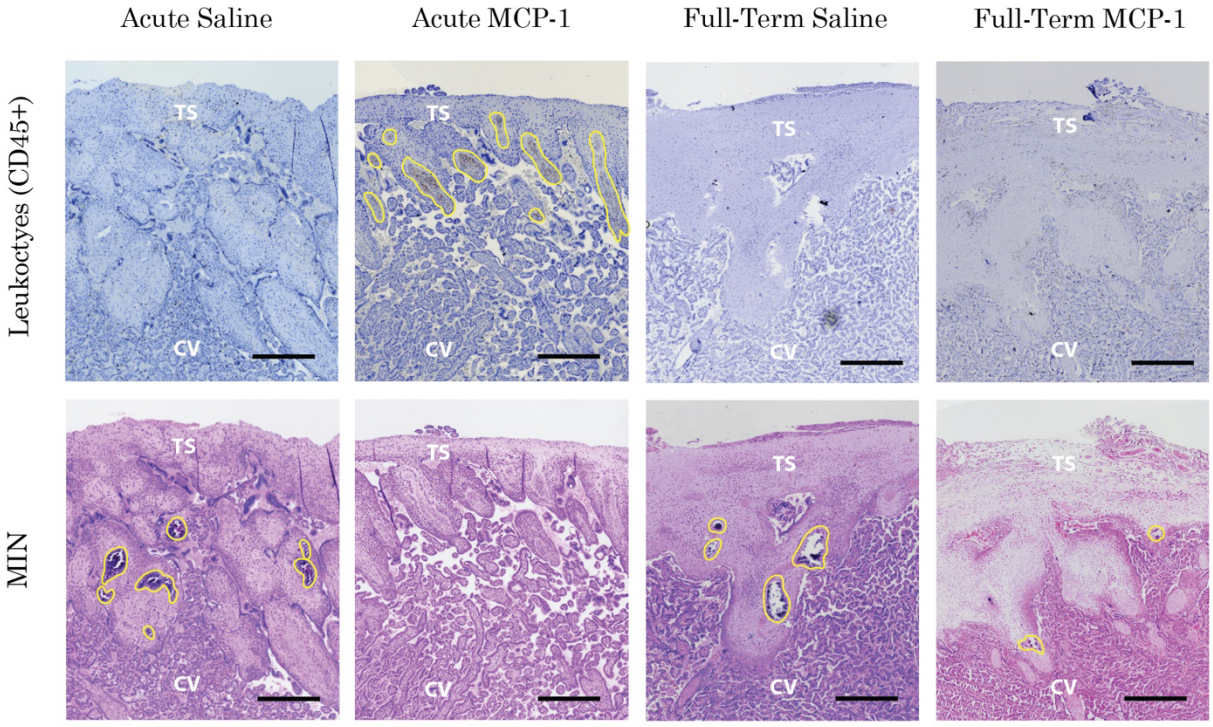

Figure 5.4. Mineralization and leukocyte staining near the maternal floor. Representative images of stromal mineralization (MIN) and leukocytes in acute and full-term saline and MCP-1 injected placentae by annotation (yellow) along the basal plate, where chorionic villi (CV) anchor along the trophoblastic shell (TS) (4x magnification, scale bars = 500 μm).

MCP-1 increased decidual dendritic cells at full-term

To better understand how MCP-1 injection at the MFI impacts the decidual immunome acutely, we utilized FlowSOM, an unsupervised clustering algorithm for

flow cytometry data coupled with tSNE visualization, to assess decidual cell populations (Figure 5.5). First, we found only subtle differences between the acute saline and MCP-1 treated deciduae when assessing major immune populations (Figure 5.5A). Specifically, we found that the innate lymphoid cell (ILC) cluster was more abundant in the MCP-1 injected decidua compared to saline (41.85% to 24.71%; Figure 5.5A). Further clustering within the ILC population revealed that trNK cells were overrepresented in the MCP-1 treated decidua, while representing a smaller proportion of ILCs in the saline treated decidua (Figure 5.5B), suggesting that MCP-1 injection led to changes in the decidual immunome.

These observations of an altered decidual immunome in acute deciduae prompted investigation of MCP-1 induced changes in our full-term outcome deciduae. We first identified all major immune populations in the deciduae from saline and MCP-1 treated placentae (Figure 5.6A and B). Assessing cluster frequency, we found that the saline and MCP-1 samples did not cluster separately (Figure 5.6C), suggesting that MCP-1 did not alter the decidual immunome over the full-term time frame. However, we did observe a trend of increased T cells, and significant increase in dendritic cells and a decrease in B cells in the MCP-1 group (Figure 5.6D). As MCP-1 has the capacity to modulate differentiation [172,173] and directly attract dendritic cells (DCs) [164], this increase in DCs suggests that MCP-1 had influenced this immune cell population at term. Given the acute changes observed in the ILC compartment, we focused our analysis on the ILC population in our full-term data

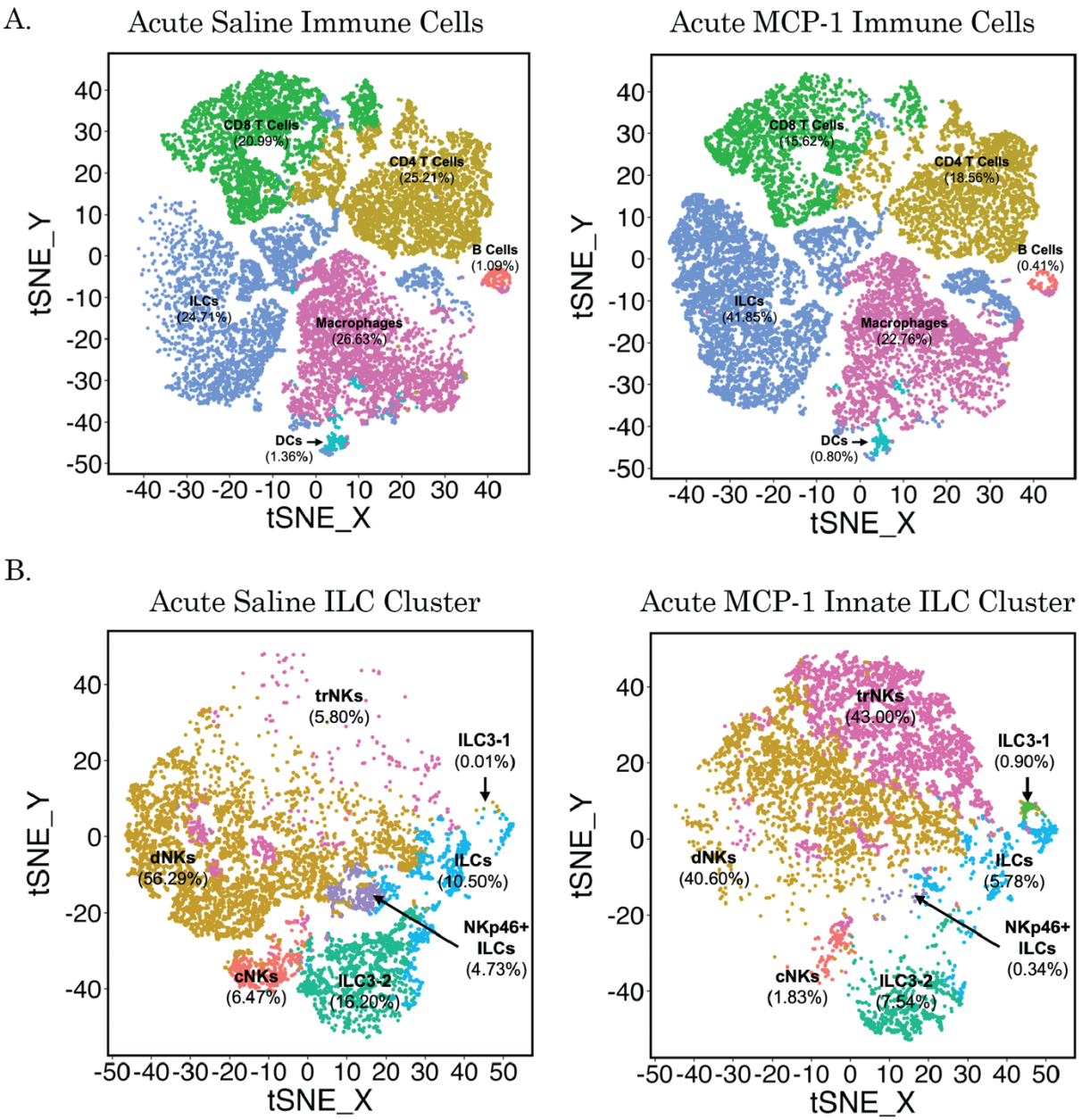

Figure 5.5. MCP-1 Injection on decidual immune populations acutely. A) tSNE plots depicting clusters with percent contribution of individual immune cell populations of saline (left) and MCP-1 (right) decidual cells. B) tSNE plots depicting sub-clusters with percent contribution of individual immune cell populations from the ILC compartment of saline (left) and MCP-1 (right) decidual cells.

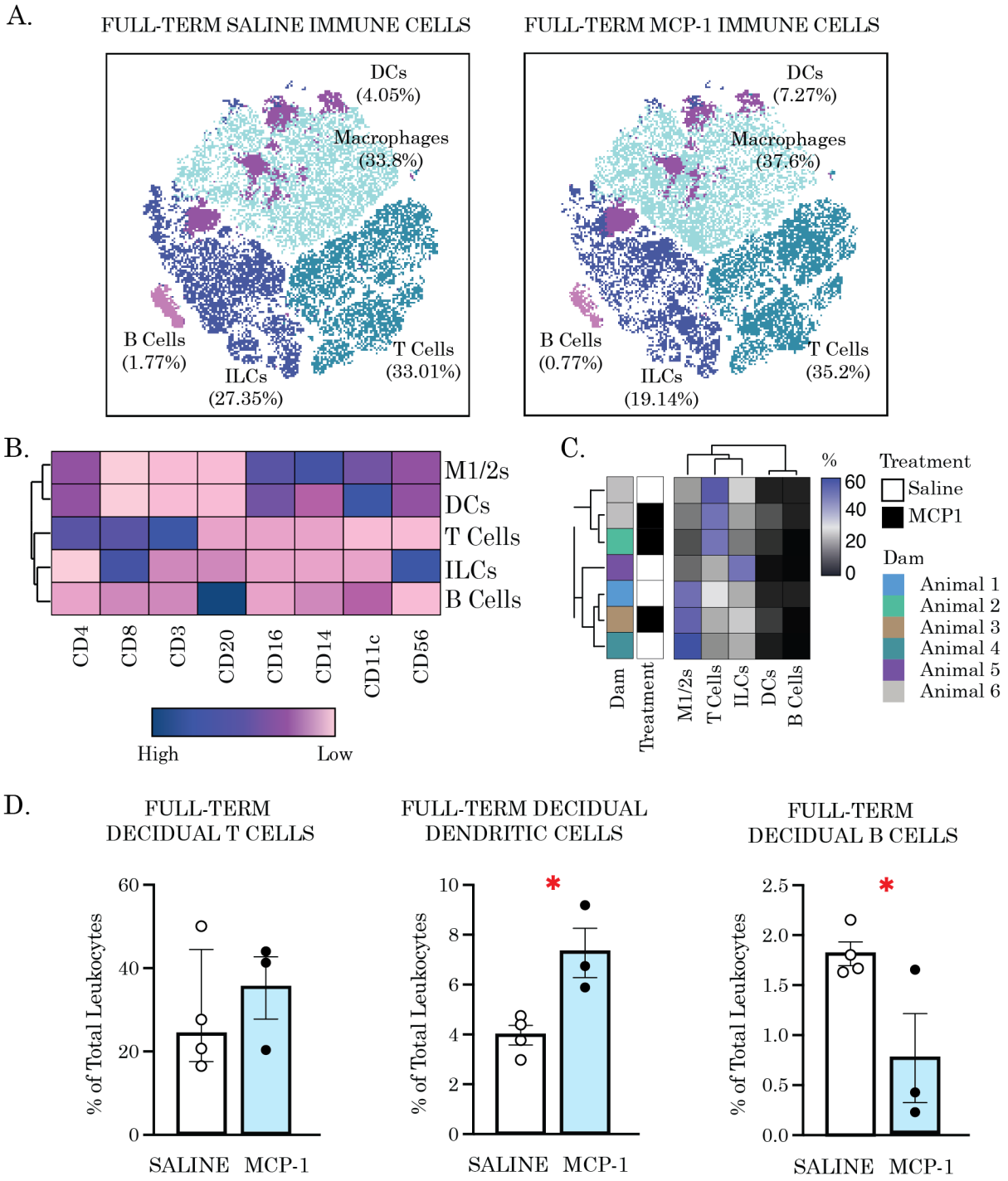

Figure 5.6. MCP-1 injection on decidual immune populations at full-term. A) tSNE plots depicting 5 clusters with percent contribution of individual immune cell populations of saline (left) and MCP-1 (right) decidual cells. B) A heatmap summarizing marker expression across the 5 immune cell clusters identified. C) A heatmap summarizing the percent of each immune cell cluster in relation to treatment and dam. D) T cell (left), Dendritic cell (center), and B cell (right) percent of total leukocytes in full-term decidual cells. An asterisk "*" represents a p value $\leqslant 0.05$.

(Figure 5.7). FlowSOM clustering revealed a total of 11 clusters within decidual ILCs (Figure 5.7A and B). The majority of decidual ILCs were activated dNKs (Figure 5.7C), based on the expression of CD69 (Figure 5.7B). However, we did not find any differences in the relative proportions of ILC clusters across the treatment groups.

Due to the significant increase in dendritic cells with MCP-1 treatment, we further analyzed antigen presenting cells (APCs) between the two groups (Figure 5.8). We found 10 distinct clusters within decidual APCs (Figure 5.8A and B). However, we did not find any differences in cluster distribution between the treatment groups (Figure 5.8C). As a final analysis, we assessed the levels of a select number of cytokines associated with high and low levels of inflammation in a subset of placental cotyledon homogenates (Figure 5.9). We found no difference in cytokine levels across the cotyledons assessed between the two treatment groups (Figure 5.9). Taken together, our data indicate that MCP-1 had a subtle effect on the MFI immunome in at full-term.

MCP-1 injection resulted in healthy blood perfusion and fetoplacental biometrics

MRIs were conducted ~5 days before MCP-1 injection (pre), ~15 days after injection (post), and ~45 days after injection (term) to determine whether MCP-1 altered perfusion dynamics (Figure 5.10). When assessing effects ~45 days after injection, total placental blood flow and fill time showed no significant differences between treatments (Figure 5.10A). When assessing the change in these metrics between ~15 and ~45 days post injection, MCP-1 treated placentae trended towards increased blood flow and decreased fill time (Figure 5.10B).

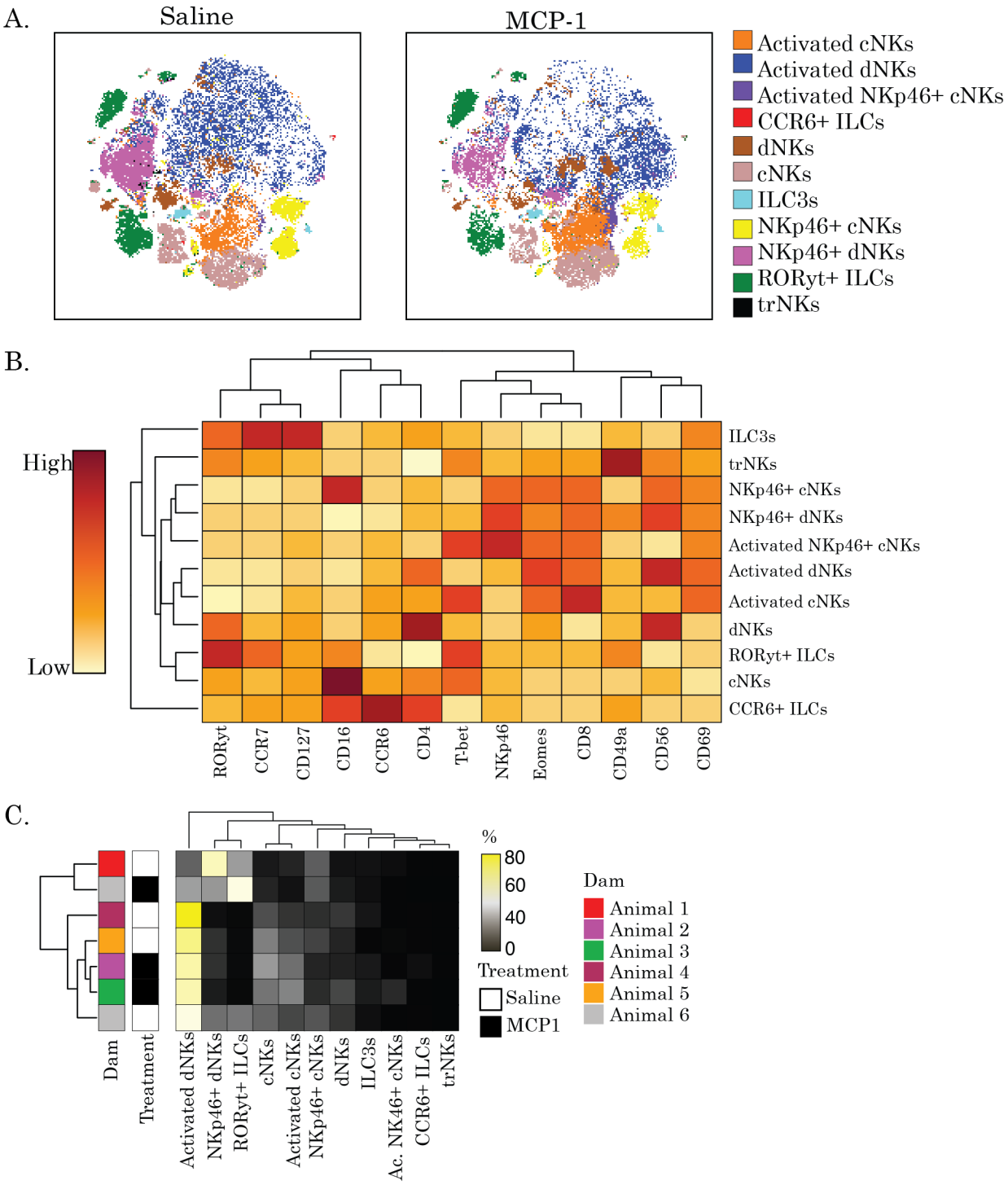

Figure 5.7. MCP-1 injection on decidual ILCs at full-term. A) tSNE plots depicting 11 clusters with percent contribution of individual ILC immune populations of saline (left) and MCP-1 (right) decidual cells. B) A heatmap summarizing marker expression across the 11 ILC clusters identified. C) A heatmap summarizing the percent of each ILC cluster in relation to treatment and dam.

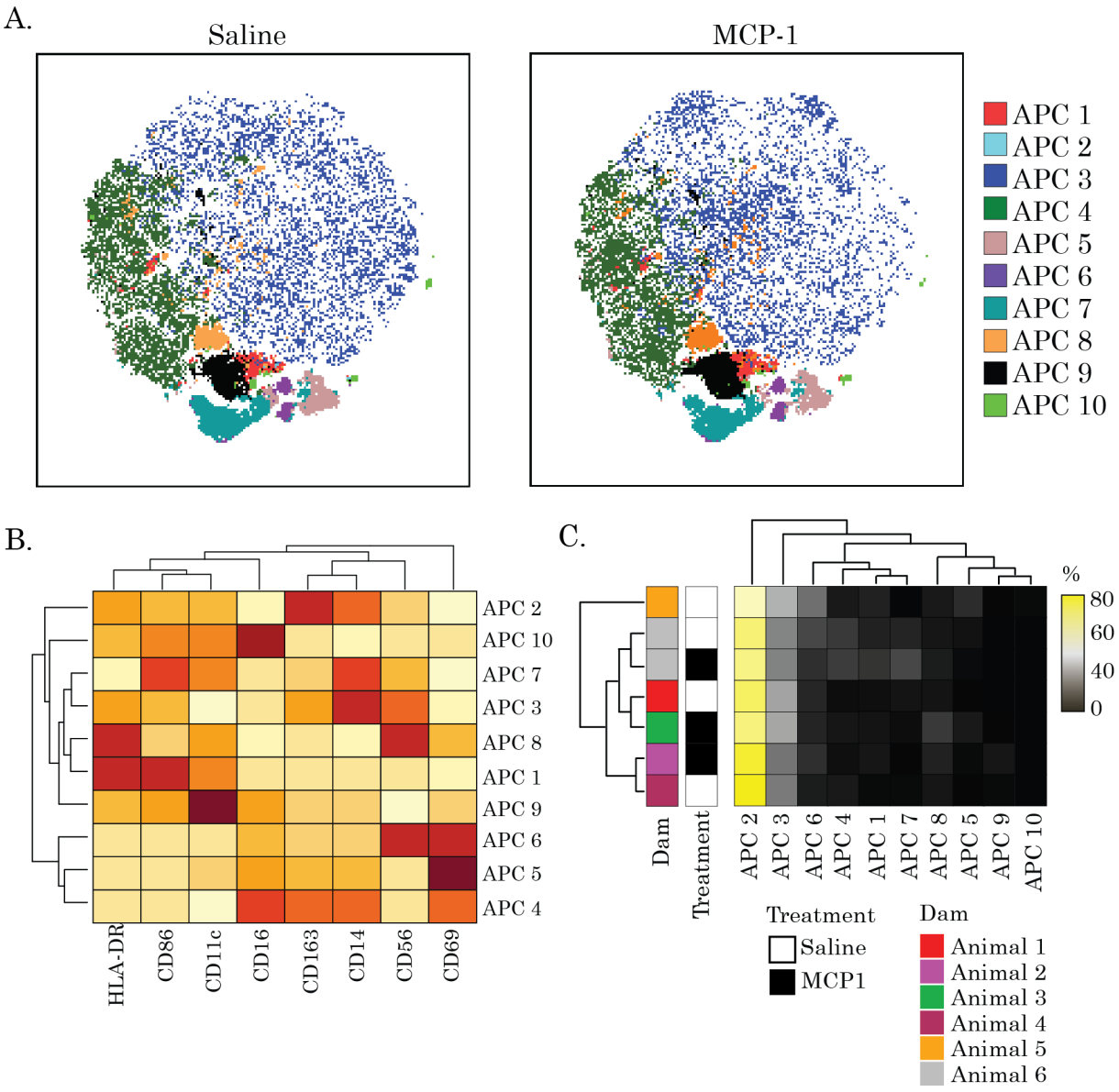

Figure 5.8. MCP-1 injection on decidual APCs at full-term. A) tSNE plots depicting 10 clusters with percent contribution of individual APC populations of saline (left) and MCP-1 (right) decidual cells. B) A heatmap summarizing marker expression across the 10 APC clusters identified. C) A heatmap summarizing the percent of each ILC cluster in relation to treatment and dam.

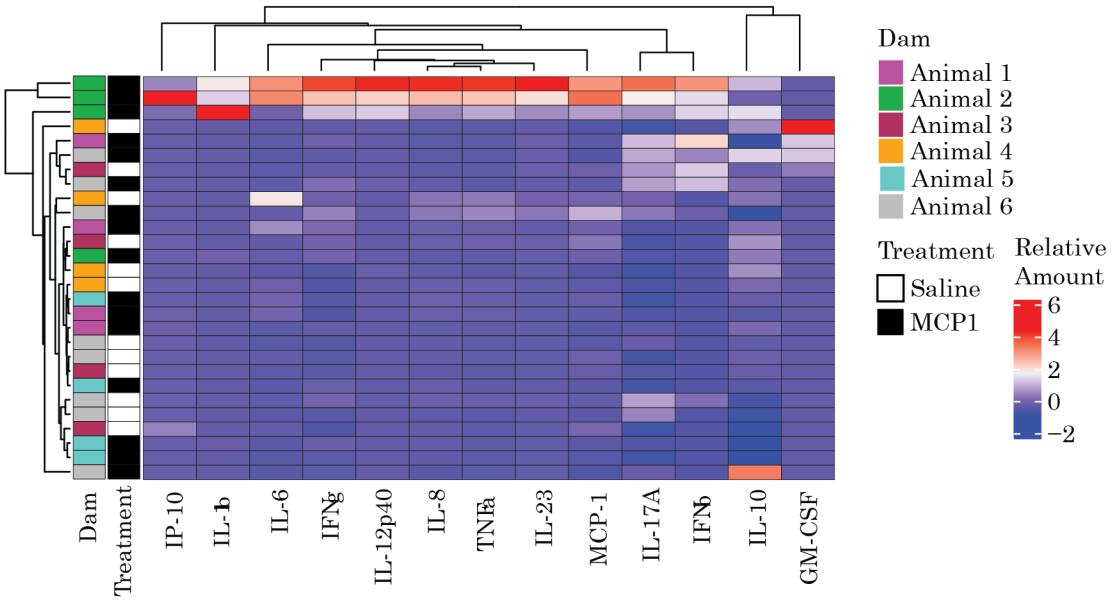

Figure 5.9. MCP-1 injected placental cotyledon cytokine expression at full-term. A heatmap summarizing the relative amount of each cytokine within placental tissue, with respect to treatment and dam.

MCP-1 treatment did not affect fetal biometrics - as gross weights of the fetal body, organs, and placentae did not differ between saline and MCP-1 treated groups (Figure 5.11A). This was further evidenced when normalizing organs to fetal weight, placental weight, or placental attachment area (Figures 5.11B-D). Interestingly, we did observe a non-significant trend of larger fetuses in the MCP-1 group, when normalized to their placentas (Figure 5.11B and D). Overall, the non-significant trends of increased maternal blood flow and fetal growth, and decreased placental fill time, suggests a trend towards increased maternal vascular function with MCP-1.

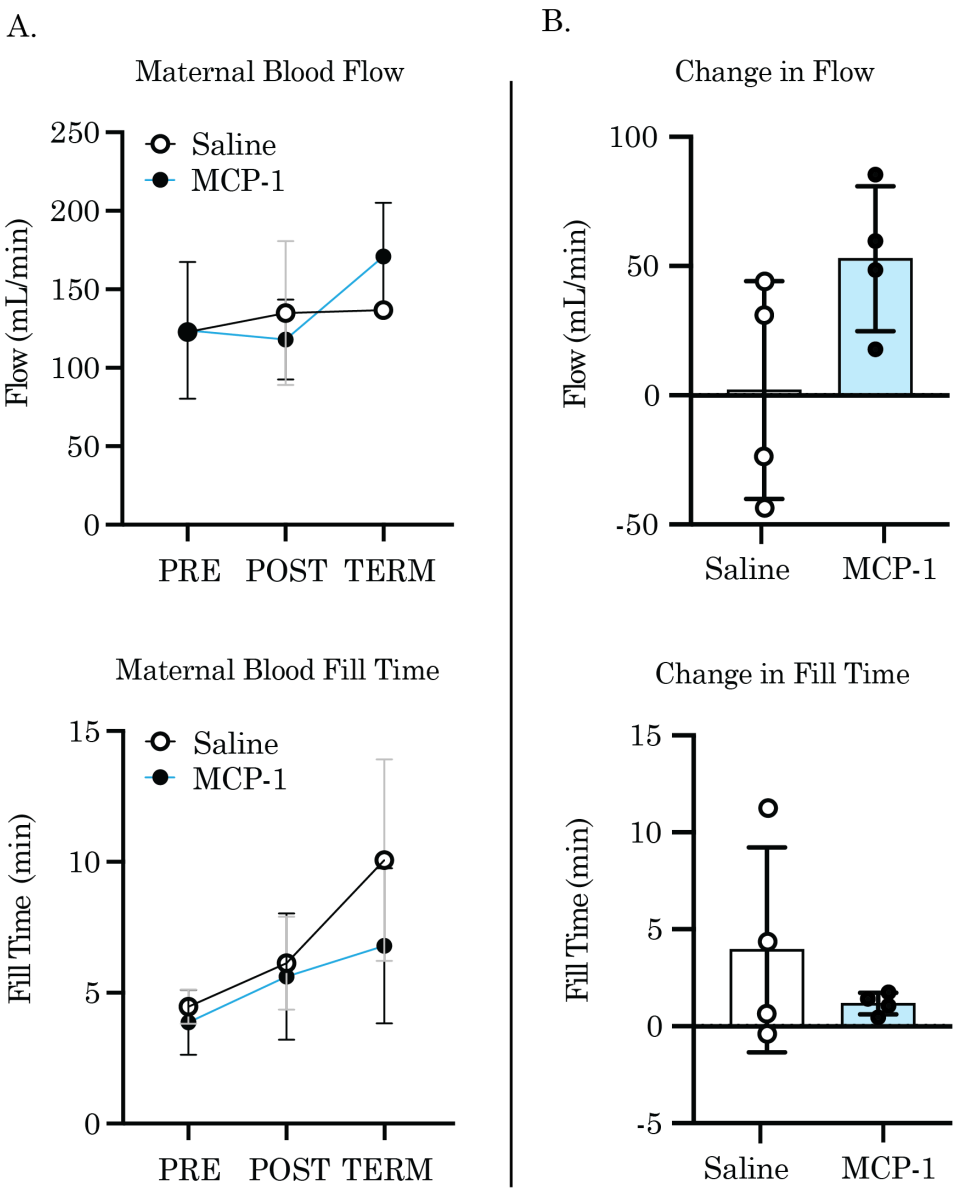

Figure 5.10. Placental maternal blood perfusion metrics by DCE MRI. A) Maternal blood flow (top) and fill time (bottom) of MCP-1 and saline placentae across gestation. Pre-injection MRIs occurred on GD ~95, followed by a post-injection MRI (POST, GD ~115) and full-term MRI (TERM, GD ~145), as described in Figure 1. B) The change in maternal blood flow (top) and fill time (bottom) of MCP-1 and saline placentae between post (GD ~115) and term (GD ~145) timepoints. Data points represent individual animal placental values, bars represent the mean, all error bars represent +/- standard deviation.

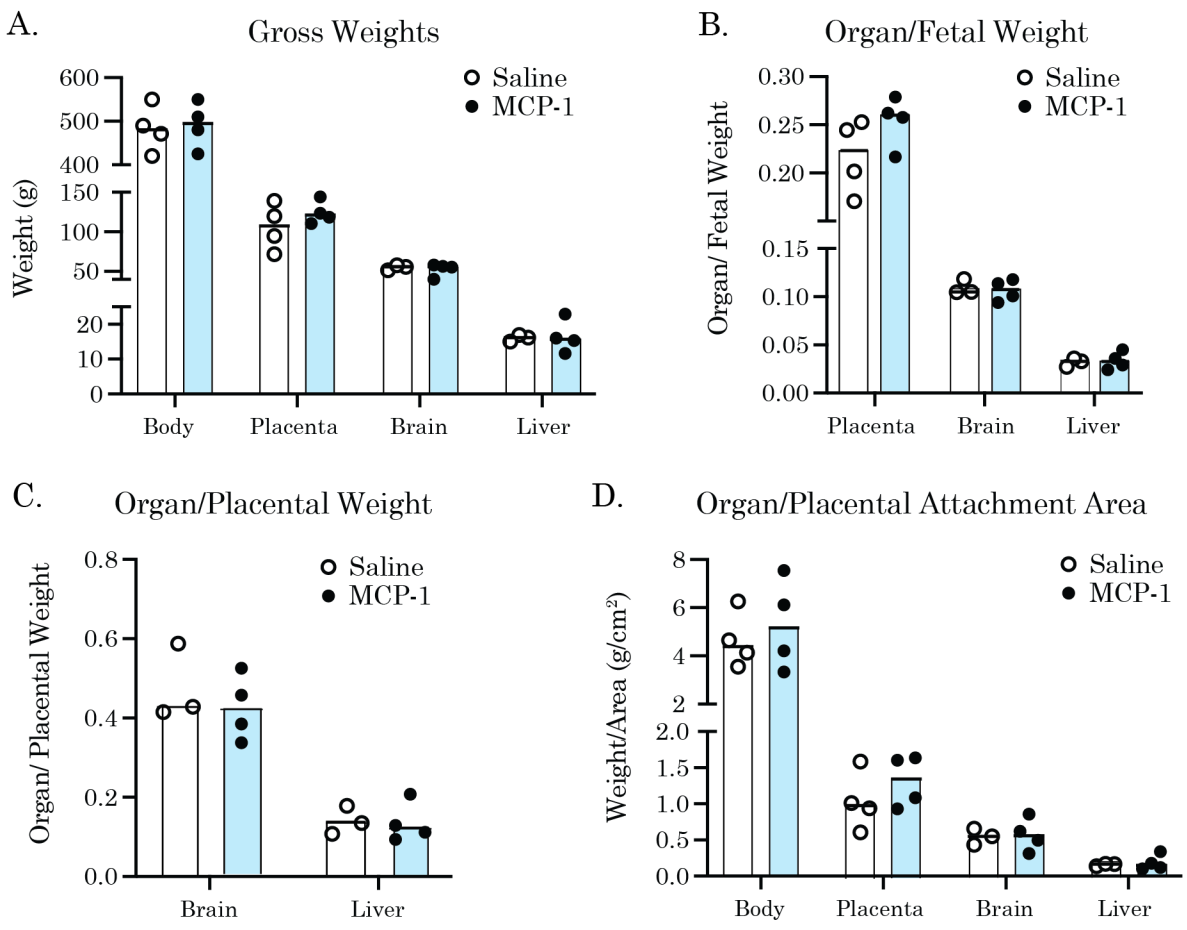

Figure 5.11. A) Gross weights of fetoplacental tissues alongside B) the ratio of organ to fetal weight, C) the ratio of organ to placental weight, and D) organ weights standardized to placental attachment area in saline and MCP-1 injected animals. All bars represent the mean value of data points analyzed by t test. An asterisk "*" represents a p value $\leqslant 0.05$.

DISCUSSION

Altered immune dynamics have been observed in placental insufficiency pathology [161], resulting in adverse outcomes of pregnancy [174]. In this study, MCP-1 injection into the macaque MFI did not result in overt inflammatory injury or adverse fetal outcomes. Although MCP-1 has historically been associated with inflammatory lesions and increased tissue pathology, it also has well-established roles in angiogenesis [175,176] and wound healing [177]. Our study demonstrates the

ability of a 100-μg dose of MCP-1 to decrease fetal vascular malperfusion pathology and sustain healthy fetal outcomes in the macaque pregnancy.

MCP-1 decreased mineralization of the villous stroma

An unexpected observation of our study was the decrease in villous mineralization that we noted in the MCP-1 treatment group. It seems reasonable to conceptualize mineralization at the placenta as a result of uncleared cellular debris, considering macrophages actively work to phagocytose apoptotic and necrotic cellular tissue [178,179]. In addition, in vitro work has shown increased MCP-1 expression and macrophage activation in rat epithelial cells co-cultured with calcium phosphate [180], the primary component of placental mineralization [181]. We hypothesize that Hofbauer cells (HBCs, fetal macrophages) were likely recruited to the villous stroma and activated by MCP-1, where they phagocytosed local necrotic, fibrotic, and mineralized tissue [179]. Further, we propose that this activated HBC state must have been either prolonged, or sufficiently ubiquitous across the placentae, as to sustain the reduced villous stoma mineralization throughout pregnancy between the MCP-1 and saline treatments.

MCP-1 did not diminish placental maternal blood perfusion

A trend towards increased maternal blood flow and decreased fill time at the placenta was also observed following MCP-1 injection. Acute damage and inflammation can result in vasodilation and increased blood flow to tissue [182], while prolonged injury and associated inflammation can lead to reduced blood flow and slower filling tissue filling, through vasoconstriction mediators such as TNF-α and

IL-6 [183,184]. In agreement, our group has previously demonstrated decreased maternal blood flow in placentae exhibiting chronic pathology [39,48]. Additionally, Roberts et al. observed increased mineralization in both pathological and compensatory discs of macaques in response to significant maternal blood flow disruption and injury [41]. The significant decrease in villous mineralization and trend towards increased placental perfusion presented here suggests an increase in placental vascular functionality with MCP-1 injection. The elevated decidual dendritic cell populations observed with MCP-1 treatment may further support this notion, as dendritic cells play a unique role in maternal immune response and fetal tolerance regulation in the decidua [185]. In agreement with this interpretation, elevated pathology (leukocytic infiltration and fibrosis) have been observed in the adipose tissue of MCP-1 knockout mice, contrary to their hypothesis that the presence of MCP-1 would exacerbate injury [186].

Curiously, placental insufficiency MVM pathologies were also reported in placental-wide center cuts from 2 of 4 the animals receiving MCP-1 injection. As these findings were not observed across MCP-1 cotyledons, it is possible that these MVM pathologies did not contribute significantly to placental perfusion in the MCP-1 group, despite the lesions' eponym. It is also possible that some pathological features commonly associated with placental insufficiency are not the primary source of injury, but rather a histological manifestation of placental compensation, such as inflammatory injury. A more exhaustive, quantitative analysis of placental pathologies would provide better resolution of the frequency and location of these

insufficiency lesions - allowing a stronger basis by which to draw associations between placental pathology, maternal blood perfusion metrics, and fetal outcomes.

MCP-1 and pathological manifestation

Historically, significant levels of MCP-1 have been documented in disease states of inflammation and pathological blood perfusion, such as multiple sclerosis and stroke [175]. The tissue pathologies resulting from these conditions are similar to those observed in placental insufficiency, such as fibrinoid necrosis, leukocytic infiltrate, mineralization, vascular pathologies, and infarction pathologies [12,187]. Currently, there is contradictory evidence for the role that MCP-1 plays in pathological pregnancies – as both increased [188], and decreased [189] MCP-1 levels in maternal peripheral blood have been associated with APOs. MCP-1 expression in vivo appears to be mainly associated with polarization to an anti-inflammatory, TH_2 phenotype [190], in agreement with our findings. As our group likely utilized an injection of MCP-1 several orders of magnitude higher than its maximally effective concentration [191], it stands to reason that MCP-1 alone does not drive pathological inflammation in cases of placental insufficiency – a notion supported in non-pregnancy injury models [186]. It appears that an additional injury, cytokines, and/or specific antigens must be present to produce inflammatory pathologies and adverse pregnancy outcomes observed clinically.

Our findings illustrate a paradoxical yet compelling role for MCP-1 at the maternal-fetal interface: rather than exacerbating inflammatory damage as initially hypothesized, MCP-1 promoted acute leukocyte recruitment and notably decreased

mineralization within placental villi, suggesting a beneficial immune-driven clearance mechanism. Importantly, these protective effects occurred without compromising placental blood perfusion or fetal growth, challenging conventional perceptions of MCP-1 solely as a mediator of pathological inflammation.

Study limitations and future directions

An argument can be made against only utilizing one injection of MCP-1 at midgestation, as opposed to periodic doses throughout pregnancy to maintain a more stable MCP-1 gradient at the MFI. This single-injection method was chosen to maximize the sterile effects of MCP-1, while minimizing mechanical injury from repeated injection of placental tissue, as the effect of a single placental injection on immune populations and placental pathology is unknown. In future work, multiple doses of MCP-1 may work to further substantiate or undermine the trends in placental perfusion and fetal biometrics observed here. Furthermore, despite the relatively low sample size inherent to non-human primate study, we believe the effects of MCP-1 on pregnancy described here provide valuable insight into the complicated role chemokines play in placental lesion pathogenesis.

Conclusions

In conclusion, future research aimed at modeling sterile placental inflammation should not only address mechanisms by which inflammatory injury can be robustly induced, but also carefully dissect the conditions under which immune cells recruited to the placenta mediate protective versus pathogenic effects. Clarifying these conditions may unlock new therapeutic strategies—potentially harnessing

chemokine signaling pathways to improve placental resilience and mitigate the impact of placental insufficiency. Deeper mechanistic insight into immune modulation at the MFI could ultimately enhance our ability to diagnose, manage, and prevent pregnancy complications associated with placental dysfunction and placental inflammation [192].

Publication:

L.T. Keding, J. Vazquez, R.-Y. Liu, E. Bove, J. Dorobek, H.A. Simmons, K.M. Antony, J.L. Racine, D.M. Shah, O. Wieben, T.G. Golos, A.K. Stanic, Monocyte Chemoattractant Protein-1 (MCP-1) Decreases Mineralization of the Villous Stroma in the Macaque Placenta, Placenta (2025). https://doi.org/10.1016/j.placenta.2025.07.083.

CHAPTER 6

AN OXIDATIVE STRESS MODEL OF PLACENTAL INSUFFICIENCY

Oxidative stress at the placenta

Reactive oxygen species (ROS) are highly reactive compounds, capable of inducing instability in lipids, proteins, and nucleic acids [193]. ROS are constantly generated in tissues through normal physiological processes, kept at bay by antioxidants, endogenously produced compounds that neutralize ROS [194]. However, as ROS production outcompetes antioxidant's capacity for scavenging, oxidative stress (OS) can occur [193]. OS of the placenta is a well-established phenomenon [195], significantly increasing in late gestation in pregnancies complicated by diabetes, FGR, and PE [196]. A baseline level of OS occurs in healthy placentas at the periphery of the disc, with more central/uniform OS often observed in the placentae miscarried pregnancies [197]. Placental hypoxia persisting beyond the first trimester has long been considered a probable cause of OS and associated pathologies of placental insufficiency [65]. Accordingly, permanent ligation of arteries supplying the placenta has resulted in APOs in primate pregnancies [41]. However, based on the lesions observed in APOs [198], hypoxia alone seems an insufficient mechanism. Currently, to our knowledge, there is no method to model APOs through oxidative stress that is physiologically compatible with what is observed clinically in cases of placental insufficiency and APO.

Ischemia/reperfusion injury (IRI)

Another common injury that results in high oxidative stress, and mimics many of the biological markers associated with APO, is an ischemia/reperfusion injury (IRI). An IRI occurs when a previously ischemic space is reperfused with oxygen-rich blood, leading to ROS production and damage to the surrounding tissue [199]. In general, an IRI is associated with significant increases in tissue damage and inflammation; paradoxically, this type of injury often results in more damage than ischemia alone [200,201]. Experiments illustrating the effects of an IRI on tissues have been mostly performed in organs common to transplant surgeries such as the heart, kidney, and liver – in addition to organs such as the brain, skeletal muscle, and the intestine [202–204].

In humans, the placenta receives fresh intervillous blood in spurts, approximately every 15 seconds [205] (a similar timeframe to the rhesus macaque [206]). If we assume that intermittent blood flow leads to fluctuations in oxygen tension, the placenta is capable of maintaining healthy function with small, frequent ischemia/reperfusion insults [207]. However, it is unclear how a single, prolonged ischemic episode followed by reperfusion would manifest physiologically in the rhesus placenta. Although placental investigators have long hypothesized a link between IRI and APOs [195,200,207–209], a primate placental IRI has never been demonstrated *in vivo*.

Modeling a placental IRI

There is *ex vivo* evidence that a placental IRI may result in the generation of common APO biomarkers. *In vitro* human placental explant studies have shown that an IRI has the capacity to induce elevated inflammatory profiles [210,211], DAMPs [211], and syncytial/stromal apoptosis [212] in placental villi, as commonly observed in APOs. Additionally, *in vivo* IRI studies have demonstrated the ability of an IRI to induce APOs in the rat model [213–216]. Pathological evidence from IRI placental models *in vivo* is limited, however, increased cytolysis, necrosis, and fibrin deposition have been described in IRI treated placentas [213]. In addition, IRI placental membranes have been reported broken and/or thickened compared to controls, with loss of general architecture and pyknotic nuclei [213].

The syncytiotrophoblast (STB) layer is the major epithelium of the placenta, acting as the primary pathway for nutrient and oxygen exchange. From the limited *in vivo* and *in vitro* work, there is evidence of STB damage as a direct result of IRI [212,213]. If severe enough, STB damage would result in the placental insufficiency pathologies commonly observed [16], and APO for the fetus. To model oxidative stress at the placenta by IRI, we first needed to determine whether the primate placenta is susceptible to an IRI *in vivo*.

To this end, we structed a preliminary time-series experiment, utilizing three pregnant rhesus macaques. We hypothesized that a prolonged cervical ligation would create ischemia at the uterus/placenta, as evidenced by a decreased fetal heart rate, ischemic uterine artery blood metrics, and uterine tissue blanching. We further

hypothesized that ligation relief/blood reperfusion would result in an IRI to the macaque placenta, evidenced by increased 1) pathological injury (syncytial fibrin deposition/necrosis, peri-/inter-villous fibrin deposition, villous architectural breakdown, and inflammatory villous agglutination [Figure 6.1]) and 2) evidence of protein oxidation by immunohistochemical staining of tissue OS marker 3-nitrotyrosine (3-NT).

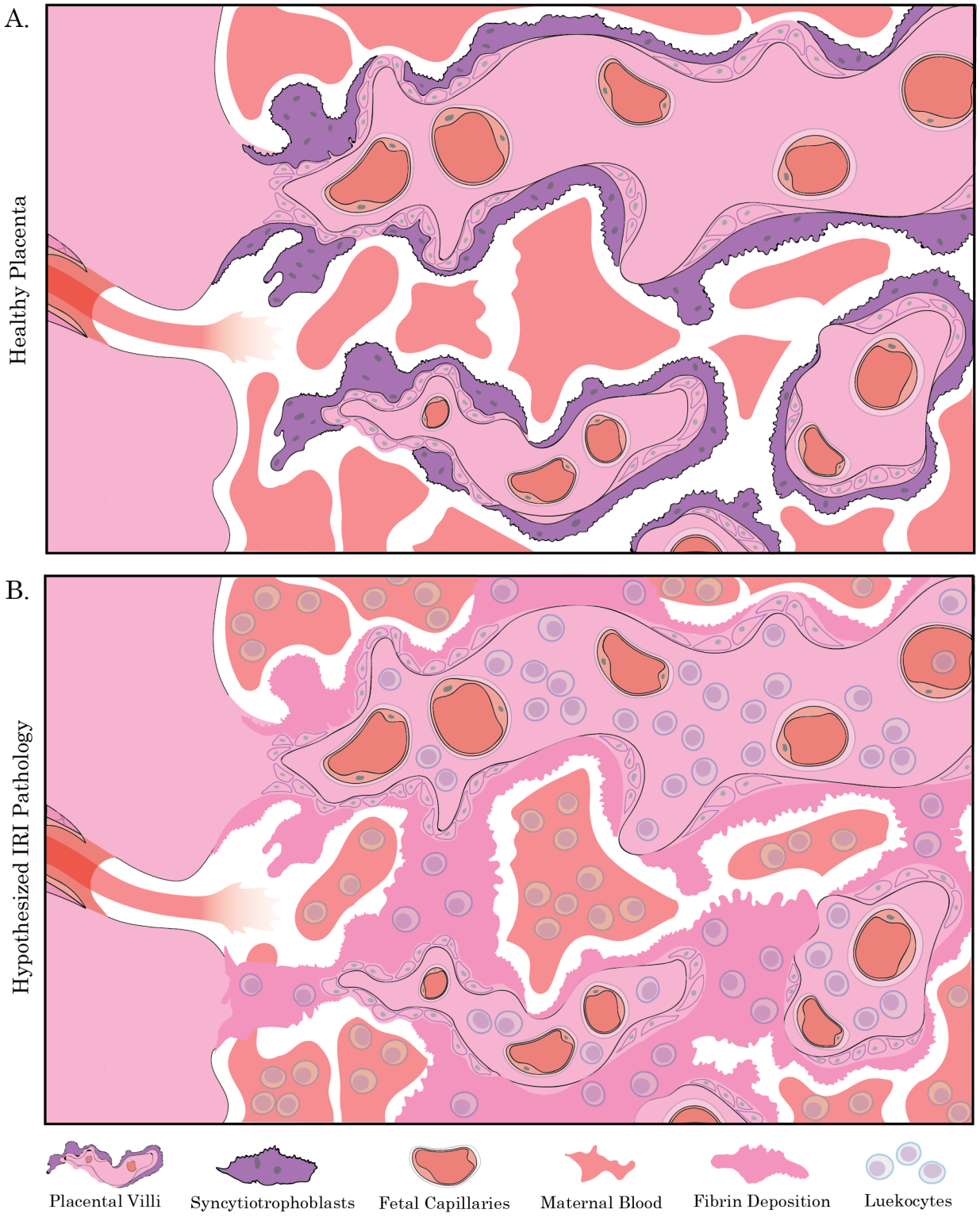

Figure 6.1. A graphical illustration depicting A) a healthy maternal/fetal interface alongside B) hypothesized pathologies occurring in a placental ischemia/reperfusion injury (IRI). Prominent structural and pathological features of the placental labeled below.

METHODS

Ethical use, care, and breeding of macaques

We utilized the macaque as our pregnancy model due to its phylogenetic proximity, long gestational period, and placental physiology similarity to humans [10,34]. All experimental procedures and tissue collections were performed in accordance with the NIH Guide for the Care and Use of Laboratory Animals and under the approval of the University of Wisconsin College of Letters and Sciences and Vice Chancellor Office for Research and Graduate Education Institutional Animal Care and Use Committee, protocol G006209. Wisconsin National Primate Research Center (WNPRC) macaques were housed with compatible mates and monitored for breeding and menstruation. Date of conception was estimated based on initiation of the menstrual cycle, observation of copulation with presence of ejaculate, and ultrasound measurements of fetus and gestational sac.

Cervical ligation and reperfusion

Pregnant rhesus macaques (n=3) underwent abdominal surgery as part of time-series placental IRI experiment at gestational day (GD) ~110. Occlusion of right and left uterine arteries for 1 hour (n=1) and 2 hours (n=1) were performed by a trained veterinary surgeon (Dr. Casey Fitz, Wisconsin National Primate Research Center) by cervical ligation using sterile umbilical tape (SDP INC., SDQ21818SCS). Additionally, a mock ligation control animal (n=1) had sterile umbilical tape place, with no ligation for 2 hours. Ligation relief followed in the 1 hr and 2 hr ligated animals, allowing reperfusion of blood into the uterus. To confirm uterine ischemia,

blood draws were acquired from the uterine artery, downstream from the ligation (just prior to ligation relief) and tested for blood metrics by CG8+ cartridge (Abbott, 03P88-25) using an i-STAT blood analyzer.

Fetal heart rate monitoring and placental collection

Ultrasound monitoring of fetal heart rate (HR) was utilized before, during, and after surgeries, to ensure fetal health and provide evidence of uterine ischemia. A sterile sleeve filled with sterile ultrasound gel containing the ultrasound probe was placed directly on the exposed uterus during control, 1 hr, and 2 hr ligation procedures. Fetal HRs were acquired before surgery, every 5 minutes during ligation, and 1 min, 1 hr, 4 hr, and 24 hr post-ligation. OS damage in the rat placenta, as evidenced by increased COX-2 mRNA, has been shown to peak around 24 hr after IRI, then fall to back to control levels by 48 hr [216]. Considering this, we collected placental tissues by c-section 24 hours post ligation.

Placental histological analyses

Cotyledon center cuts from each individual placental cotyledon were FFPE processed as previously described [30], and subject to the quantitative placental pathological annotation analysis described in Chapter 3. For the purposes of this study, only pathology at the cotyledon level was quantified. As was described in Chapter 4, all histological quantification was reported as a ratio, in relation to total cotyledon pixels (i.e. total feature pixels/total cotyledon pixels), to account for discrepancies in cotyledon sample size.

3-nitrotyrosine immunohistochemical staining

Although it is possible to measure ROS directly, their transient nature presents an inherent challenge in their direct quantification *in vivo* [217]. For example, peroxynitrite, a potent ROS, has a half-life of less than a second [218]. In light of this, downstream biomarkers are often investigated to confirm the presence of increased ROS and OS in tissues [197,217].

Accordingly, we captured total protein oxidation levels at the cotyledon by immunohistochemical staining of 3-nitrotyrosine (3-NT), as has been demonstrated on placental tissues previously [212]. Cotyledon tissue sections were incubated with an anti-3-nitrotyrosine antibody (Abcam, AB110282), alongside a negative control IgG of the same concentration. Staining was developed for 150 s with Betazoid Diaminobenzidine (DAB) chromogen (Biocare Medical, Concord, CA, USA).

Statistical analyses

Differences across control, 1 hr, and 2 hr ligation animal fetal heart rates over ligation/sx the ligation window were determined by paired t test. Placental cotyledon pathology and 3-NT quantification was assessed by Mann-Whitney U test to account for non-normal, zero inflated data.

RESULTS

1 and 2 hr cervical ligation results in uterine ischemia

We began our placental IRI investigation by determining whether cervical ligation successfully resulted in uterine ischemia. To do this, we obtained a blood draw from the uterine artery (downstream of ligation, just before ligation relief) to determine levels of ischemia-associated blood metrics. We were unable to get a reading from the 2 hr ligated animal, as all three blood draws from this artery were too clotted, resulting in iSTAT analysis error. As extended arterial compression can result in blood coagulation during ischemia [219,220], this absence of blood metric data served as evidence of local uterine ischemia in the 2 hr ligation animal.

Uterine artery blood drawn from the 1 hr ligated uterine artery also failed upon first attempt, but was eventually successfully read, demonstrating blood CO_2 and O_2 trends indicative of ischemia (Table 5.1). Ischemia results in the acidification of tissues, leading to diminished ATP production, and eventual Na^+/K^+ pump failure [199]. Altered glucose, pH, and Base Excess metrics demonstrated the diminished nutrients and anerobic respiration/tissue acidosis indicative of ischemia (Table 5.1). Additionally, the potassium (K^+) level spike following Na^+/K^+ pump failure was observed in the 1 hr ligation animal (Table 5.1). Uterine artery blood drawn from the mock ligation control animal did not present difficulty when analyzed and demonstrated good agreement with normal blood metric ranges of the human (Table 5.1). When control metrics were outside of normal range (pO_2 and K), they were in the opposite manner from what we would expect in ischemic tissue [204].

Table 5.1. Assorted blood metric readouts, drawn from uterine artery blood of control and 1 hr dams near the end of ligation or Sx compared to healthy/normal human ranges.

Blood Metric	Human Range	Control	1 hr Ligation
pCO_2	35 – 45 mmHg [221]	36 mmHg	**116.2 mmHg***
pO_2	80 – 105 mmHg [222]	**130 mmHg***	**31 mmHg***
sO_2	95-100% [222]	99%	**28%***
Glucose	30 – 91 mg/dL [221]	46 mg/dL	**<20 mg/dL (LOD)***
pH	7.35 – 7.45 [221]	7.421	**6.922***
Base Excess	(-2) – (+3) mM [221]	-1 mM	**-9 mM***
Na	138-146 mM [222]	144 mM	143
K	3.5-4.9 mM [222]	**3.3 mM***	**6.9 mM***

Bolded text followed by an asterisk "*" denotes metrics outside of normal human range.

Both 1 hr and 2 hr cervical ligations resulted in a dramatic drop off in fetal heart rate (HR), indicative of fetal hypoxemia [223], demonstrating a significant decrease compared to the mock ligation control (Figure 5.2A). The effect of surgery and anesthesia appears to have had a subtle effect on the control animal's fetal HR, showing a slight decrease from baseline from surgery start, until 24 hr post-surgery (Figure 5.2A). Following ligation relief, the 1 hr ligation fetus was quick to recover to their baseline HR, while the 2 hr ligation animal did not recover until the 24 hr post ligation timepoint (Figure 5.2A). When visually assessing the uteri of 1 hr and 2 hr ligation animals, tissue displayed initial darkening, followed by blanching (Figure 5.2B), a common indicator of local ischemia [224]. This blanching appears starker when compared to the mock ligated uterus, which demonstrated a flush, red hue throughout the duration of surgery (Figure 5.2B). Together, the anerobic blood metrics, diminished fetal HRs, and uterine blanching observed in 1 and 2 hr ligated animals provide strong evidence for successful uterine ischemia by cervical ligation.

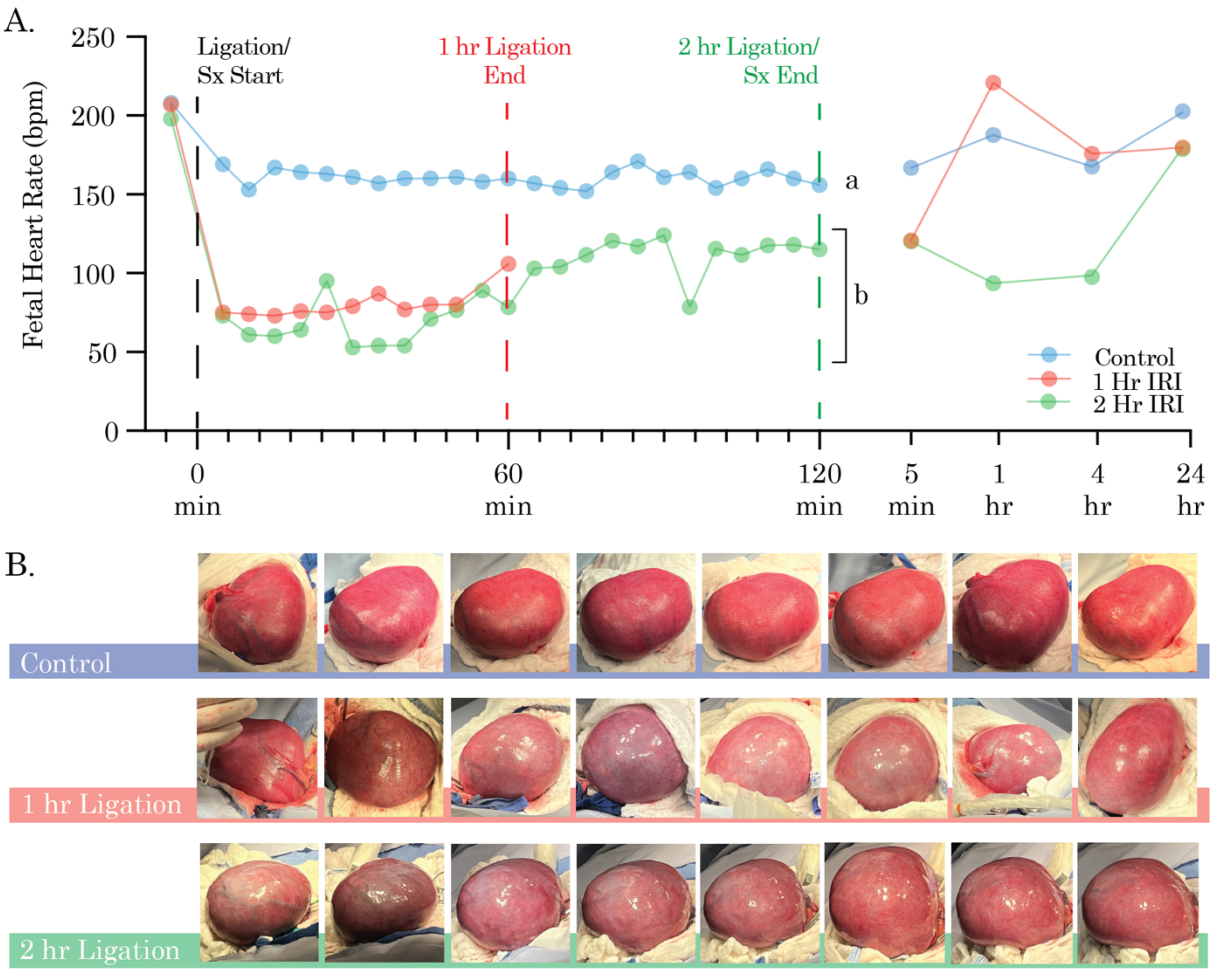

Figure 5.2. A) A graph of fetal heart rate (HR) over surgery (Sx) in control (blue), 1 hr (red), and 2 hr (green) ligation animals. Different letters represent a significant difference in fetal HR across the ligation/Sx window (α=0.05). B) Images taken periodically of control, 1 hr, and 2 hr ligation animals throughout ligation/Sx.

Reperfusion following ligation resulted in increased injury

To assess whether and IRI occurred following uterine reperfusion, maternal peripheral blood was assessed (Figure 5.3). D dimer levels were elevated above the upper limit of detection (LOD) in the 2 hr ligated animal, at 1 hr and 4 hr timepoints following uterine reperfusion, before returning to baseline level at 24 hr post reperfusion (Figure 5.3). As peripheral blood D-dimer levels are indicative of blood

coagulation [225], these data evidence substantial injury in the 2 hr ligation dam following reperfusion. The 1 hr ligated animal demonstrated this same trajectory as the 2 hr dam to a lesser degree, while control D dimer levels gradually elevated following surgery (Figure 5.3). In all three animals, maternal peripheral leukocytes peaked at 4 hr post ligation/Sx, with the 2 hr ligation demonstrating the highest spike (Figure 5.3). The percentage of peripheral lymphocytes in animals of both ligation groups decreased following reperfusion, increasing up the 24 hr post ligation blood draw, while control lymphocytes demonstrated consistent variability (Figure 5.3).

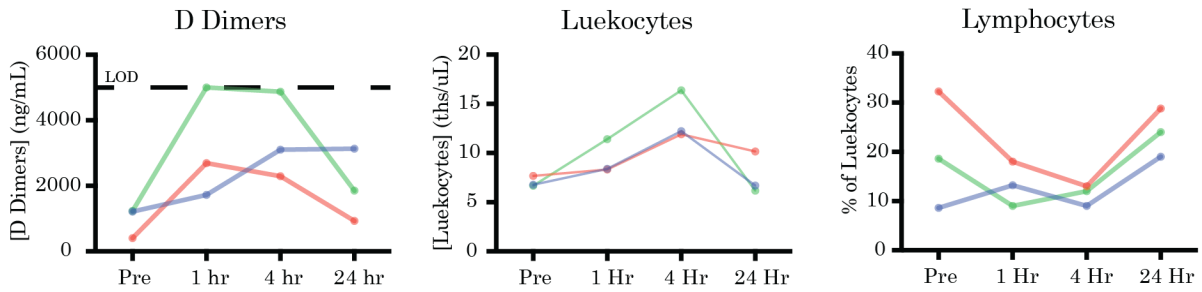

Figure 5.3. A) Graphs displaying peripheral blood D dimers, leukocytes, and lymphocytes of control (blue), 1 hr (red), and 2 hr (green) ligation animals at pre ligation (Pre), 1 hr, 4 hr, and 24 hr post ligation timepoints.

A 2 hr ligation followed by reperfusion resulted in a placental IRI

Next, placental pathology was assessed across rhesus macaque cotyledons, to determine whether ischemia and reperfusion resulted in hypothesized placental pathologies (Figure 5.4). 1 hr of ligation resulted in no differences in cotyledon pathology compared to the control animal (Figure 5.4). The 2 hr ligation animal, however, demonstrated increased inflammatory villous agglutination (INF) and combined pathology (PTH) compared to mock ligation cotyledons (Figure 5.4).

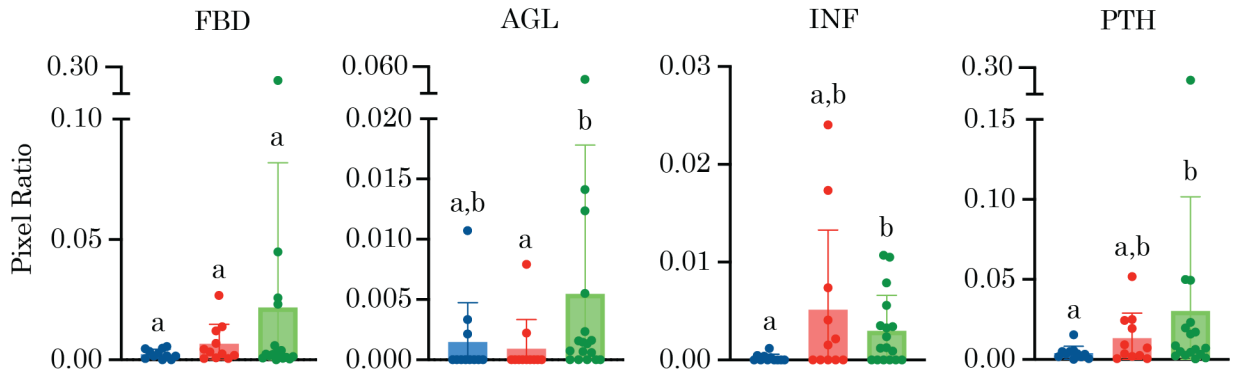

Figure 5.4. Bar graphs displaying fibrin deposition (FBD), villous agglutination (AGL), inflammatory villous agglutination (INF), and total pathology (PTH) in control (blue), 1 hr (red), and 2 hr (green) ligation animals. Data points represent individual cotyledons; bars represent mean and standard deviation. Different letters indicate a statistical difference between animals ($\alpha \leq 0.05$).

Oxidative stress was evidenced immunohistochemically by 3-nitrotyrosine staining (3-NT), a well-established marker of protein oxidation at the placenta [226]. We observed strong, consistent staining across all ligated cotyledons in comparison to control cotyledons (Figure 5.5). Specifically, the villous region of 2 hr ligated cotyledons stained most consistently (Figure 5.5A). Elevated protein oxidation with increasing duration of cervical ligation was further supported by 3-NT quantification, demonstrating significant increases in 3-NT as ligation duration increased (Figure 5.5B).

When qualitatively assessing 2 hr ligation pathologies, we observed great agreement between placental injury and hypothesized placental IRI pathologies (Figure 5.6) One region demonstrated heavy architectural breakdown and leukocytic infiltration by H&E (Figure 5.6A). This injury occurred as hypothesized, centrally

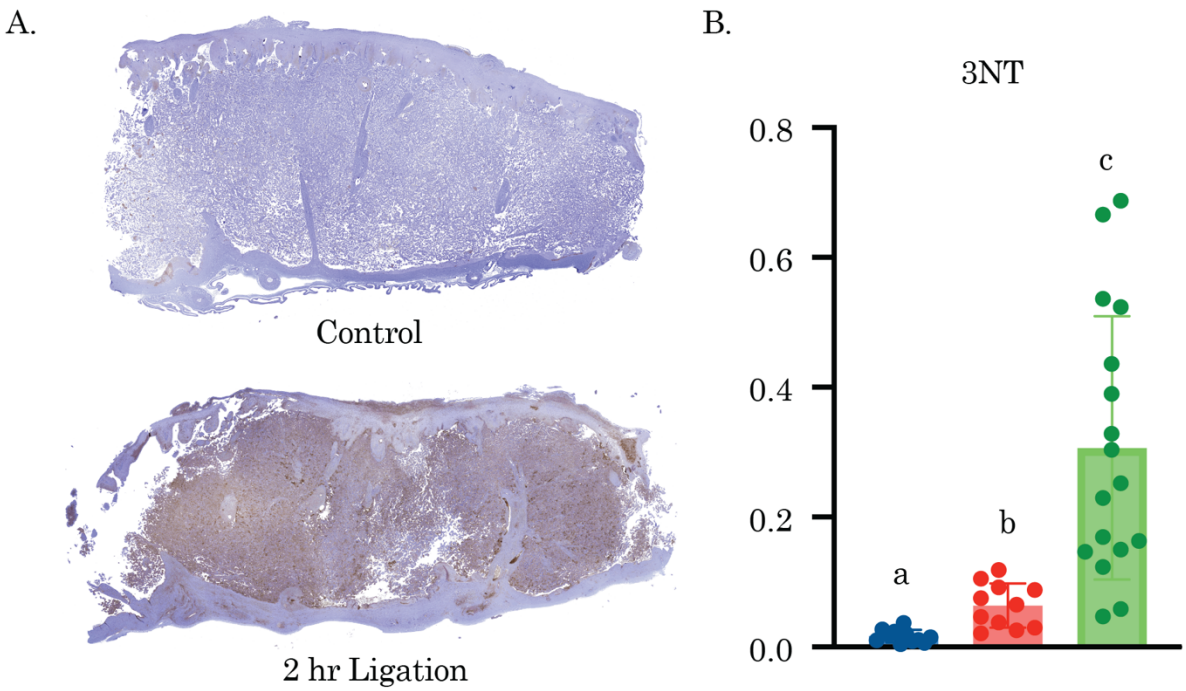

Figure 5.5. Evidence of protein oxidation by 3-nitrotyrosine (3NT) staining. A) Representative images of 3NT-stained control and 2 hr ligated animal cotyledons. B) Quantification of 3NT staining across control (blue), 1 hr (red), and 2 hr (green) ligation animals. Data points represent individual cotyledons; bars represent mean and standard deviation. Different letters indicate a statistical difference between animals ($\alpha \leq 0.05$).

with respect to the placental septa, along the trophoblastic shell/basal plate (Figure 5.6A). Additionally, this region demonstrated heavy 3-NT staining, indicative of severe protein oxidation (Figure 5.6A). At 10x magnification hypothesized attributes of an IRI found in the 2 hr ligated placenta can be more clearly observed and compared with healthy tissue (Figure 5.6B). Healthy villi display good architecture, intact syncytia, diffuse intervillous space red blood cells, and little leukocytic infiltrate (Figure 5.6B). Conversely, the IRI placental villi contained fibrin deposition/ fibrotic syncytia, diminished villous architecture, structured red blood cells, and heavy leukocytic infiltration (Figure 5.6B).

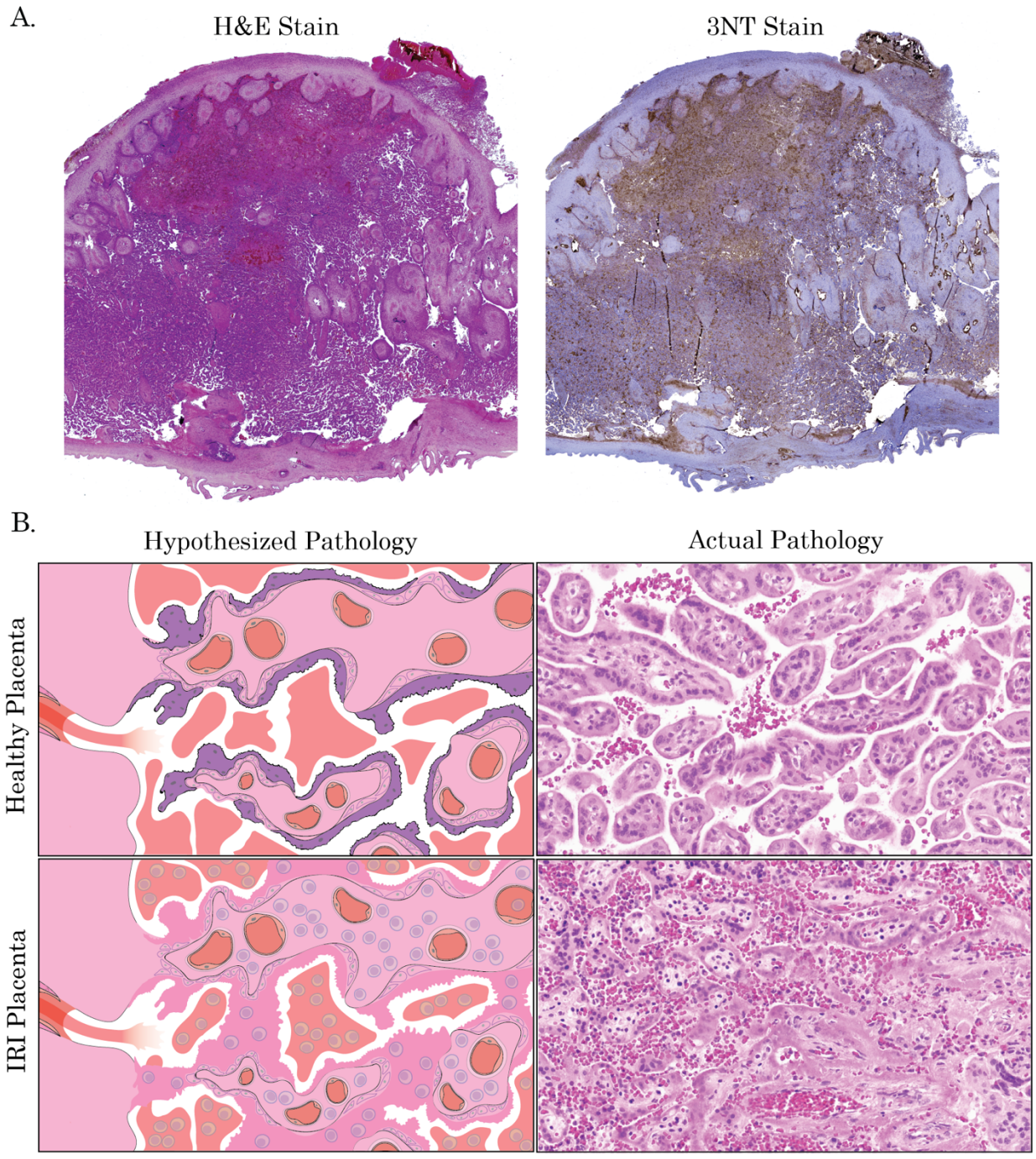

Figure 5.6. Ischemia/reperfusion injury in the macaque placenta. A) H&E- and 3NT-stained images of a 2 hr ligated placental cotyledon demonstrating hypothesized IRI pathologies. B) An image grid comparing hypothesized graphical depictions histopathological features oin healthy and IRI placental tissue (left) next to actual H&E-stained images (right). Enhanced placental villi images taken at 10x magnification.

DISCUSSION

Elevated ROS levels and oxidative stress (OS) markers have been observed in maternal plasma, umbilical cord plasma, and placentae of patients with adverse pregnancy outcomes (APOs) [227–230]. Furthermore, as altered villous growth and structural damage are tightly associated with diminished blood flow, virtually all pathologies of placental insufficiency are linked with oxidative stress at the placenta [17,196]. Despite APOs and OS having long been associated, relatively little work has been done to elucidate their connection [195]. Further, although permanent ligation techniques have been utilized historically to produce APO *in vivo* [41], an IRI represents a more physiologically probable method of inducing OS related injuries. Here, we provide strong evidence that the primate placenta is susceptible to an ischemia/reperfusion injury (IRI) acutely, simultaneously demonstrating many of the hallmarks of placental insufficiency pathologies associated with APOs [198].

The primate placenta is susceptible to an IRI

Fetal heart rate in the macaque has been noted to show minimal variability across gestation *in utero*, with significant decreases observed during uterine contraction [231]. Studies observing diminished fetal heart rate alongside increasing fetal hypoxemia and acidemia (decreasing blood oxygenation and pH levels), has demonstrated a declining fetal heart rate as a functional proxy of fetal distress and ischemia *in utero* [223]. We observed a significantly diminished heart rate, alongside uterine blanching and blood metrics indicative of ischemia, giving us confidence in the utility of cervical ligation to induce uterine ischemia in the rhesus macaque. The

full recovery observed in fetal heart rate and D-dimers 24 hr post reperfusion in the 2 hr ligation animal also provides evidence that a fetus can recover from this transient insult and continue gestation, potentially through full-term.

Increasing the duration of ligation, followed by reperfusion, led to stepwise increases in placental injury across several pathologies investigated. Additionally, the placental injury observed in the 2-hr ligated macaque demonstrated a unique combination of pathological characteristics we hypothesized would occur in an IRI. The widespread immune cell infiltrate outside of and within structurally compromised, agglutinated villi is one such prominent example, uncommon across healthy/normal placentae. This lesion carries pathological attributes blending villous infarct, infarction-hematoma, perivillous fibrin deposition, chronic histiocytic intervillositis (CHIV), and villitis of unknown etiology (VUE) [16]. Furthermore, it had occurred at the basal plate, likely near a spiral artery, supporting its association with MVM pathology [17]. Finally, the ubiquitous 3-NT staining of the villous region in ligated placental cotyledons provides strong evidence that significant OS and IRI had taken place – only increasing in significance as ligation duration was extended.

As transient bouts of placental ischemia have been observed in healthy human [205] and macaque pregnancy [206,232], we know that the primate placenta experiences a degree of ischemia and reperfusion. Further, we know from placental explant studies that the primate placenta is susceptible to an IRI *in vitro* [210,211]. Here, we demonstrated that cervical ligation of the macaque uterus at GD 110 for 2 hr, followed by ligation relief resulted in altered blood metrics, placental pathologies,

and placental protein oxidation indicative of an IRI at 24 hr post reperfusion. As this time-series experiment is a preliminary investigation of low sample size, we cannot draw any definitive conclusions. However, given the strength of the available evidence, we propose that the primate placenta is susceptible to an IRI *in vivo*.

Study limitations and future directions

The most significant limitation to this work is the single animal used for each timepoint. This study was meant to serve as a preliminary investigation, to ensure that an IRI was possible in the rhesus macaque placentae *in vivo*. Future experimentation will include increasing our sample size of rhesus macaques, as well as expanding pathological assessment to the uterine artery for evidence of IRI damage [233]. Additionally, we plan to trial less invasive methodology to induce IRI in the rhesus pregnancy, such as intra-vascular balloon pumps [234]. This would allow less invasive means to induce transient uterine ischemia and allow for multiple insults within a shorter timeframe. Lastly, additional immunohistochemical staining will be used to assess IRI damage at the placenta. Specifically, C4d deposition within the syncytia will be added to the analysis alongside 3-NT staining. C4d highly associated with IRI and is commonly observed chronic placental inflammatory pathologies [235], making it a perfect candidate to assess the degree in which an IRI models placental insufficiency injury.

Additionally, common oxidative stress markers such as 8-oxo-dG (DNA/RNA oxidation) and 4-HNE (lipid oxidation) were omitted from analysis, as their expression was ubiquitous throughout positive control (H_2O_2 incubated) and negative

control (fresh collected) placentae. Crucially, there are observed differences in how long each marker takes to manifest in tissues - with 8-oxo-dG [236] and 4-HNE [237] formation taking minutes to seconds, while 3NT develops over hours to days following oxidative injury [238]. The inherent tissue damage and oxidation associated with placental dissection likely obfuscates varying levels of DNA/RNA and lipid oxidative catabolites, whereas evidence of protein oxidation catabolites take longer to form and would therefore be more indicative of oxidative stresses prior to tissue extraction.

Conclusions on placental IRI

In conclusion, this work makes great headway towards a viable model of OS in the primate pregnancy. We chose to collect tissues at 24 hr post reperfusion, as this is when evidence of injury in the rat model was observed to be greatest [216]. It is likely that evidence of a placental IRI may resolve in the weeks and months leading up to delivery the macaque, however, these changes confirm that an IRI results in the placental pathologies observed in human APOs acutely. A single IRI may not be sufficient to induce APOs and increased quantity and/or frequency of IRIs in rhesus pregnancy may result increasingly pathological outcomes for the fetus at term. As the non-human primate represents the gold-standard for pre-clinical trials [36,37], and OS is a central component of placental disease [195], achieving an IRI APO model in the rhesus macaque would allow for the testing and validation of placental APO therapeutics currently underway [239]. Such therapeutics would work towards relieving the acute and chronic illnesses associated with APOs, improving the lives out countless newborns and families around the globe [1].

CHAPTER 7

CONCLUDING REMARKS AND FUTURE PERSPECTIVES

We set out to better our collective understanding of placental anatomy, physiology, and pathology, with a central aim of to producing a functional model of adverse pregnancy outcomes (APOs) and placental insufficiency in the rhesus macaque. We successfully established novel methodology in which to quantify naturally occurring pathological features of the macaque placenta. Utilizing these methods, we have increased our understanding of primate placental anatomy, physiology, and pathology through categorization of placental cotyledon sub-tissues and pathological features associated with placental insufficiency – such as increased mineralization and inflammatory villous agglutination manifesting with decreased maternal blood flow – pathological characteristics not commonly attributed to maternal malperfusion [15,17]. In addition, through our attempts at modeling placental inflammation we discovered valuable insights concerning the role of chemokines in placental inflammatory lesion manifestation [40]. At the time of this publication, we have yet to successfully produce a model of placental insufficiency in the rhesus macaque *in vivo*. However, our work with transient cervical ligation at midgestation in the rhesus macaque has produced promising evidence that an IRI is possible in the rhesus macaque placenta and produces the pathologies of placental insufficiency acutely. Finally, we were able to confirm the identify of our TSC-derived macaque EVTs, establishing a platform in which to conduct future *in vitro*/*in vivo* crossover studies centered on investigation of placental function and insufficiency.

Characterization of rhesus macaque EVTs *in vitro*

The rhesus macaque is a powerful model of pregnancy – as it uniquely allows for analysis at every gestational age, as well as *in vivo*/*in vitro* crossover, in an organism closely resembling human anatomy and physiology. Specifically, the study of macaque extravillous trophoblasts (EVTs) allows us to investigate a cell type centrally implicated in APO manifestation [11], as EVTs work to remodel maternal spiral arteries and establish the connection between maternal blood flow and fetal tissue [10]. Our investigations on macaque EVTs *in vitro* led to an understanding that macaque TSCs undergo an epithelial-to-mesenchymal transition *en route* to becoming EVTs [30], a trait observed in human EVT differentiation. Additionally, we found NCAM1 to function as a macaque EVT-specific surface marker [30]. This is a significant finding, as multiple macaque trophoblast cell types express Mamu-AG (the human HLA-G homolog found in the rhesus macaque) and therefore cannot be used to discern the EVT cell type. Last, and potentially most significantly here, we observed that differentiating EVTs in low oxygen resulted in a less mature EVT, that also demonstrated diminished proliferative capacity, potentially modeling the less invasive endovascular EVTs observed in placental insufficiency APOs such as preeclampsia [11,46]. Alternatively, this low oxygen EVT cell type may be more phenotypically indicative of the less mature, less motile EVTs of trophoblastic shell, observed to a much greater degree in the macaque placenta [10]. More work will have to be done to assess the similarities and differences between our *in vitro* low oxygen

macaque EVTs and the *in vivo* shallow invasion endovascular EVTs observed in APOs such as preeclampsia.

Challenging current conceptualizations of placental pathological analysis

We set out to develop a quantitative placental pathological analysis to generate numerical data for increased translatability to a research context. Our novel placental pathological feature analysis utilizes digital annotation of common histopathological features, omitting the inherent etiological interpretations involved in current placental pathological analyses [15,16]. It can be effectively argued that there is an inherent loss of resolution associated with our novel approach to quantify pathological features – as we understand basic etiological principles behind how many of pathologies often develop and can approximate their origins with relative confidence. The problem is that historical placental analysis methodology has resulted in limited success in making headway towards understanding the mechanistic underpinnings of placental insufficiency, in large part due to its incompatibility with other forms of biological data. If we are to connect placental pathology to other forms of experimental evidence, it appears we must do so utilizing a more quantitative approach.

We propose that this analysis represents a step forward towards greater placental pathological translatability across research, as well as a more objective way to assess placental injury. We have directly quantified pathological features of the placenta, allowing for direct comparison to additional biological metrics, as well as removing the interpretive elements inherent in current placental pathology clinical

diagnostics [15,16]. We are limited by the small team that has produced the pathological feature criteria thus far – and plan for greater collaborative efforts with placental pathologists moving forward to increase the scope and accuracy of this novel analysis. This is future direction is quite attainable, as this novel methodology is all digitized – ready for review and revision. Importantly, this methodology is unencumbered by the challenges of traditional microscopy, such as limited access to physical slides and a lack of a virtual/physical record of pathology annotation. It is our position that this type of analysis will move the needle forward in the field of placental pathology, by increasing translatability to additional forms of placental, pregnancy, and biological data, decreasing bias/error through review and revision, and enhancing our understanding of placental insufficiency and the mechanisms that drive it.

What is a "normal" placenta?

If we are ever to effectively model the placenta *in vitro*, or produce robust and effective therapeutics, we must first understand the fundamental principles governing placental biology and pathological manifestation. Our novel quantitative placental analysis, alongside dynamic contrast-enhanced MRI methods previously developed in our group [39,48], was used to investigate relationships between biometrics, pathology, and maternal blood perfusion in healthy/normal macaque pregnancies. Through this effort, we established a negative relationship between multiple placental pathologies and maternal blood flow at the cotyledon level for the first time. We also found that stromal mineralization demonstrated significant

negative relationships to maternal blood flow and fetal weight – a correlation previously not tied to altered maternal blood supply, and only effecting fetal weight in severe cases [19]. Additionally, we observed disc-specific relationships regarding mineralization manifestation, evidencing the existence of a distinct compensatory etiology of the lesion. We also provided evidence for a common etiology behind pathological features villous agglutination and inflammatory villous agglutination, supporting those in the field of placental pathology that propose a common etiology for these pathological lesions [17]. Combined, this work helps to classify the baseline pathologies of healthy/normal placentae, as well as highlight several new relationships connecting pregnancy biometrics, placental pathology, and maternal blood perfusion previously unappreciated. Future quantification of pathological features in human placentae would work to illuminate whether the compensatory mineralization pathology is unique to bidiscoid pregnancies or also a component of human monodiscoid pregnancy. Additionally, pathological feature quantification of human placentae would help to elucidate the connection between AGL and INF in humans, supporting or rejecting the notion of a common etiology behind cases co-expressing pathologies such as chronic villitis/VUE and massive perivillous fibrin deposition/maternal floor infarctions.

Modeling placental insufficiency in the rhesus macaque *in vivo*

Two approaches were implemented to develop a rhesus macaque model of placental insufficiency *in vivo*. The first was an intraplacental injection of the potent chemoattractant MCP-1 in attempt to induce inflammatory placental lesions. We

discovered that MCP-1 largely demonstrated the opposite effect - decreasing pathological mineralization in the stroma of placental villi and resulting in comparable maternal blood perfusion and fetal biometrics as observed in unmanipulated pregnancies. In the context of placental insufficiency, these findings suggest potential therapeutic effects of exogenous chemokine administration at the placenta. However, as the dynamics governing inflammatory lesion pathogenesis at the placenta are not well understood [152], it is possible that the addition of MCP-1 to an already pathological placenta may exacerbate injury, instead of mitigate it. A functional model of placental injury must first be produced, to elucidate MCP-1's effects and investigate the potential of it as a therapeutic in disease states of pregnancy.

The second method investigated oxidative stress induction through an ischemia/reperfusion injury (IRI) as a way of modeling placental insufficiency. Utilizing a cervical ligation, we found that 2 hr of uterine artery ligation followed by reperfusion resulted in significant increases in the placental pathology and immunohistochemical staining we had hypothesized, blending several discrete pathological designations associated with APOs [16]. The strength of this method is in its physiological compatibility with the oxidative stress injuries and placental pathologies observed clinically; in contrast to full ligation experimentation at the placenta that has successfully produced APOs [41], but in a manner unobserved in human pregnancy. Currently, it is unknown whether a 2 hr ligation is sufficient to induce APOs in the rhesus macaque, as we collected tissues 24 hours after initial

reperfusion injury. We plan to continue our work on placental IRI – both through assessing acute manifestation pathologically, as well as determining the effect of an IRI on the fetus/dam at full gestation. As it is unclear how susceptible the rhesus macaque is to APOs naturally [38], determining the effect of IRI(s) on the macaque pregnancy at full term will help to elucidate whether or not this type of injury results in classically defined APO biomarkers not commonly observed in the macaque. If successful, this model of oxidative stress-induced placental insufficiency/APO would be a powerful tool for placental physiology and injury investigation, as well as placental therapeutic development.

The future of placental insufficiency and APO study

The placenta is an incredibly dynamic organ, with establishment, growth, and elimination occurring over a relatively short time frame within a genetical dissimilar maternal compartment. In accordance with these facts, altered placental development and/or function appears to be a major factor effecting pregnancies, with a majority of adverse pregnancy outcomes broadly attributed to placental insufficiency [11]. To decrease the frequency of these adverse outcomes, or develop therapeutics to counteract their effects, we must first understand the fundamental forces behind altered placental development and function. The past few decades of research have resulted in a better understanding placental insufficiency and its potential mechanisms [240,241], however, the cause of insufficiency in a majority of these cases still remains a mystery [11]. The work outlined here has resulted in a better understanding of modeling the macaque placenta *in vitro*, defined

relationships connecting fetal outcome, placental pathology, and maternal blood flow, and presented a novel *in vivo* oxidative stress mechanism by which pathologies of placental insufficiency can manifest. Trophoblast stem cell modeling *in vitro* in conjunction with placental insufficiency models *in vivo* has the potential to be a powerful pairing in the pursuit of understanding placental insufficiency etiology and developing APO therapeutics [239].

We aim to continue building on the great work accomplished thus far, to continue exploring knowledge gaps surrounding placental insufficiency/APOs. The translatability of macaque placental pathology-biometric-perfusion relationships to human pregnancy one such example. We plan to conduct pathological feature analysis of human placentae alongside the macaque, to determine the similarity in pathological feature manifestation and relationships. Additionally, we plan to investigate the full-term effects of a placental IRI on rhesus macaque pregnancy. This will illuminate how suitable the model truly is in relation to human APOs. All this effort, and future work, is in pursuit of a enhancing our collecting understanding of placental insufficiency and adverse outcomes in human pregnancy. To the extent we succeed, we contribute to the alleviation of hardship in human pregnancy - improving health outcomes for children, mothers, and families around the globe [1].

REFERENCES

[1] E. Maltepe, S.J. Fisher, Placenta: the forgotten organ, Annu. Rev. Cell Dev. Biol. 31 (2015) 523–552. https://doi.org/10.1146/annurev-cellbio-100814-125620.

[2] D.J. Barker, C. Osmond, Infant mortality, childhood nutrition, and ischaemic heart disease in England and Wales, Lancet Lond. Engl. 1 (1986) 1077–1081. https://doi.org/10.1016/s0140-6736(86)91340-1.

[3] D. Almond, J. Currie, Killing Me Softly: The Fetal Origins Hypothesis, J. Econ. Perspect. J. Am. Econ. Assoc. 25 (2011) 153–172. https://doi.org/10.1257/jep.25.3.153.

[4] P.M. Freaney, K. Harrington, R. Molsberry, A.M. Perak, M.C. Wang, W. Grobman, P. Greenland, N.B. Allen, S. Capewell, M. O'Flaherty, D.M. Lloyd-Jones, S.S. Khan, Temporal Trends in Adverse Pregnancy Outcomes in Birthing Individuals Aged 15 to 44 Years in the United States, 2007 to 2019, J. Am. Heart Assoc. 11 (2022) e025050. https://doi.org/10.1161/JAHA.121.025050.

[5] A. Sadovsky, D.M. Serr, G. Kohn, Composition of the placental septa as shown by nuclear sexing, Science 126 (1957) 609–610. https://doi.org/10.1126/science.126.3274.609.

[6] D. Barker, C. Osmond, S. Grant, K.L. Thornburg, C. Cooper, S. Ring, G. Davey-Smith, Maternal cotyledons at birth predict blood pressure in childhood, Placenta 34 (2013) 672–675. https://doi.org/10.1016/j.placenta.2013.04.019.

[7] N.S. Dellschaft, G. Hutchinson, S. Shah, N.W. Jones, C. Bradley, L. Leach, C. Platt, R. Bowtell, P.A. Gowland, The haemodynamics of the human placenta in utero, PLoS Biol. 18 (2020) e3000676. https://doi.org/10.1371/journal.pbio.3000676.

[8] H. Okada, T. Tsuzuki, H. Murata, Decidualization of the human endometrium, Reprod. Med. Biol. 17 (2018) 220–227. https://doi.org/10.1002/rmb2.12088.

[9] E.D. Albrecht, G.J. Pepe, Regulation of Uterine Spiral Artery Remodeling: a Review, Reprod. Sci. Thousand Oaks Calif 27 (2020) 1932–1942. https://doi.org/10.1007/s43032-020-00212-8.

[10] E.P.C.T. De Rijk, E. Van Esch, The Macaque Placenta—A Mini-Review, Toxicol. Pathol. 36 (2008) 108S-118S. https://doi.org/10.1177/0192623308326095.

[11] J.E. Wardinger, S. Ambati, Placental Insufficiency, in: StatPearls, StatPearls Publishing, Treasure Island (FL), 2024. http://www.ncbi.nlm.nih.gov/books/NBK563171/ (accessed August 28, 2024).

[12] K. Benirschke, G.J. Burton, R.N. Baergen, Pathology of the Human Placenta, Springer Berlin Heidelberg, Berlin, Heidelberg, 2012. https://doi.org/10.1007/978-3-642-23941-0.

[13] L.M. Ernst, Maternal vascular malperfusion of the placental bed, APMIS 126 (2018) 551–560. https://doi.org/10.1111/apm.12833.

[14] Society for Maternal-Fetal Medicine (SMFM). Electronic address: pubs@smfm.org, J.G. Martins, J.R. Biggio, A. Abuhamad, Society for Maternal-Fetal Medicine Consult Series #52: Diagnosis and management of fetal growth restriction: (Replaces Clinical Guideline Number 3, April 2012), Am. J. Obstet. Gynecol. 223 (2020) B2–B17. https://doi.org/10.1016/j.ajog.2020.05.010.

[15] T.Y. Khong, E.E. Mooney, I. Ariel, N.C.M. Balmus, T.K. Boyd, M.-A. Brundler, H. Derricott, M.J. Evans, O.M. Faye-Petersen, J.E. Gillan, A.E.P. Heazell, D.S. Heller, S.M. Jacques, S. Keating, P. Kelehan, A. Maes, E.M. McKay, T.K. Morgan, P.G.J. Nikkels, W.T. Parks, R.W. Redline, I. Scheimberg, M.H. Schoots, N.J. Sebire, A. Timmer, G. Turowski, J.P. van der Voorn, I. van Lijnschoten, S.J. Gordijn, Sampling and Definitions of Placental Lesions: Amsterdam Placental Workshop Group Consensus Statement, Arch. Pathol. Lab. Med. 140 (2016) 698–713. https://doi.org/10.5858/arpa.2015-0225-CC.

[16] R.W. Redline, S. Ravishankar, C.M. Bagby, S.T. Saab, S. Zarei, Four major patterns of placental injury: a stepwise guide for understanding and implementing the 2016 Amsterdam consensus, Mod. Pathol. Off. J. U. S. Can. Acad. Pathol. Inc 34 (2021) 1074–1092. https://doi.org/10.1038/s41379-021-00747-4.

[17] T.Y. Khong, E.E. Mooney, P.G.J. Nikkels, T.K. Morgan, S.J. Gordijn, Pathology of the Placenta: A Practical Guide, Springer, Cham, 2019.

[18] R. Agarwal, A. Tiwari, N. Wadhwa, G. Radhakrishnan, Placental histopathological findings in preterm/term and early/late onset small for gestation age: Are they significant?, Indian J. Pathol. Microbiol. 60 (2017) 232–235. https://doi.org/10.4103/IJPM.IJPM_390_16.

[19] J. Stanek, Segmental villous mineralization: A placental feature of fetal vascular malperfusion, Placenta 86 (2019) 20–27. https://doi.org/10.1016/j.placenta.2019.07.011.

[20] P. Kapur, D. Rakheja, A.M. Gomez, J. Sheffield, P. Sanchez, B.B. Rogers, Characterization of inflammation in syphilitic villitis and in villitis of unknown etiology, Pediatr. Dev. Pathol. Off. J. Soc. Pediatr. Pathol. Paediatr. Pathol. Soc. 7 (2004) 453–458; discussion 421. https://doi.org/10.1007/s10024-004-2124-3.

[21] C.J. Kim, R. Romero, P. Chaemsaithong, J.-S. Kim, Chronic inflammation of the placenta: definition, classification, pathogenesis, and clinical significance, Am. J. Obstet. Gynecol. 213 (2015) S53–S69. https://doi.org/10.1016/j.ajog.2015.08.041.

[22] M.T. Loverro, E. Di Naro, V. Nicolardi, L. Resta, S.A. Mastrolia, F. Schettini, M. Capozza, M. Loverro, G. Loverro, N. Laforgia, Pregnancy Complications, Correlation With Placental Pathology and Neonatal Outcomes, Front. Clin. Diabetes Healthc. 2 (2022). https://doi.org/10.3389/fcdhc.2021.807192.

[23] L.M.M. Nardozza, A.C.R. Caetano, A.C.P. Zamarian, J.B. Mazzola, C.P. Silva, V.M.G. Marçal, T.F. Lobo, A.B. Peixoto, E. Araujo Júnior, Fetal growth restriction: current knowledge, Arch. Gynecol. Obstet. 295 (2017) 1061–1077. https://doi.org/10.1007/s00404-017-4341-9.

[24] B.A. Nowakowska, K. Pankiewicz, U. Nowacka, M. Niemiec, S. Kozłowski, T. Issat, Genetic Background of Fetal Growth Restriction, Int. J. Mol. Sci. 23 (2021) 36. https://doi.org/10.3390/ijms23010036.

[25] I. Brosens, R. Pijnenborg, L. Vercruysse, R. Romero, The "Great Obstetrical Syndromes" are associated with disorders of deep placentation, Am. J. Obstet. Gynecol. 204 (2011) 193–201. https://doi.org/10.1016/j.ajog.2010.08.009.

[26] J.M. Catov, M.F. Muldoon, S.E. Reis, R.B. Ness, L.N. Nguyen, J.-M. Yamal, H. Hwang, W.T. Parks, Preterm birth with placental evidence of malperfusion is associated with cardiovascular risk factors after pregnancy: a prospective cohort study, BJOG Int. J. Obstet. Gynaecol. 125 (2018) 1009–1017. https://doi.org/10.1111/1471-0528.15040.

[27] D. Sharma, S. Shastri, P. Sharma, Intrauterine Growth Restriction: Antenatal and Postnatal Aspects, Clin. Med. Insights Pediatr. 10 (2016) 67–83. https://doi.org/10.4137/CMPed.S40070.

[28] H. Teka, A. Yemane, H.E. Abraha, E. Berhe, H. Tadesse, F. Gebru, M. Yahya, Y. Tadesse, D. Gebre, M. Abrha, B. Tesfay, A. Tekle, T. Gebremariam, B. Amare, M.M. Ebrahim, Y.B. Zelelow, A. Mulugeta, Clinical presentation, maternal-fetal, and neonatal outcomes of early-onset versus late onset preeclampsia-eclampsia syndrome in a teaching hospital in a low-resource setting: A retrospective cohort study, PloS One 18 (2023) e0281952. https://doi.org/10.1371/journal.pone.0281952.

[29] GBD 2021 Fertility and Forecasting Collaborators, Global fertility in 204 countries and territories, 1950-2021, with forecasts to 2100: a comprehensive demographic analysis for the Global Burden of Disease Study 2021, Lancet Lond. Engl. 403 (2024) 2057–2099. https://doi.org/10.1016/S0140-6736(24)00550-6.

[30] L.T. Keding, A.R. Heselton, E. Ren, S.A. Shaw, M.R. Koenig, T.G. Golos, J.K. Schmidt, In vitro differentiation of macaque extravillous trophoblasts in a low oxygen environment, Placenta 163 (2025) 16–28. https://doi.org/10.1016/j.placenta.2025.02.014.

[31] T.A. Nketia, H. Sailem, G. Rohde, R. Machiraju, J. Rittscher, Analysis of live cell images: Methods, tools and opportunities, Methods San Diego Calif 115 (2017) 65–79. https://doi.org/10.1016/j.ymeth.2017.02.007.

[32] L.N. Block, M.T. Aliota, T.C. Friedrich, M.L. Schotzko, K.D. Mean, G.J. Wiepz, T.G. Golos, J.K. Schmidt, Embryotoxic impact of Zika virus in a rhesus macaque in vitro implantation model†, Biol. Reprod. 102 (2020) 806–816. https://doi.org/10.1093/biolre/ioz236.

[33] M. Cherubini, S. Erickson, K. Haase, Modelling the Human Placental Interface In Vitro-A Review, Micromachines 12 (2021) 884. https://doi.org/10.3390/mi12080884.

[34] H.F. Huber, S.L. Jenkins, C. Li, P.W. Nathanielsz, Strength of nonhuman primate studies of developmental programming: review of sample sizes, challenges, and steps for future work, J. Dev. Orig. Health Dis. 11 (2020) 297–306. https://doi.org/10.1017/S2040174419000539.

[35] V.H.J. Roberts, J.N. Castro, B.M. Wessel, D.F. Conrad, A.D. Lewis, J.O. Lo, Rhesus macaque fetal and placental growth demographics: A resource for laboratory animal researchers, Am. J. Primatol. 85 (2023) e23526. https://doi.org/10.1002/ajp.23526.

[36] A.M. Carter, A.C. Enders, R. Pijnenborg, The role of invasive trophoblast in implantation and placentation of primates, Philos. Trans. R. Soc. Lond. B. Biol. Sci. 370 (2015) 20140070. https://doi.org/10.1098/rstb.2014.0070.

[37] R.A. Gibbs, J. Rogers, M.G. Katze, R. Bumgarner, G.M. Weinstock, E.R. Mardis, K.A. Remington, R.L. Strausberg, J.C. Venter, R.K. Wilson, M.A. Batzer, C.D. Bustamante, E.E. Eichler, M.W. Hahn, R.C. Hardison, K.D. Makova, W. Miller, A. Milosavljevic, R.E. Palermo, A. Siepel, J.M. Sikela, T. Attaway, S. Bell, K.E. Bernard, C.J. Buhay, M.N. Chandrabose, M. Dao, C. Davis, K.D. Delehaunty, Y. Ding, H.H. Dinh, S. Dugan-Rocha, L.A. Fulton, R.A. Gabisi, T.T. Garner, J. Godfrey, A.C. Hawes, J. Hernandez, S. Hines, M. Holder, J. Hume, S.N. Jhangiani, V. Joshi, Z.M. Khan, E.F. Kirkness, A. Cree, R.G. Fowler, S. Lee, L.R. Lewis, Z. Li, Y. Liu, S.M. Moore, D. Muzny, L.V. Nazareth, D.N. Ngo, G.O. Okwuonu, G. Pai, D. Parker, H.A. Paul, C. Pfannkoch, C.S. Pohl, Y.-H. Rogers, S.J. Ruiz, A. Sabo, J. Santibanez, B.W. Schneider, S.M. Smith, E. Sodergren, A.F. Svatek, T.R. Utterback, S. Vattathil, W. Warren, C.S. White, A.T. Chinwalla, Y. Feng, A.L. Halpern, L.W. Hillier, X. Huang, P. Minx, J.O. Nelson, K.H. Pepin, X. Qin, G.G. Sutton, E. Venter, B.P. Walenz, J.W. Wallis,

K.C. Worley, S.-P. Yang, S.M. Jones, M.A. Marra, M. Rocchi, J.E. Schein, R. Baertsch, L. Clarke, M. Csürös, J. Glasscock, R.A. Harris, P. Havlak, A.R. Jackson, H. Jiang, Y. Liu, D.N. Messina, Y. Shen, H.X.-Z. Song, T. Wylie, L. Zhang, E. Birney, K. Han, M.K. Konkel, J. Lee, A.F.A. Smit, B. Ullmer, H. Wang, J. Xing, R. Burhans, Z. Cheng, J.E. Karro, J. Ma, B. Raney, X. She, M.J. Cox, J.P. Demuth, L.J. Dumas, S.-G. Han, J. Hopkins, A. Karimpour-Fard, Y.H. Kim, J.R. Pollack, T. Vinar, C. Addo-Quaye, J. Degenhardt, A. Denby, M.J. Hubisz, A. Indap, C. Kosiol, B.T. Lahn, H.A. Lawson, A. Marklein, R. Nielsen, E.J. Vallender, A.G. Clark, B. Ferguson, R.D. Hernandez, K. Hirani, H. Kehrer-Sawatzki, J. Kolb, S. Patil, L.-L. Pu, Y. Ren, D.G. Smith, D.A. Wheeler, I. Schenck, E.V. Ball, R. Chen, D.N. Cooper, B. Giardine, F. Hsu, W.J. Kent, A. Lesk, D.L. Nelson, W.E. O'Brien, K. Prüfer, P.D. Stenson, J.C. Wallace, H. Ke, X.-M. Liu, P. Wang, A.P. Xiang, F. Yang, G.P. Barber, D. Haussler, D. Karolchik, A.D. Kern, R.M. Kuhn, K.E. Smith, A.S. Zwieg, Evolutionary and Biomedical Insights from the Rhesus Macaque Genome, Science 316 (2007) 222–234. https://doi.org/10.1126/science.1139247.

[38] L. Krugner-Higby, M. Luck, D. Hartley, H.M. Crispen, G.R. Lubach, C.L. Coe, High-risk pregnancy in rhesus monkeys (Macaca mulatta): a case of ectopic, abdominal pregnancy with birth of a live, term infant, and a case of gestational diabetes complicated by pre-eclampsia, J. Med. Primatol. 38 (2009) 252–256. https://doi.org/10.1111/j.1600-0684.2009.00349.x.

[39] D.P. Seiter, S.M. Nguyen, T.K. Morgan, L. Mao, D.M. Dudley, D.H. O'connor, M.E. Murphy, K.D. Ludwig, R. Chen, A. Dhyani, A. Zhu, M.L. Schotzko, K.G. Brunner, D.M. Shah, K.M. Johnson, T.G. Golos, O. Wieben, Ferumoxytol dynamic contrast enhanced magnetic resonance imaging identifies altered placental cotyledon perfusion in rhesus macaques†, Biol. Reprod. 107 (2022) 1517–1527. https://doi.org/10.1093/biolre/ioac168.

[40] L.T. Keding, J. Vazquez, R.-Y. Liu, E. Bove, J. Dorobek, H.A. Simmons, K.M. Antony, J.L. Racine, D.M. Shah, O. Wieben, T.G. Golos, A.K. Stanic, Monocyte Chemoattractant Protein-1 (MCP-1) Decreases Mineralization of the Villous Stroma in the Macaque Placenta, Placenta (2025). https://doi.org/10.1016/j.placenta.2025.07.083.

[41] V.H.J. Roberts, J.P. Räsänen, M.J. Novy, A. Frias, S. Louey, T.K. Morgan, K.L. Thornburg, E.R. Spindel, P.L. Grigsby, Restriction of placental vasculature in a non-human primate: A unique model to study placental plasticity, Placenta 33 (2012) 73–76. https://doi.org/10.1016/j.placenta.2011.10.003.

[42] B. Lo, L. Parham, Ethical issues in stem cell research, Endocr. Rev. 30 (2009) 204–213. https://doi.org/10.1210/er.2008-0031.

[43] J.K. Schmidt, L.T. Keding, L.N. Block, G.J. Wiepz, M.R. Koenig, M.G. Meyer, B.M. Dusek, K.M. Kroner, M.J. Bertogliat, A.R. Kallio, K.D. Mean, T.G. Golos, Placenta-derived macaque trophoblast stem cells: differentiation to syncytiotrophoblasts and extravillous trophoblasts reveals phenotypic reprogramming, Sci. Rep. 10 (2020) 19159. https://doi.org/10.1038/s41598-020-76313-w.

[44] L.D.M. Ottosen, J. Hindkaer, M. Husth, D.E. Petersen, J. Kirk, H.J. Ingerslev, Observations on intrauterine oxygen tension measured by fibre-optic microsensors, Reprod. Biomed. Online 13 (2006) 380–385. https://doi.org/10.1016/s1472-6483(10)61443-5.

[45] O. Genbacev, Y. Zhou, J.W. Ludlow, S.J. Fisher, Regulation of human placental development by oxygen tension, Science 277 (1997) 1669–1672. https://doi.org/10.1126/science.277.5332.1669.

[46] Q. Shi, P. Gu, Y. Tang, Q. Ma, Y. Xu, NINJ1 exerts a role in the development of preeclampsia through potential regulation by the Notch1 signaling pathway, J. Obstet. Gynaecol. Res. 51 (2025) e16295. https://doi.org/10.1111/jog.16295.

[47] D. Tiwari, S.S. Choudhury, T. Nath, S. Bose, An investigation into the role of Notch signaling, altered angiogenesis, and inflammatory-induced preterm delivery and related complications in Northeast Indian patients, Placenta 139 (2023) 172–180. https://doi.org/10.1016/j.placenta.2023.07.002.

[48] R. Chen, D. Seiter, L.T. Keding, J. Vazquez, K.M. Antony, H.A. Simmons, P. Basu, A.F. Mejia, K.M. Johnson, A.K. Stanic, R.-Y. Liu, D.M. Shah, T.G. Golos, O. Wieben, Cotyledon-Specific Flow Evaluation of Rhesus Macaque Placental Injury Using Ferumoxytol Dynamic Contrast-Enhanced MRI, J. Magn. Reson. Imaging JMRI 60 (2024) 2196–2204. https://doi.org/10.1002/jmri.29291.

[49] A.C. Enders, T.N. Blankenship, Modification of endometrial arteries during invasion by cytotrophoblast cells in the pregnant macaque, Acta Anat. (Basel) 159 (1997) 169–193. https://doi.org/10.1159/000147983.

[50] S. Kovats, E.K. Main, C. Librach, M. Stubblebine, S.J. Fisher, R. DeMars, A Class I Antigen, HLA-G, Expressed in Human Trophoblasts, Science 248 (1990) 220–223. https://doi.org/10.1126/science.2326636.

[51] I.I. Slukvin, D.P. Lunn, D.I. Watkins, T.G. Golos, Placental expression of the nonclassical MHC class I molecule Mamu-AG at implantation in the rhesus monkey, Proc. Natl. Acad. Sci. U. S. A. 97 (2000) 9104–9109. https://doi.org/10.1073/pnas.97.16.9104.

[52] S.V. Dambaeva, G.I. Bondarenko, R.L. Grendell, R.H. Kravitz, M. Durning, T.G. Golos, Non-classical MHC-E (Mamu-E) expression in the rhesus monkey

placenta, Placenta 29 (2008) 58–70. https://doi.org/10.1016/j.placenta.2007.10.001.

[53] J.K. Schmidt, L.N. Block, T.G. Golos, Defining the rhesus macaque placental miRNAome: Conservation of expression of placental miRNA clusters between the macaque and human, Placenta 65 (2018) 55–64. https://doi.org/10.1016/j.placenta.2018.04.003.

[54] H. Okae, H. Toh, T. Sato, H. Hiura, S. Takahashi, K. Shirane, Y. Kabayama, M. Suyama, H. Sasaki, T. Arima, Derivation of Human Trophoblast Stem Cells, Cell Stem Cell 22 (2018) 50-63.e6. https://doi.org/10.1016/j.stem.2017.11.004.

[55] S. Haider, G. Meinhardt, L. Saleh, V. Kunihs, M. Gamperl, U. Kaindl, A. Ellinger, T.R. Burkard, C. Fiala, J. Pollheimer, S. Mendjan, P.A. Latos, M. Knöfler, Self-Renewing Trophoblast Organoids Recapitulate the Developmental Program of the Early Human Placenta, Stem Cell Rep. 11 (2018) 537–551. https://doi.org/10.1016/j.stemcr.2018.07.004.

[56] M.Y. Turco, L. Gardner, R.G. Kay, R.S. Hamilton, M. Prater, M.S. Hollinshead, A. McWhinnie, L. Esposito, R. Fernando, H. Skelton, F. Reimann, F.M. Gribble, A. Sharkey, S.G.E. Marsh, S. O'Rahilly, M. Hemberger, G.J. Burton, A. Moffett, Trophoblast organoids as a model for maternal–fetal interactions during human placentation, Nature 564 (2018) 263–267. https://doi.org/10.1038/s41586-018-0753-3.

[57] M.T. McMaster, C.L. Librach, Y. Zhou, K.H. Lim, M.J. Janatpour, R. DeMars, S. Kovats, C. Damsky, S.J. Fisher, Human placental HLA-G expression is restricted to differentiated cytotrophoblasts, J. Immunol. Baltim. Md 1950 154 (1995) 3771–3778.

[58] A. Arutyunyan, K. Roberts, K. Troulé, F.C.K. Wong, M.A. Sheridan, I. Kats, L. Garcia-Alonso, B. Velten, R. Hoo, E.R. Ruiz-Morales, C. Sancho-Serra, J. Shilts, L.-F. Handfield, L. Marconato, E. Tuck, L. Gardner, C.I. Mazzeo, Q. Li, I. Kelava, G.J. Wright, E. Prigmore, S.A. Teichmann, O.A. Bayraktar, A. Moffett, O. Stegle, M.Y. Turco, R. Vento-Tormo, Spatial multiomics map of trophoblast development in early pregnancy, Nature 616 (2023) 143–151. https://doi.org/10.1038/s41586-023-05869-0.

[59] Z. Liu, M. Zhai, Q. Zhang, T. Yang, Z. Wan, J. Li, X. Liu, B. Xu, L. Du, R.W.S. Chan, L. Zhang, W.S.B. Yeung, K.W. Cheung, P.C.N. Chiu, W.-J. Wang, C.-L. Lee, Y. Gao, Resolving the gene expression maps of human first-trimester chorionic villi with spatial transcriptome, Front. Cell Dev. Biol. 10 (2022) 1060298. https://doi.org/10.3389/fcell.2022.1060298.

[60] H. Suryawanshi, K. Max, K.A. Bogardus, A. Sopeyin, M.S. Chang, P. Morozov, P.M. Castano, T. Tuschl, Z. Williams, Dynamic genome-wide gene

expression and immune cell composition in the developing human placenta, J. Reprod. Immunol. 151 (2022) 103624. https://doi.org/10.1016/j.jri.2022.103624.

[61] S. Greenbaum, I. Averbukh, E. Soon, G. Rizzuto, A. Baranski, N.F. Greenwald, A. Kagel, M. Bosse, E.G. Jaswa, Z. Khair, S. Kwok, S. Warshawsky, H. Piyadasa, M. Goldston, A. Spence, G. Miller, M. Schwartz, W. Graf, D. Van Valen, V.D. Winn, T. Hollmann, L. Keren, M. van de Rijn, M. Angelo, A spatially resolved timeline of the human maternal-fetal interface, Nature 619 (2023) 595–605. https://doi.org/10.1038/s41586-023-06298-9.

[62] X. Jiang, J. Zhai, Z. Xiao, X. Wu, D. Zhang, H. Wan, Y. Xu, L. Qi, M. Wang, D. Yu, Y. Liu, H. Wu, R. Sun, S. Xia, K. Yu, J. Guo, H. Wang, Identifying a dynamic transcriptomic landscape of the cynomolgus macaque placenta during pregnancy at single-cell resolution, Dev. Cell 58 (2023) 806-821.e7. https://doi.org/10.1016/j.devcel.2023.03.012.

[63] M.N. Shahbazi, A. Jedrusik, S. Vuoristo, G. Recher, A. Hupalowska, V. Bolton, N.N.M. Fogarty, A. Campbell, L. Devito, D. Ilic, Y. Khalaf, K.K. Niakan, S. Fishel, M. Zernicka-Goetz, Self-organization of the human embryo in the absence of maternal tissues, Nat. Cell Biol. 18 (2016) 700–708. https://doi.org/10.1038/ncb3347.

[64] A.K. Wakeland, F. Soncin, M. Moretto-Zita, C.-W. Chang, M. Horii, D. Pizzo, K.K. Nelson, L.C. Laurent, M.M. Parast, Hypoxia Directs Human Extravillous Trophoblast Differentiation in a Hypoxia-Inducible Factor–Dependent Manner, Am. J. Pathol. 187 (2017) 767–780. https://doi.org/10.1016/j.ajpath.2016.11.018.

[65] J.D. Aplin, Hypoxia and human placental development, J. Clin. Invest. 105 (2000) 559–560. https://doi.org/10.1172/JCI9512.

[66] O. Genbacev, R. Joslin, C.H. Damsky, B.M. Polliotti, S.J. Fisher, Hypoxia alters early gestation human cytotrophoblast differentiation/invasion in vitro and models the placental defects that occur in preeclampsia, J. Clin. Invest. 97 (1996) 540–550. https://doi.org/10.1172/JCI118447.

[67] M. Horii, Y. Li, A.K. Wakeland, D.P. Pizzo, K.K. Nelson, K. Sabatini, L.C. Laurent, Y. Liu, M.M. Parast, Human pluripotent stem cells as a model of trophoblast differentiation in both normal development and disease, Proc. Natl. Acad. Sci. 113 (2016). https://doi.org/10.1073/pnas.1604747113.

[68] C.-W. Chang, A.K. Wakeland, M.M. Parast, Trophoblast lineage specification, differentiation and their regulation by oxygen tension, J. Endocrinol. 236 (2018) R43–R56. https://doi.org/10.1530/JOE-17-0402.

[69] F. Rodesch, P. Simon, C. Donner, E. Jauniaux, Oxygen measurements in endometrial and trophoblastic tissues during early pregnancy, Obstet. Gynecol. 80 (1992) 283–285.

[70] E. Jauniaux, A.L. Watson, J. Hempstock, Y.P. Bao, J.N. Skepper, G.J. Burton, Onset of maternal arterial blood flow and placental oxidative stress. A possible factor in human early pregnancy failure, Am. J. Pathol. 157 (2000) 2111–2122. https://doi.org/10.1016/S0002-9440(10)64849-3.

[71] B. Fischer, B.D. Bavister, Oxygen tension in the oviduct and uterus of rhesus monkeys, hamsters and rabbits, J. Reprod. Fertil. 99 (1993) 673–679. https://doi.org/10.1530/jrf.0.0990673.

[72] A.E. Rozner, M. Durning, J. Kropp, G.J. Wiepz, T.G. Golos, Macrophages modulate the growth and differentiation of rhesus monkey embryonic trophoblasts, Am. J. Reprod. Immunol. N. Y. N 1989 76 (2016) 364–375. https://doi.org/10.1111/aji.12564.

[73] K.J. Livak, T.D. Schmittgen, Analysis of relative gene expression data using real-time quantitative PCR and the 2(-Delta Delta C(T)) Method, Methods San Diego Calif 25 (2001) 402–408. https://doi.org/10.1006/meth.2001.1262.

[74] M.R. Koenig, A.M. Mitzey, T.K. Morgan, X. Zeng, H.A. Simmons, A. Mejia, F. Leyva Jaimes, L.T. Keding, C.M. Crooks, A.M. Weiler, E.K. Bohm, M.T. Aliota, T.C. Friedrich, E.L. Mohr, T.G. Golos, Infection of the maternal-fetal interface and vertical transmission following low-dose inoculation of pregnant rhesus macaques (Macaca mulatta) with an African-lineage Zika virus, PLOS ONE 18 (2023) e0284964. https://doi.org/10.1371/journal.pone.0284964.

[75] A.F. Tarantal, A.G. Hendrickx, Prenatal growth in the cynomolgus and rhesus macaque (Macaca fascicularis and Macaca mulatta): A comparison by ultrasonography, Am. J. Primatol. 15 (1988) 309–323. https://doi.org/10.1002/ajp.1350150405.

[76] T.E. Ziegler, R.L. Matteri, F.H. Wegner, Detection of urinary gonadotropins in callitrichid monkeys with a sensitive immunoassay based upan a unique monoclonal antibody, Am. J. Primatol. 31 (1993) 181–188. https://doi.org/10.1002/ajp.1350310303.

[77] D.H. Abbott, S.H. Vepraskas, T.H. Horton, E. Terasawa, J.E. Levine, Accelerated Episodic Luteinizing Hormone Release Accompanies Blunted Progesterone Regulation in PCOS-like Female Rhesus Monkeys (Macaca Mulatta) Exposed to Testosterone during Early-to-Mid Gestation, Neuroendocrinology 107 (2018) 133–146. https://doi.org/10.1159/000490570.

[78] K.M. Varberg, E.M. Dominguez, B. Koseva, J.M. Varberg, R.P. McNally, A. Moreno-Irusta, E.R. Wesley, K. Iqbal, W.A. Cheung, C. Schwendinger-Schreck, C. Smail, H. Okae, T. Arima, M. Lydic, K. Holoch, C. Marsh, M.J. Soares, E. Grundberg, Extravillous trophoblast cell lineage development is associated with active remodeling of the chromatin landscape, Nat. Commun. 14 (2023) 4826. https://doi.org/10.1038/s41467-023-40424-5.

[79] I. Caniggia, H. Mostachfi, J. Winter, M. Gassmann, S.J. Lye, M. Kuliszewski, M. Post, Hypoxia-inducible factor-1 mediates the biological effects of oxygen on human trophoblast differentiation through TGFbeta(3), J. Clin. Invest. 105 (2000) 577–587. https://doi.org/10.1172/JCI8316.

[80] S.A. Patel, M.C. Simon, Biology of hypoxia-inducible factor-2alpha in development and disease, Cell Death Differ. 15 (2008) 628–634. https://doi.org/10.1038/cdd.2008.17.

[81] N. Yu, J.-L. Wu, J. Xiao, L. Fan, S.-H. Chen, W. Li, HIF-1α regulates angiogenesis via Notch1/STAT3/ETBR pathway in trophoblastic cells, Cell Cycle Georget. Tex 18 (2019) 3502–3512. https://doi.org/10.1080/15384101.2019.1689481.

[82] S. Ikeda, A. Kitadate, F. Abe, N. Takahashi, H. Tagawa, Hypoxia-inducible KDM3A addiction in multiple myeloma, Blood Adv. 2 (2018) 323–334. https://doi.org/10.1182/bloodadvances.2017008847.

[83] D. Chakraborty, W. Cui, G.X. Rosario, R.L. Scott, P. Dhakal, S.J. Renaud, M. Tachibana, M.A.K. Rumi, C.W. Mason, A.J. Krieg, M.J. Soares, HIF-KDM3A-MMP12 regulatory circuit ensures trophoblast plasticity and placental adaptations to hypoxia, Proc. Natl. Acad. Sci. U. S. A. 113 (2016) E7212–E7221. https://doi.org/10.1073/pnas.1612626113.

[84] E.S. Meade, Y.Y. Ma, S. Guller, Role of hypoxia-inducible transcription factors 1alpha and 2alpha in the regulation of plasminogen activator inhibitor-1 expression in a human trophoblast cell line, Placenta 28 (2007) 1012–1019. https://doi.org/10.1016/j.placenta.2007.04.005.

[85] Y. Ye, A. Vattai, X. Zhang, J. Zhu, C.J. Thaler, S. Mahner, U. Jeschke, V. von Schönfeldt, Role of Plasminogen Activator Inhibitor Type 1 in Pathologies of Female Reproductive Diseases, Int. J. Mol. Sci. 18 (2017) 1651. https://doi.org/10.3390/ijms18081651.

[86] R.-P. Czekay, D.J. Loskutoff, Unexpected role of plasminogen activator inhibitor 1 in cell adhesion and detachment, Exp. Biol. Med. Maywood NJ 229 (2004) 1090–1096. https://doi.org/10.1177/153537020422901102.

[87] J. E Davies, J. Pollheimer, H.E.J. Yong, M.I. Kokkinos, B. Kalionis, M. Knöfler, P. Murthi, Epithelial-mesenchymal transition during extravillous trophoblast differentiation, Cell Adhes. Migr. 10 (2016) 310–321. https://doi.org/10.1080/19336918.2016.1170258.

[88] D.M. Gonzalez, D. Medici, Signaling mechanisms of the epithelial-mesenchymal transition, Sci. Signal. 7 (2014) re8. https://doi.org/10.1126/scisignal.2005189.

[89] M.A. Sheridan, X. Zhao, R.C. Fernando, L. Gardner, V. Perez-Garcia, Q. Li, S.G.E. Marsh, R. Hamilton, A. Moffett, M.Y. Turco, Characterization of primary models of human trophoblast, Dev. Camb. Engl. 148 (2021) dev199749. https://doi.org/10.1242/dev.199749.

[90] K.M. Varberg, K. Iqbal, M. Muto, M.E. Simon, R.L. Scott, K. Kozai, R.H. Choudhury, J.D. Aplin, R. Biswell, M. Gibson, H. Okae, T. Arima, J.L. Vivian, E. Grundberg, M.J. Soares, ASCL2 reciprocally controls key trophoblast lineage decisions during hemochorial placenta development, Proc. Natl. Acad. Sci. 118 (2021) e2016517118. https://doi.org/10.1073/pnas.2016517118.

[91] C.H. Damsky, C. Librach, K.H. Lim, M.L. Fitzgerald, M.T. McMaster, M. Janatpour, Y. Zhou, S.K. Logan, S.J. Fisher, Integrin switching regulates normal trophoblast invasion, Dev. Camb. Engl. 120 (1994) 3657–3666. https://doi.org/10.1242/dev.120.12.3657.

[92] B. Dietrich, S. Haider, G. Meinhardt, J. Pollheimer, M. Knöfler, WNT and NOTCH signaling in human trophoblast development and differentiation, Cell. Mol. Life Sci. CMLS 79 (2022) 292. https://doi.org/10.1007/s00018-022-04285-3.

[93] A.C. Enders, T.N. Blankenship, Interstitial trophoblast cells: An enigmatic and variable component of the developing macaque placenta, Placenta 33 (2012) 672–676. https://doi.org/10.1016/j.placenta.2012.06.003.

[94] C.Q.E. Lee, M.Y. Turco, L. Gardner, B.D. Simons, M. Hemberger, A. Moffett, Integrin α2 marks a niche of trophoblast progenitor cells in first trimester human placenta, Dev. Camb. Engl. 145 (2018) dev162305. https://doi.org/10.1242/dev.162305.

[95] S. Haider, G. Meinhardt, L. Saleh, C. Fiala, J. Pollheimer, M. Knöfler, Notch1 controls development of the extravillous trophoblast lineage in the human placenta, Proc. Natl. Acad. Sci. 113 (2016). https://doi.org/10.1073/pnas.1612335113.

[96] K. Plessl, S. Haider, C. Fiala, J. Pollheimer, M. Knöfler, Expression pattern and function of Notch2 in different subtypes of first trimester cytotrophoblast, Placenta 36 (2015) 365–371. https://doi.org/10.1016/j.placenta.2015.01.009.

[97] C.Q.E. Lee, L. Gardner, M. Turco, N. Zhao, M.J. Murray, N. Coleman, J. Rossant, M. Hemberger, A. Moffett, What Is Trophoblast? A Combination of Criteria Define Human First-Trimester Trophoblast, Stem Cell Rep. 6 (2016) 257–272. https://doi.org/10.1016/j.stemcr.2016.01.006.

[98] S. Usman, N.H. Waseem, T.K.N. Nguyen, S. Mohsin, A. Jamal, M.-T. Teh, A. Waseem, Vimentin Is at the Heart of Epithelial Mesenchymal Transition (EMT) Mediated Metastasis, Cancers 13 (2021) 4985. https://doi.org/10.3390/cancers13194985.

[99] J. Gerdes, U. Schwab, H. Lemke, H. Stein, Production of a mouse monoclonal antibody reactive with a human nuclear antigen associated with cell proliferation, Int. J. Cancer 31 (1983) 13–20. https://doi.org/10.1002/ijc.2910310104.

[100] T.D. Burrows, A. King, Y.W. Loke, Expression of adhesion molecules by endovascular trophoblast and decidual endothelial cells: implications for vascular invasion during implantation, Placenta 15 (1994) 21–33. https://doi.org/10.1016/s0143-4004(05)80233-4.

[101] T.N. Blankenship, B.F. King, Macaque intra-arterial trophoblast and extravillous trophoblast of the cell columns and cytotrophoblastic shell express neural cell adhesion molecule (NCAM), Anat. Rec. 245 (1996) 525–531. https://doi.org/10.1002/(SICI)1097-0185(199607)245:3<525::AID-AR9>3.0.CO;2-Q.

[102] I.I. Slukvin, J.E. Boyson, D.I. Watkins, T.G. Golos, The Rhesus Monkey Analogue of Human Lymphocyte Antigen-G Is Expressed Primarily in Villous Syncytiotrophoblasts1, Biol. Reprod. 58 (1998) 728–738. https://doi.org/10.1095/biolreprod58.3.728.

[103] L.K. Harris, C.J.P. Jones, J.D. Aplin, Adhesion Molecules in Human Trophoblast – A Review. II. Extravillous Trophoblast, Placenta 30 (2009) 299–304. https://doi.org/10.1016/j.placenta.2008.12.003.

[104] M.J. Wolfgang, S.G. Eisele, L. Knowles, M.A. Browne, M.L. Schotzko, T.G. Golos, Pregnancy and live birth from nonsurgical transfer of *in vivo* - and *in vitro* -produced blastocysts in the rhesus monkey, J. Med. Primatol. 30 (2001) 148–155. https://doi.org/10.1111/j.1600-0684.2001.tb00003.x.

[105] J.C. Robins, A. Heizer, A. Hardiman, M. Hubert, S. Handwerger, Oxygen Tension Directs the Differentiation Pathway of Human Cytotrophoblast Cells, Placenta 28 (2007) 1141–1146. https://doi.org/10.1016/j.placenta.2007.05.006.

[106] L. Zhang, G. Huang, X. Li, Y. Zhang, Y. Jiang, J. Shen, J. Liu, Q. Wang, J. Zhu, X. Feng, J. Dong, C. Qian, Hypoxia induces epithelial-mesenchymal

transition via activation of SNAI1 by hypoxia-inducible factor -1α in hepatocellular carcinoma, BMC Cancer 13 (2013) 108. https://doi.org/10.1186/1471-2407-13-108.

[107] E. Arimoto-Ishida, M. Sakata, K. Sawada, M. Nakayama, F. Nishimoto, S. Mabuchi, T. Takeda, T. Yamamoto, A. Isobe, Y. Okamoto, E. Lengyel, N. Suehara, K.-I. Morishige, T. Kimura, Up-regulation of alpha5-integrin by E-cadherin loss in hypoxia and its key role in the migration of extravillous trophoblast cells during early implantation, Endocrinology 150 (2009) 4306–4315. https://doi.org/10.1210/en.2008-1662.

[108] R.E. Albers, M.R. Kaufman, B.V. Natale, C. Keoni, K. Kulkarni-Datar, S. Min, C.R. Williams, D.R.C. Natale, T.L. Brown, Trophoblast-Specific Expression of Hif-1α Results in Preeclampsia-Like Symptoms and Fetal Growth Restriction, Sci. Rep. 9 (2019) 2742. https://doi.org/10.1038/s41598-019-39426-5.

[109] N.M. Hunkapiller, M. Gasperowicz, M. Kapidzic, V. Plaks, E. Maltepe, J. Kitajewski, J.C. Cross, S.J. Fisher, A role for Notch signaling in trophoblast endovascular invasion and in the pathogenesis of pre-eclampsia, Dev. Camb. Engl. 138 (2011) 2987–2998. https://doi.org/10.1242/dev.066589.

[110] W.-X. Zhao, X. Zhuang, T.-T. Huang, R. Feng, J.-H. Lin, Effects of Notch2 and Notch3 on Cell Proliferation and Apoptosis of Trophoblast Cell Lines, Int. J. Med. Sci. 12 (2015) 867–874. https://doi.org/10.7150/ijms.12935.

[111] T.G. Golos, G.I. Bondarenko, S.V. Dambaeva, E.E. Breburda, M. Durning, On the role of placental Major Histocompatibility Complex and decidual leukocytes in implantation and pregnancy success using non-human primate models, Int. J. Dev. Biol. 54 (2010) 431–443. https://doi.org/10.1387/ijdb.082797tg.

[112] G.D. Hodgen, W.W. Tullner, J.L. Vaitukaitis, D.N. Ward, G.T. Ross, Specific Radioimmunoassay of Chorionic Gonadotropin During Implantation in Rhesus Monkeys, J. Clin. Endocrinol. Metab. 39 (1974) 457–464. https://doi.org/10.1210/jcem-39-3-457.

[113] J.A. Wilken, K. Matsumoto, L.S. Laughlin, B.L. Lasley, E. Bedows, Comparison of chorionic gonadotropin expression in human and macaque (*Macaca fascicularis*) trophoblasts, Am. J. Primatol. 56 (2002) 89–97. https://doi.org/10.1002/ajp.1066.

[114] K. Handschuh, J. Guibourdenche, V. Tsatsaris, M. Guesnon, I. Laurendeau, D. Evain-Brion, T. Fournier, Human Chorionic Gonadotropin Expression in Human Trophoblasts from Early Placenta: Comparative Study Between Villous and Extravillous Trophoblastic Cells, Placenta 28 (2007) 175–184. https://doi.org/10.1016/j.placenta.2006.01.019.

[115] Y. Liu, X. Fan, R. Wang, X. Lu, Y.-L. Dang, H. Wang, H.-Y. Lin, C. Zhu, H. Ge, J.C. Cross, H. Wang, Single-cell RNA-seq reveals the diversity of trophoblast subtypes and patterns of differentiation in the human placenta, Cell Res. 28 (2018) 819–832. https://doi.org/10.1038/s41422-018-0066-y.

[116] C.-C.J. Sun, V.O. Revell, A.J. Belli, R.M. Viscardi, Discrepancy in pathologic diagnosis of placental lesions, Arch. Pathol. Lab. Med. 126 (2002) 706–709. https://doi.org/10.5858/2002-126-0706-DIPDOP.

[117] I. Ptacek, N.J. Sebire, J.A. Man, P. Brownbill, A.E.P. Heazell, Systematic review of placental pathology reported in association with stillbirth, Placenta 35 (2014) 552–562. https://doi.org/10.1016/j.placenta.2014.05.011.

[118] E. Dubruc, F. Lebreton, C. Giannoli, M. Rabilloud, C. Huissoud, M. Devouassoux-Shisheboran, F. Allias, Placental histological lesions in fetal and neonatal alloimmune thrombocytopenia: A retrospective cohort study of 21 cases, Placenta 48 (2016) 104–109. https://doi.org/10.1016/j.placenta.2016.10.009.

[119] O.M. Faye-Petersen, L.M. Ernst, Maternal Floor Infarction and Massive Perivillous Fibrin Deposition, Surg. Pathol. Clin. 6 (2013) 101–114. https://doi.org/10.1016/j.path.2012.10.002.

[120] R. Lee, D. Adlam, C.A. Clelland, K.M. Channon, Lines of Zahn in coronary artery thrombus, Eur. Heart J. 33 (2012) 1039. https://doi.org/10.1093/eurheartj/ehs028.

[121] D.M. Nelson, E.C. Crouch, E.M. Curran, D.R. Farmer, Trophoblast interaction with fibrin matrix. Epithelialization of perivillous fibrin deposits as a mechanism for villous repair in the human placenta, Am. J. Pathol. 136 (1990) 855–865.

[122] T.E. Bunton, Incidental lesions in nonhuman primate placentae, Vet. Pathol. 23 (1986) 431–438. https://doi.org/10.1177/030098588602300413.

[123] H. Fox, N. Sebire, Pathology of the Placenta, 3rd Edition, Saunders Elsevier, 2007.

[124] V.V. Joshi, D.S. Heller, O.M. Faye-Petersen, Handbook of Placental Pathology, Informa Healthcare, London, 2005.

[125] N.M.E. Fogarty, A.C. Ferguson-Smith, G.J. Burton, Syncytial knots (Tenney-Parker changes) in the human placenta: evidence of loss of transcriptional activity and oxidative damage, Am. J. Pathol. 183 (2013) 144–152. https://doi.org/10.1016/j.ajpath.2013.03.016.

[126] S. Mukhopadhyay, M.D. Feldman, E. Abels, R. Ashfaq, S. Beltaifa, N.G. Cacciabeve, H.P. Cathro, L. Cheng, K. Cooper, G.E. Dickey, R.M. Gill, R.P. Heaton, R. Kerstens, G.M. Lindberg, R.K. Malhotra, J.W. Mandell, E.D. Manlucu, A.M. Mills, S.E. Mills, C.A. Moskaluk, M. Nelis, D.T. Patil, C.G. Przybycin, J.P. Reynolds, B.P. Rubin, M.H. Saboorian, M. Salicru, M.A. Samols, C.D. Sturgis, K.O. Turner, M.R. Wick, J.Y. Yoon, P. Zhao, C.R. Taylor, Whole Slide Imaging Versus Microscopy for Primary Diagnosis in Surgical Pathology: A Multicenter Blinded Randomized Noninferiority Study of 1992 Cases (Pivotal Study), Am. J. Surg. Pathol. 42 (2018) 39–52. https://doi.org/10.1097/PAS.0000000000000948.

[127] W. Mifsud, N.J. Sebire, Placental pathology in early-onset and late-onset fetal growth restriction, Fetal Diagn. Ther. 36 (2014) 117–128. https://doi.org/10.1159/000359969.

[128] S. Pathak, C.C. Lees, G. Hackett, F. Jessop, N.J. Sebire, Frequency and clinical significance of placental histological lesions in an unselected population at or near term, Virchows Arch. 459 (2011) 565–572. https://doi.org/10.1007/s00428-011-1157-z.

[129] S.M. Nguyen, G.J. Wiepz, M. Schotzko, H.A. Simmons, A. Mejia, K.D. Ludwig, A. Zhu, K. Brunner, D. Hernando, S.B. Reeder, O. Wieben, K. Johnson, D. Shah, T.G. Golos, Impact of ferumoxytol magnetic resonance imaging on the rhesus macaque maternal-fetal interface†, Biol. Reprod. 102 (2020) 434–444. https://doi.org/10.1093/biolre/ioz181.

[130] R. Chen, D.P. Seiter, L.T. Keding, J. Vazquez, K.M. Antony, H.A. Simmons, K.M. Johnson, A.K. Stanic, R.-Y. Liu, D.M. Shah, T.G. Golos, O. Wieben, Cotyledon-Specific Flow Evaluation of Rhesus Macaque Placental Injury using Ferumoxytol Dynamic Contrast Enhanced (DCE) MRI, Manuscr. Submitt. Publ. (2023).

[131] M.A. Kliewer, C.G. Bockoven, S.B. Reeder, A.R. Bagley, M.K. Fritsch, Ferumoxytol-enhanced magnetic resonance imaging with volume rendering: A new approach for the depiction of internal placental structure in vivo, Placenta 131 (2023) 104–110. https://doi.org/10.1016/j.placenta.2022.12.001.

[132] P.A. Yushkevich, J. Piven, H.C. Hazlett, R.G. Smith, S. Ho, J.C. Gee, G. Gerig, User-guided 3D active contour segmentation of anatomical structures: significantly improved efficiency and reliability, NeuroImage 31 (2006) 1116–1128. https://doi.org/10.1016/j.neuroimage.2006.01.015.

[133] C.L. Coe, G.R. Lubach, Maternal determinants of gestation length in the rhesus monkey, Trends Dev. Biol. 14 (2021) 63–72. https://doi.org/10.31300/tdb.14.2021.63-72.

[134] Ultrasound Imaging in Rhesus (Macaca mulatta) and Long-tailed (Macaca fascicularis) Macaques: Reproductive and Research Applications, in: Lab. Primate, Elsevier, 2005: pp. 317–352. https://doi.org/10.1016/b978-012080261-6/50020-9.

[135] A.E. Frias, M.C. Schabel, V.H.J. Roberts, A. Tudorica, P.L. Grigsby, K.Y. Oh, C.D. Kroenke, Using dynamic contrast-enhanced MRI to quantitatively characterize maternal vascular organization in the primate placenta, Magn. Reson. Med. 73 (2015) 1570–1578. https://doi.org/10.1002/mrm.25264.

[136] A.-P. Radan, D. Baud, G. Favre, A. Papadia, D. Surbek, M. Baumann, L. Raio, Low placental weight and altered metabolic scaling after severe acute respiratory syndrome coronavirus type 2 infection during pregnancy: a prospective multicentric study, Clin. Microbiol. Infect. 28 (2022) 718–722. https://doi.org/10.1016/j.cmi.2022.02.003.

[137] A. Jamal, S. Vosoogh, R.S. Tabatabaei, F. Salamat, Placental Size and Uterine Artery Doppler for Prediction of Adverse Pregnancy Outcomes in Women with Low Pregnancy-Associated Plasma Protein-A, Shiraz E-Med. J. 23 (2022). https://doi.org/10.5812/semj-120716.

[138] A. Eskild, E.M. Strøm-Roum, C. Haavaldsen, Does the Biological Response to Fetal Hypoxia Involve Angiogenesis, Placental Enlargement and Preeclampsia?, Paediatr. Perinat. Epidemiol. 30 (2016) 305–309. https://doi.org/10.1111/ppe.12283.

[139] S. Hietalati, D. Pham, H. Arora, M. Mochizuki, G. Santiago, J. Vaught, E.T. Lin, K.K. Mestan, M. Parast, M.B. Jacobs, Placental pathology and fetal growth outcomes in pregnancies complicated by maternal obesity, Int. J. Obes. 48 (2024) 1248–1257. https://doi.org/10.1038/s41366-024-01546-y.

[140] J. Saintonge, P. Rosso, Placental blood flow and transfer of nutrient analogs in large, average, and small guinea pig littermates, Pediatr. Res. 15 (1981) 152–156. https://doi.org/10.1203/00006450-198102000-00014.

[141] J. Kingdom, B. Huppertz, G. Seaward, P. Kaufmann, Development of the placental villous tree and its consequences for fetal growth, Eur. J. Obstet. Gynecol. Reprod. Biol. 92 (2000) 35–43. https://doi.org/10.1016/s0301-2115(00)00423-1.

[142] R.W. Redline, D.J. Roberts, M.M. Parast, L.M. Ernst, T.K. Morgan, M.F. Greene, C. Gyamfi-Bannerman, J.M. Louis, E. Maltepe, K.K. Mestan, R. Romero, J. Stone, Placental pathology is necessary to understand common pregnancy complications and achieve an improved taxonomy of obstetrical disease, Am. J. Obstet. Gynecol. 228 (2023) 187–202. https://doi.org/10.1016/j.ajog.2022.08.010.

[143] T.M. Mayhew, FIBRIN-TYPE FIBRINOID IN HUMAN PLACENTA: A STEREOLOGICAL ANALYSIS OF ITS ASSOCIATION WITH INTERVILLOUS VOLUME AND VILLOUS SURFACE AREA, Image Anal. Stereol. 20 (2011) 1. https://doi.org/10.5566/ias.v20.p1-7.

[144] M.C. Schabel, V.H.J. Roberts, J.O. Lo, S. Platt, K.A. Grant, A.E. Frias, C.D. Kroenke, Functional imaging of the nonhuman primate Placenta with endogenous blood oxygen level-dependent contrast, Magn. Reson. Med. 76 (2016) 1551–1562. https://doi.org/10.1002/mrm.26052.

[145] J.M. Miller, H.L. Brown, G.A. Kissling, H.A. Gabert, The relationship of placental grade to fetal size and growth at term, Am. J. Perinatol. 5 (1988) 19–21. https://doi.org/10.1055/s-2007-999645.

[146] K.H. Chen, L.R. Chen, Y.H. Lee, Exploring the relationship between preterm placental calcification and adverse maternal and fetal outcome, Ultrasound Obstet. Gynecol. 37 (2011) 328–334. https://doi.org/10.1002/uog.7733.

[147] A. Spinillo, S. Cesari, S. Bariselli, C. Tzialla, B. Gardella, E.M. Silini, Placental lesions associated with oligohydramnios in fetal growth restricted (FGR) pregnancies, Placenta 36 (2015) 538–544. https://doi.org/10.1016/j.placenta.2015.02.007.

[148] A. Heider, Fetal Vascular Malperfusion, Arch. Pathol. Lab. Med. 141 (2017) 1484–1489. https://doi.org/10.5858/arpa.2017-0212-RA.

[149] A. Cimic, R.N. Baergen, Meconium-Associated Umbilical Vascular Myonecrosis: Correlations with Adverse Outcome and Placental Pathology, Pediatr. Dev. Pathol. Off. J. Soc. Pediatr. Pathol. Paediatr. Pathol. Soc. 19 (2016) 315–319. https://doi.org/10.2350/15-06-1660-OA.1.

[150] J.M. Roberts, Pathophysiology of ischemic placental disease, Semin. Perinatol. 38 (2014) 139–145. https://doi.org/10.1053/j.semperi.2014.03.005.

[151] X. Tian, N.N.T. Goemaere, L. Van Der Meeren, J. Yang, J.M. Kapsenberg, L.E.E.L.O. Lashley, M. Eikmans, M.-L.P. Van Der Hoorn, Inflammatory placental lesions are specifically observed in healthy oocyte donation pregnancies with extreme fetal-maternal incompatibility, Placenta 143 (2023) 100–109. https://doi.org/10.1016/j.placenta.2023.10.005.

[152] R.W. Redline, Villitis of unknown etiology: noninfectious chronic villitis in the placenta, Hum. Pathol. 38 (2007) 1439–1446. https://doi.org/10.1016/j.humpath.2007.05.025.

[153] O.M. Faye-Petersen, D.S. Heller, V.V. Joshi, Handbook of Placental Pathology, 0 ed., CRC Press, 2005. https://doi.org/10.3109/9780203489567.

[154] M.L. Novak, T.J. Koh, Phenotypic transitions of macrophages orchestrate tissue repair, Am. J. Pathol. 183 (2013) 1352–1363. https://doi.org/10.1016/j.ajpath.2013.06.034.

[155] S. Matsumoto, E. Okamura, M. Muto, M. Ema, Similarities and differences in placental development between humans and cynomolgus monkeys, Reprod. Med. Biol. 22 (2023). https://doi.org/10.1002/rmb2.12522.

[156] S. Furukawa, Y. Kuroda, A. Sugiyama, A comparison of the histological structure of the placenta in experimental animals, J. Toxicol. Pathol. 27 (2014) 11–18. https://doi.org/10.1293/tox.2013-0060.

[157] T. Fujikura, R.C. Benson, S.G. Driscoll, The bipartite placenta and its clinical features, Am. J. Obstet. Gynecol. 107 (1970) 1013–1017. https://doi.org/10.1016/0002-9378(70)90621-6.

[158] T.K. Boyd, R.W. Redline, Chronic histiocytic intervillositis: a placental lesion associated with recurrent reproductive loss, Hum. Pathol. 31 (2000) 1389–1396.

[159] T. Raia-Barjat, M. Digonnet, A. Giraud, T. Ayash, S. Vancolen, M. Benharouga, C. Chauleur, N. Alfaidy, G. Sébire, Animal Models of Chorioamnionitis: Considerations for Translational Medicine, Biomedicines 10 (2022) 811. https://doi.org/10.3390/biomedicines10040811.

[160] H. Derricott, A.E.P. Heazell, S.L. Greenwood, R.L. Jones, A novel in vitro model of villitis of unknown etiology demonstrates altered placental hormone and cytokine profile, Am. J. Reprod. Immunol. 78 (2017) e12725. https://doi.org/10.1111/aji.12725.

[161] P.K. Lothert, B. Fedyshyn, S. Girard, R. Chakraborty, A.P. Norgan, E.A.L. Enninga, Spatial proteomics reveals phenotypic and functional differences in T cell and macrophage subsets during villitis of unknown etiology, Sci. Rep. 14 (2024) 914. https://doi.org/10.1038/s41598-024-51545-2.

[162] S.L. Deshmane, S. Kremlev, S. Amini, B.E. Sawaya, Monocyte Chemoattractant Protein-1 (MCP-1): An Overview, J. Interferon Cytokine Res. 29 (2009) 313–326. https://doi.org/10.1089/jir.2008.0027.

[163] M.W. Carr, S.J. Roth, E. Luther, S.S. Rose, T.A. Springer, Monocyte chemoattractant protein 1 acts as a T-lymphocyte chemoattractant, Proc. Natl. Acad. Sci. U. S. A. 91 (1994) 3652–3656. https://doi.org/10.1073/pnas.91.9.3652.

[164] S. Sozzani, F. Sallusto, W. Luini, D. Zhou, L. Piemonti, P. Allavena, J. Van Damme, S. Valitutti, A. Lanzavecchia, A. Mantovani, Migration of dendritic cells in response to formyl peptides, C5a, and a distinct set of chemokines, J. Immunol. Baltim. Md 1950 155 (1995) 3292–3295.

[165] P. Allavena, G. Bianchi, D. Zhou, J. van Damme, P. Jílek, S. Sozzani, A. Mantovani, Induction of natural killer cell migration by monocyte chemotactic protein-1, -2 and -3, Eur. J. Immunol. 24 (1994) 3233–3236. https://doi.org/10.1002/eji.1830241249.

[166] M.R. Koenig, J. Vazquez, F.B. Leyva Jaimes, A.M. Mitzey, A.K. Stanic, T.G. Golos, Decidual leukocytes respond to African lineage Zika virus infection with mild anti-inflammatory changes during acute infection in rhesus macaques, Front. Immunol. 15 (2024) 1363169. https://doi.org/10.3389/fimmu.2024.1363169.

[167] Z. Gu, R. Eils, M. Schlesner, Complex heatmaps reveal patterns and correlations in multidimensional genomic data, Bioinformatics 32 (2016) 2847–2849. https://doi.org/10.1093/bioinformatics/btw313.

[168] J. Vazquez, M. Chavarria, Y. Li, G.E. Lopez, A.K. Stanic, Computational flow cytometry analysis reveals a unique immune signature of the human maternal-fetal interface, Am. J. Reprod. Immunol. N. Y. N 1989 79 (2018). https://doi.org/10.1111/aji.12774.

[169] J. Vazquez, M.A. Mohamed, S. Banerjee, L.T. Keding, M.R. Koenig, F. Leyva Jaimes, R.C. Fisher, E.M. Bove, T.G. Golos, A.K. Stanic, Deciphering decidual leukocyte traffic with serial intravascular staining, Front. Immunol. 14 (2024) 1332943. https://doi.org/10.3389/fimmu.2023.1332943.

[170] T.M. Ashhurst, F. Marsh-Wakefield, G.H. Putri, A.G. Spiteri, D. Shinko, M.N. Read, A.L. Smith, N.J.C. King, Integration, exploration, and analysis of high-dimensional single-cell cytometry data using Spectre, Cytom. Part J. Int. Soc. Anal. Cytol. 101 (2022) 237–253. https://doi.org/10.1002/cyto.a.24350.

[171] A. Malhotra, B.J. Allison, M. Castillo-Melendez, G. Jenkin, G.R. Polglase, S.L. Miller, Neonatal Morbidities of Fetal Growth Restriction: Pathophysiology and Impact, Front. Endocrinol. 10 (2019) 55. https://doi.org/10.3389/fendo.2019.00055.

[172] S. Singh, D. Anshita, V. Ravichandiran, MCP-1: Function, regulation, and involvement in disease, Int. Immunopharmacol. 101 (2021) 107598. https://doi.org/10.1016/j.intimp.2021.107598.

[173] N. Omata, M. Yasutomi, A. Yamada, H. Iwasaki, M. Mayumi, Y. Ohshima, Monocyte chemoattractant protein-1 selectively inhibits the acquisition of CD40 ligand-dependent IL-12-producing capacity of monocyte-derived dendritic cells and modulates Th1 immune response, J. Immunol. Baltim. Md 1950 169 (2002) 4861–4866. https://doi.org/10.4049/jimmunol.169.9.4861.

[174] E.F. Cornish, T. McDonnell, D.J. Williams, Chronic Inflammatory Placental Disorders Associated With Recurrent Adverse Pregnancy Outcome, Front. Immunol. 13 (2022) 825075. https://doi.org/10.3389/fimmu.2022.825075.

[175] O. Dewald, P. Zymek, K. Winkelmann, A. Koerting, G. Ren, T. Abou-Khamis, L.H. Michael, B.J. Rollins, M.L. Entman, N.G. Frangogiannis, CCL2/Monocyte Chemoattractant Protein-1 Regulates Inflammatory Responses Critical to Healing Myocardial Infarcts, Circ. Res. 96 (2005) 881–889. https://doi.org/10.1161/01.RES.0000163017.13772.3a.

[176] K.H. Hong, J. Ryu, K.H. Han, Monocyte chemoattractant protein-1-induced angiogenesis is mediated by vascular endothelial growth factor-A, Blood 105 (2005) 1405–1407. https://doi.org/10.1182/blood-2004-08-3178.

[177] Q.E. Low, I.A. Drugea, L.A. Duffner, D.G. Quinn, D.N. Cook, B.J. Rollins, E.J. Kovacs, L.A. DiPietro, Wound healing in MIP-1alpha(-/-) and MCP-1(-/-) mice, Am. J. Pathol. 159 (2001) 457–463. https://doi.org/10.1016/s0002-9440(10)61717-8.

[178] J. Westman, S. Grinstein, P.E. Marques, Phagocytosis of Necrotic Debris at Sites of Injury and Inflammation, Front. Immunol. 10 (2020) 3030. https://doi.org/10.3389/fimmu.2019.03030.

[179] J.R. Thomas, P. Naidu, A. Appios, N. McGovern, The Ontogeny and Function of Placental Macrophages, Front. Immunol. 12 (2021) 771054. https://doi.org/10.3389/fimmu.2021.771054.

[180] T. Umekawa, N. Chegini, S.R. Khan, Increased expression of monocyte chemoattractant protein-1 (MCP-1) by renal epithelial cells in culture on exposure to calcium oxalate, phosphate and uric acid crystals, Nephrol. Dial. Transplant. 18 (2003) 664–669. https://doi.org/10.1093/ndt/gfg140.

[181] M.C. Wallingford, C. Benson, N.W. Chavkin, M.T. Chin, M.G. Frasch, Placental Vascular Calcification and Cardiovascular Health: It Is Time to Determine How Much of Maternal and Offspring Health Is Written in Stone, Front. Physiol. 9 (2018) 1044. https://doi.org/10.3389/fphys.2018.01044.

[182] J.S. Pober, W.C. Sessa, Inflammation and the blood microvascular system, Cold Spring Harb. Perspect. Biol. 7 (2014) a016345. https://doi.org/10.1101/cshperspect.a016345.

[183] N.R. Sibson, TNF-alpha reduces cerebral blood volume and disrupts tissue homeostasis via an endothelin- and TNFR2-dependent pathway, Brain 125 (2002) 2446–2459. https://doi.org/10.1093/brain/awf256.

[184] P. Villar-Fincheira, F. Sanhueza-Olivares, I. Norambuena-Soto, N. Cancino-Arenas, F. Hernandez-Vargas, R. Troncoso, L. Gabrielli, M. Chiong, Role of Interleukin-6 in Vascular Health and Disease, Front. Mol. Biosci. 8 (2021) 641734. https://doi.org/10.3389/fmolb.2021.641734.

[185] R. Wei, N. Lai, L. Zhao, Z. Zhang, X. Zhu, Q. Guo, C. Chu, X. Fu, X. Li, Dendritic cells in pregnancy and pregnancy-associated diseases, Biomed. Pharmacother. 133 (2021) 110921. https://doi.org/10.1016/j.biopha.2020.110921.

[186] T.L. Cranford, R.T. Enos, K.T. Velázquez, J.L. McClellan, J.M. Davis, U.P. Singh, M. Nagarkatti, P.S. Nagarkatti, C.M. Robinson, E.A. Murphy, Role of MCP-1 on inflammatory processes and metabolic dysfunction following high-fat feedings in the FVB/N strain, Int. J. Obes. 2005 40 (2016) 844–851. https://doi.org/10.1038/ijo.2015.244.

[187] R.M. Silver, Examining the link between placental pathology, growth restriction, and stillbirth, Best Pract. Res. Clin. Obstet. Gynaecol. 49 (2018) 89–102. https://doi.org/10.1016/j.bpobgyn.2018.03.004.

[188] E. Buyuk, O.A. Asemota, Z. Merhi, M.J. Charron, D.S. Berger, A. Zapantis, S.K. Jindal, Serum and follicular fluid monocyte chemotactic protein-1 levels are elevated in obese women and are associated with poorer clinical pregnancy rate after in vitro fertilization: a pilot study, Fertil. Steril. 107 (2017) 632-640.e3. https://doi.org/10.1016/j.fertnstert.2016.12.023.

[189] D.D. Briana, M. Boutsikou, S. Baka, G. Papadopoulos, D. Gourgiotis, K.P. Puchner, D. Hassiakos, A. Malamitsi-Puchner, Perinatal plasma monocyte chemotactic protein-1 concentrations in intrauterine growth restriction, Mediators Inflamm. 2007 (2007) 65032. https://doi.org/10.1155/2007/65032.

[190] L. Gu, S. Tseng, R.M. Horner, C. Tam, M. Loda, B.J. Rollins, Control of TH2 polarization by the chemokine monocyte chemoattractant protein-1, Nature 404 (2000) 407–411. https://doi.org/10.1038/35006097.

[191] L. Gu, B. Rutledge, J. Fiorillo, C. Ernst, I. Grewal, R. Flavell, R. Gladue, B. Rollins, In vivo properties of monocyte chemoattractant protein-1, J. Leukoc. Biol. 62 (1997) 577–580. https://doi.org/10.1002/jlb.62.5.577.

[192] E.A.L. Enninga, A.A. Leontovich, B. Fedyshyn, L. Wakefield, M. Gandhi, S.N. Markovic, R. Ruano, S.E. Kerr, Upregulation of HLA-Class I and II in Placentas Diagnosed with Villitis of Unknown Etiology, Reprod. Sci. Thousand Oaks Calif 27 (2020) 1129–1138. https://doi.org/10.1007/s43032-019-00101-9.

[193] G.J. Burton, Oxygen, the Janus gas; its effects on human placental development and function, J. Anat. 215 (2009) 27–35. https://doi.org/10.1111/j.1469-7580.2008.00978.x.

[194] C. Di Fabrizio, V. Giorgione, A. Khalil, C.E. Murdoch, Antioxidants in Pregnancy: Do We Really Need More Trials?, Antioxidants 11 (2022) 812. https://doi.org/10.3390/antiox11050812.

[195] G.J. Burton, E. Jauniaux, Oxidative stress, Best Pract. Res. Clin. Obstet. Gynaecol. 25 (2011) 287–299. https://doi.org/10.1016/j.bpobgyn.2010.10.016.

[196] L. Myatt, X. Cui, Oxidative stress in the placenta, Histochem. Cell Biol. 122 (2004) 369–382. https://doi.org/10.1007/s00418-004-0677-x.

[197] E. Jauniaux, J. Hempstock, N. Greenwold, G.J. Burton, Trophoblastic oxidative stress in relation to temporal and regional differences in maternal placental blood flow in normal and abnormal early pregnancies, Am. J. Pathol. 162 (2003) 115–125. https://doi.org/10.1016/S0002-9440(10)63803-5.

[198] W. Mifsud, N.J. Sebire, Placental Pathology in Early-Onset and Late-Onset Fetal Growth Restriction, Fetal Diagn. Ther. 36 (2014) 117–128. https://doi.org/10.1159/000359969.

[199] P. Cowled, R. Fitridge, Pathophysiology of Reperfustion Injury, in: Mech. Vasc. Dis. Ref. Book Vasc. Spec., University of Adelaide Press, 2011. https://www.ncbi.nlm.nih.gov/books/NBK534267/?report=classic.

[200] C.M. Scifres, D.M. Nelson, Intrauterine growth restriction, human placental development and trophoblast cell death, J. Physiol. 587 (2009) 3453–3458. https://doi.org/10.1113/jphysiol.2009.173252.

[201] M.J. Gourdin, B. Bree, M. De Kock, The impact of ischaemia–reperfusion on the blood vessel:, Eur. J. Anaesthesiol. 26 (2009) 537–547. https://doi.org/10.1097/EJA.0b013e328324b7c2.

[202] T.A. Hacker, G. Diarra, B.L. Fahl, S. Back, E. Kaufmann, W.E. Fahl, Significant reduction of ischemia-reperfusion cell death in mouse myocardial infarcts using the immediate-acting PrC-210 ROS-scavenger, Pharmacol. Res. Perspect. 7 (2019) e00500. https://doi.org/10.1002/prp2.500.

[203] D. Pereda, A. García-Alvarez, D. Sánchez-Quintana, M. Nuño, L. Fernández-Friera, R. Fernández-Jiménez, J.M. García-Ruíz, E. Sandoval, J. Aguero, M. Castellá, R.J. Hajjar, V. Fuster, B. Ibáñez, Swine Model of Chronic Postcapillary Pulmonary Hypertension with Right Ventricular Remodeling: Long-Term Characterization by Cardiac Catheterization, Magnetic Resonance, and Pathology, J Cardiovasc. Transl. Res. 7 (2014) 494–506. https://doi.org/10.1007/s12265-014-9564-6.

[204] P. Cowled, R. Fitridge, Pathophysiology of Reperfusion Injury, in: R. Fitridge, M. Thompson (Eds.), Mech. Vasc. Dis. Ref. Book Vasc. Spec., University of

Adelaide Press, Adelaide (AU), 2011. http://www.ncbi.nlm.nih.gov/books/NBK534267/ (accessed August 15, 2023).

[205] U. Borell, I. Fernstroem, AN ARTERIOGRAPHIC STUDY OF THE BLOOD FLOW THROUGH THE UTERUS AND THE PLACENTA AT MIDPREGNANCY, Acta Obstet. Gynecol. Scand. 44 (1965) 22–31. https://doi.org/10.3109/00016346509153973.

[206] C.B. Martin, H.S. McGaughey, I.H. Kaiser, M.W. Donner, E.M. Ramsey, Intermittent functioning of the uteroplacental arteries, Am. J. Obstet. Gynecol. 90 (1964) 819–823. https://doi.org/10.1016/0002-9378(64)90948-2.

[207] T.-H. Hung, G.J. Burton, Hypoxia and reoxygenation: a possible mechanism for placental oxidative stress in preeclampsia, Taiwan. J. Obstet. Gynecol. 45 (2006) 189–200. https://doi.org/10.1016/S1028-4559(09)60224-2.

[208] C.S. Rashid, A. Bansal, R.A. Simmons, Oxidative Stress, Intrauterine Growth Restriction, and Developmental Programming of Type 2 Diabetes, Physiol. Bethesda Md 33 (2018) 348–359. https://doi.org/10.1152/physiol.00023.2018.

[209] N. Aguilera, F. Salas-Pérez, M. Ortíz, D. Álvarez, B. Echiburú, M. Maliqueo, Rodent models in placental research. Implications for fetal origins of adult disease, Anim. Reprod. 19 (2022) e20210134. https://doi.org/10.1590/1984-3143-ar2021-0134.

[210] T.H. Hung, J.N. Skepper, G.J. Burton, In vitro ischemia-reperfusion injury in term human placenta as a model for oxidative stress in pathological pregnancies, Am. J. Pathol. 159 (2001) 1031–1043. https://doi.org/10.1016/S0002-9440(10)61778-6.

[211] B.C. Baker, A.E.P. Heazell, C. Sibley, R. Wright, H. Bischof, F. Beards, T. Guevara, S. Girard, R.L. Jones, Hypoxia and oxidative stress induce sterile placental inflammation in vitro, Sci. Rep. 11 (2021) 7281. https://doi.org/10.1038/s41598-021-86268-1.

[212] T.-H. Hung, J.N. Skepper, D.S. Charnock-Jones, G.J. Burton, Hypoxia-reoxygenation: a potent inducer of apoptotic changes in the human placenta and possible etiological factor in preeclampsia, Circ. Res. 90 (2002) 1274–1281. https://doi.org/10.1161/01.res.0000024411.22110.aa.

[213] S. Singh, G.C. Sensharma, P.K. Chinara, Placental changes in rat following experimental ischaemic hypoxia, Indian J. Med. Res. 77 (1983) 144–149.

[214] M. Tanaka, M. Natori, H. Ishimoto, T. Miyazaki, T. Kobayashi, S. Nozawa, Experimental growth retardation produced by transient period of uteroplacental

ischemia in pregnant Sprague-Dawley rats, Am. J. Obstet. Gynecol. 171 (1994) 1231–1234. https://doi.org/10.1016/0002-9378(94)90138-4.

[215] H. Ishimoto, M. Natori, M. Tanaka, T. Miyazaki, T. Kobayashi, Y. Yoshimura, Role of oxygen-derived free radicals in free growth retardation induced by ischemia-reperfusion in rats, Am. J. Physiol. 272 (1997) H701-705. https://doi.org/10.1152/ajpheart.1997.272.2.H701.

[216] K. Yamazaki, T. Endo, Y. Kitajima, K. Manase, K. Nagasawa, H. Honnma, T. Hayashi, R. Kudo, T. Saito, Elevation of Both Cyclooxygenase-2 and Prostaglandin E2 Receptor EP3 Expressions in Rat Placenta after Uterine Artery Ischemia–Reperfusion, Placenta 27 (2006) 395–401. https://doi.org/10.1016/j.placenta.2005.04.007.

[217] M.P. Murphy, H. Bayir, V. Belousov, C.J. Chang, K.J.A. Davies, M.J. Davies, T.P. Dick, T. Finkel, H.J. Forman, Y. Janssen-Heininger, D. Gems, V.E. Kagan, B. Kalyanaraman, N.-G. Larsson, G.L. Milne, T. Nyström, H.E. Poulsen, R. Radi, H. Van Remmen, P.T. Schumacker, P.J. Thornalley, S. Toyokuni, C.C. Winterbourn, H. Yin, B. Halliwell, Guidelines for measuring reactive oxygen species and oxidative damage in cells and in vivo, Nat. Metab. 4 (2022) 651–662. https://doi.org/10.1038/s42255-022-00591-z.

[218] C. Herce-Pagliai, S. Kotecha, D.E. Shuker, Analytical methods for 3-nitrotyrosine as a marker of exposure to reactive nitrogen species: a review, Nitric Oxide Biol. Chem. 2 (1998) 324–336. https://doi.org/10.1006/niox.1998.0192.

[219] J. Huang, J. Lauer, O. Zurkiya, Arterial thoracic outlet syndrome, Cardiovasc. Diagn. Ther. 11 (2021) 1118–1124. https://doi.org/10.21037/cdt-20-149.

[220] A. LaPelusa, H.D. Dave, Physiology, Hemostasis, in: StatPearls, StatPearls Publishing, Treasure Island (FL), 2025. http://www.ncbi.nlm.nih.gov/books/NBK545263/ (accessed July 29, 2025).

[221] N.W. Tietz, C.A. Burtis, E.R. Ashwood, eds., Tietz textbook of clinical chemistry, 2nd ed, Saunders, Philadelphia, 1994.

[222] B.E. Statland, Clinical decision levels for lab tests, 2nd ed, Medical Economics Books, Oradell, N.J, 1987.

[223] Y. Murata, Advances on the horizon, Clin. Perinatol. 9 (1982) 433–441.

[224] M.S.Y. Kwek, M. Thangaveloo, S.L.B. Hui, L.E. Madden, A.R. Phillips, D.L. Becker, Characterisation of an ischemia reperfusion model for the formation of a

stage I pressure ulcer in mouse skin, J. Tissue Viability 30 (2021) 352–362. https://doi.org/10.1016/j.jtv.2021.03.004.

[225] R.B. Killeen, S.J. Kok, D-Dimer Test, in: StatPearls, StatPearls Publishing, Treasure Island (FL), 2025. http://www.ncbi.nlm.nih.gov/books/NBK431064/ (accessed July 28, 2025).

[226] T.-H. Hung, J.N. Skepper, G.J. Burton, In Vitro Ischemia-Reperfusion Injury in Term Human Placenta as a Model for Oxidative Stress in Pathological Pregnancies, Am. J. Pathol. 159 (2001) 1031–1043. https://doi.org/10.1016/S0002-9440(10)61778-6.

[227] A. Biri, N. Bozkurt, A. Turp, M. Kavutcu, O. Himmetoglu, I. Durak, Role of oxidative stress in intrauterine growth restriction, Gynecol. Obstet. Invest. 64 (2007) 187–192. https://doi.org/10.1159/000106488.

[228] A. Karowicz-Bilińska, [Lipid peroxidation in women with gestational hypertension complicated by asymetric intrauterine growth retardation], Ginekol. Pol. 77 (2006) 435–440.

[229] J. Nowaczyk, B. Poniedziałek, P. Rzymski, D. Sikora, M. Ropacka-Lesiak, Platelets in Fetal Growth Restriction: Role of Reactive Oxygen Species, Oxygen Metabolism, and Aggregation, Cells 11 (2022) 724. https://doi.org/10.3390/cells11040724.

[230] R. Kiyokoba, T. Uchiumi, M. Yagi, T. Toshima, S. Tsukahara, Y. Fujita, K. Kato, D. Kang, Mitochondrial dysfunction-induced high hCG associated with development of fetal growth restriction and pre-eclampsia with fetal growth restriction, Sci. Rep. 12 (2022) 4056. https://doi.org/10.1038/s41598-022-07893-y.

[231] C.J. Mahoney, S. Eisele, Use of an ultrasonic blood flow monitor for determining fetal viability in the rhesus monkey (Macaca mulatta). A preliminary study, J. Med. Primatol. 5 (1976) 284–295. https://doi.org/10.1159/000459973.

[232] E.M. Ramsey, G.W. Corner, M.W. Donner, Serial and cineradioangiographic visualization of maternal circulation in the primate (hemochorial) placenta, Am. J. Obstet. Gynecol. 86 (1963) 213–225. https://doi.org/10.1016/0002-9378(63)90434-4.

[233] C. Rios-Navarro, N. Daghbouche-Rubio, J. Gavara, E. De Dios, N. Perez, J.M. Vila, F.J. Chorro, A. Ruiz-Sauri, V. Bodi, Ischemia-reperfusion injury to coronary arteries: Comprehensive microscopic study after reperfused myocardial infarction, Ann. Anat. - Anat. Anz. 238 (2021) 151785. https://doi.org/10.1016/j.aanat.2021.151785.

[234] M.M. de Jong, R. Lorusso, F. Al Awami, F. Matteuci, O. Parise, P. Lozekoot, M. Bonacchi, J.G. Maessen, D.M. Johnson, S. Gelsomino, Vascular complications following intra-aortic balloon pump implantation: an updated review, Perfusion 33 (2018) 96–104. https://doi.org/10.1177/0267659117727825.

[235] K. A Lee, Y.W. Kim, J.Y. Shim, H.S. Won, P.R. Lee, A. Kim, C.J. Kim, Distinct patterns of C4d immunoreactivity in placentas with villitis of unknown etiology, cytomegaloviral placentitis, and infarct, Placenta 34 (2013) 432–435. https://doi.org/10.1016/j.placenta.2013.02.003.

[236] K. Kumar, A.J. Fornace, S. Suman, 8-OxodG: A Potential Biomarker for Chronic Oxidative Stress Induced by High-LET Radiation, DNA 4 (2024) 221–238. https://doi.org/10.3390/dna4030015.

[237] A. Renner, M.R. Sagstetter, H. Harms, V. Lange, M.E. Götz, O. Elert, Formation of 4-hydroxy-2-nonenal protein adducts in the ischemic rat heart after transplantation, J. Heart Lung Transplant. Off. Publ. Int. Soc. Heart Transplant. 24 (2005) 730–736. https://doi.org/10.1016/j.healun.2004.02.021.

[238] S. Steven, M. Dib, S. Roohani, F. Kashani, T. Münzel, A. Daiber, Time Response of Oxidative/Nitrosative Stress and Inflammation in LPS-Induced Endotoxaemia-A Comparative Study of Mice and Rats, Int. J. Mol. Sci. 18 (2017) 2176. https://doi.org/10.3390/ijms18102176.

[239] R.L. Wilson, J.K. Schmidt, B.N. Davenport, E. Ren, L.T. Keding, S.A. Shaw, M.L. Schotzko, K.M. Antony, H.A. Simmons, T.G. Golos, H.N. Jones, Placental gene therapy in nonhuman primates: a pilot study of maternal, placental, and fetal response to non-viral, polymeric nanoparticle delivery of IGF1, Mol. Hum. Reprod. 30 (2024) gaae038. https://doi.org/10.1093/molehr/gaae038.

[240] A. Natenzon, P. McFadden, S.C. DaSilva-Arnold, S. Zamudio, N.P. Illsley, Diminished trophoblast differentiation in early onset preeclampsia, Placenta 120 (2022) 25–31. https://doi.org/10.1016/j.placenta.2022.02.004.

[241] C. Dunk, M. Kwan, A. Hazan, S. Walker, J.K. Wright, L.K. Harris, R.L. Jones, S. Keating, J.C.P. Kingdom, W. Whittle, C. Maxwell, S.J. Lye, Failure of Decidualization and Maternal Immune Tolerance Underlies Uterovascular Resistance in Intra Uterine Growth Restriction, Front. Endocrinol. 10 (2019) 160. https://doi.org/10.3389/fendo.2019.00160.